# HIGH-CONTRAST IMAGING WITH A BAND-LIMITED CORONAGRAPHIC MASK

By

JUSTIN ROBERT CREPP

A DISSERTATION PRESENTED TO THE GRADUATE SCHOOL
OF THE UNIVERSITY OF FLORIDA IN PARTIAL FULFILLMENT
OF THE REQUIREMENTS FOR THE DEGREE OF
DOCTOR OF PHILOSOPHY

UNIVERSITY OF FLORIDA

2008

For Aaron. I can't wait to meet you!

ACKNOWLEDGMENTS

I am grateful for the support and kindness of many people over the past several years who have helped me throughout graduate school and with life in general.

I thank Mom, Dad, Adam, & Kristina for your continued love and support – it has been difficult to be so far away for so long; Larry & Gay Slozat, for the great Christmas parties, your help with our first home, and, most importantly, allowing me to whisk your daughter away to Florida; Lori, Tim, & Jaxon, for giving me a place to sleep before and after observing runs; Brian Sands, for the late-night physics conversations, get-rich-quick schemes, and teaching me the art of your great patience (of which I am still learning); Andrew Vanden Heuvel, for your contagious enthusiasm, being my partner in crime our first two years in Florida, and conquering Rome with me in a single day; Matthew Turk, for sharing with me your mad-scientist-like computer skills, dining with Judy and I at IP and Herwig's before becoming a vegetarian, and giving me a place to stay during post-doc interviews; Anthony, Craig, Curtis, Dave, Ji, Jorge, Mark, and PC, for keeping me involved in athletics – because of you, my sanity is, I think, still intact; Knicole and Paola for keeping me company in the office while working into the wee hours of the morning; Dimitri for your famous "Late Night Cookie Time" and trivia; Sun Mi, for your karaoke skills, love of Indian food, and multiple birthday parties (per year); Leah, for giving me a lift to and from the Gainesville airport at a moment's notice; Kelly Bradley, for hiring me at the Athletic Tutoring Center; Charlotte Dare, for hiring me as the billiards leisure course instructor; Pam Fitzgerald, for keeping me involved in public outreach with the local grade schools; Steamers, for serving such delectable dishes, and, to a lesser extent, the Krishna folks.

I thank Darren Williams, my undergraduate advisor, Blair Tuttle, and the other professors at Penn State Behrend for preparing me for graduate school and showing me the importance of balance in life; Jian Ge, my graduate thesis advisor, for setting a good example of work-ethic, improving my proposal writing skills, paying my fees every

semester, and supporting the many high-contrast imaging projects; Marc Kuchner, for inventing the band-limited mask and being my external mentor; Eugene Serabyn, for giving us access to the relay optics and serving as PI for observations at Palomar; Joe Carson, for taking care of the politics to install a coronagraphic mask in PHARO; Kent Wallace, Rick Burruss, and Jeff Hickey for your help on the mountain at Palomar – we will get flex-cam working someday, I promise; Bo and Xiaoke, for your help in the lab; Suvrath, for your leadership, knowledge of the literature, and our frequent pizza runs to Cloudcroft; Ji Wang, aka "King Lucky", for reconstructing wavefronts, calculating Strehl ratios, and your optimism towards our projects; Julian, for bringing your consistency to the radial velocity team and reminding me when the space shuttle would next be launched; Scott and PC for the many fun observing runs and stimulating scientific and nonscientific conversations; Audrey Simmons, for playing chess, basketball, piano, cards, frisbee, pool, and backgammon with the ET observers to help pass the time at Sloan; all members of the ET radial velocity team for your hard work; Jeff Julian, for letting me borrow your tools; and Margaret, for conversations in a different bandpass.

Thanks also go to my PhD thesis committee, Jian Ge, Steve Eikenberry, Eric Ford, Katia Matcheva, and Charlie Telesco, which is comprised of world-class instrument builders and experts in planetary science.

I acknowledge support from the Sigma Xi for two grants in aid of research, the SPIE for a scholarship, and the Advanced Research Projects Agency for a grant to work on technologies associated with the Terrestrial Planet Finder (TPF) mission.

Finally, this work would not have been possible without the support of my beautiful and loving wife Amy. You have sacrificed so much to be with me in Florida. Thank you for your encouragement and patience, for accommodating my awkward work schedule, and for entertaining me with stories from Westwood Middle School. I love you.

TABLE OF CONTENTS

LIST OF TABLES

LIST OF FIGURES

## LIST OF SYMBOLS AND ABBREVIATIONS

| | |
|---|---|
| BLM | band-limited mask |
| DH | dark hole |
| DM | deformable mirror |
| FOV | field of view |
| GPI | Gemini Planet Imager |
| IWA | inner-working-angle |
| JPL | Jet Propulsion Laboratory |
| PALAO | PALomar Adaptive Optics system |
| PHARO | Palomar High Angular Resolution Observer |
| PSF | point-spread function |
| RV | radial velocity |
| SETI | Search for ExtraTerrestrial Intelligence |
| SIM | Space Interferometry Mission |
| SPHERE | Spectro-Polarimetric High-contrast Exoplanet REsearch instrument |
| TPF-C | The Terrestrial Planet Finder – Coronagraph |
| TPF-I | The Terrestrial Planet Finder – Interferometer |
| WFE | wavefront error |

Abstract of Dissertation Presented to the Graduate School
of the University of Florida in Partial Fulfillment of the
Requirements for the Degree of Doctor of Philosophy

HIGH-CONTRAST IMAGING WITH A BAND-LIMITED CORONAGRAPHIC MASK

By

Justin Robert Crepp

August 2008

Chair: Jian Ge
Major: Astronomy

We present a comprehensive study of the band-limited coronagraphic mask. Emphasis is placed on its ability to detect faint substellar companions when operating in concert with a high-actuator-density deformable mirror. Both space and ground-based applications are considered.

It is shown that a new kind of band-limited mask, the "eighth-order" mask, can remove diffracted starlight while providing more resistance to tip/tilt errors and low-order aberrations as compared to other designs. This feature also naturally translates to an improved resistance to the finite size of stars. Our numerical simulations indicate that a TPF-C-like instrument equipped with an eighth-order mask can, in addition to achieving its baseline goal of characterizing "Earth-like" planets orbiting main-sequence stars, also address fundamental questions regarding planet formation and evolution by targeting nearby evolved stars. We show that such observations can probe the exoplanet population near the high-mass-end of the spectral-sequence and also possibly constrain the timescale for the development of life.

We next make a comparative study of the performance of various coronagraphic masks when in the presence of atmospheric turbulence. It is shown that there are several guidelines for deciding the design of a ground-based image-plane occulter: (i) to justify the use of a band-limited mask, the on-sky Strehl ratio delivered by the adaptive optics system must exceed $\approx 0.88\ S_{qs}$, where $S_{qs}$ is the intrinsic (quasi-static) Strehl ratio provided by

the instrument; (ii) one should never build a Gaussian coronagraphic mask; and (iii) the use of higher-order band-limited masks, such as the eighth-order mask, is relegated to situations where quasi-static residual starlight cannot be sufficiently removed from the search area with speckle-nulling hardware. These results are independent of the telescope entrance aperture geometry.

We then built the first series of eighth-order band-limited masks using electron-beam lithography and test their performance in the lab. Our experiments show that eighth-order masks follow the theoretical predictions for resistance to tip/tilt and focus alignment errors and can generate contrast levels of $2 \times 10^{-6}$ at $3\ \lambda/D$ in a system with $\approx 1$ nm of rms wavefront error over the surface of critical optics.

This work culminates with the design and fabrication of the first band-limited mask for on-sky observations – a demonstration that also constitutes the first tests of a leading TPF-C design candidate using "extreme" AO. Contrast levels sufficient to detect brown dwarfs over a wide range of ages are generated at projected separations $\gtrsim 100$ AU for the stars: HIP 72567, HIP 83389, and HD 102195, a.k.a. ET-1. The sensitivity is limited by non-common-path errors and AO lag-time for the fainter targets.

Taking advantage of the mask's linear geometry, we also conducted the first high-contrast imaging observations of visual binary stars by suppressing both sources simultaneously to search for faint tertiary companions.

# CHAPTER 1
# INTRODUCTION TO HIGH-CONTRAST IMAGING

## 1.1 Background Information

High-contrast imaging is a technique whereby astronomers attempt to detect and characterize faint objects that are located in the immediate vicinity of a bright source. Applications include searching for debris disks, brown dwarf companions, and planets orbiting nearby stars. Extragalactic studies, such as observations close to the nucleus of an active galaxy, are also possible.

The first demonstration of high-contrast imaging technology took place in the late 1930s when Bernard Lyot built an instrument to block light from the disk of the Sun in order to study its peripheries. He was particularly interested in the solar corona and planned to conduct extensive observations whenever desired, instead of waiting for the infrequent occurrence of an eclipse. His invention, which now bares the name: the Lyot *corona*graph (§1.3), has become an indispensable tool in the field. It can be found at most ground-based observatories. Moreover, the Hubble Space Telescope (HST) has a coronagraphic operating mode (Krist 2007), the James Webb Space Telescope (JWST) will be equipped with coronagraphic starlight suppression hardware (Clampin 2007), and one of the Terrestrial Planet Finder (TPF) missions (§3) will likely utilize some variation of Lyot's original concept to generate unprecedented sensitivity (Shaklan & Levine 2007).

Modern high-contrast imaging is motivated primarily by extrasolar planet research. To date, nearly 300 planets have been detected orbiting other stars (http://exoplanet.eu/; http://exoplanets.org/); however, the vast majority were discovered using *indirect* techniques. Radial velocity (RV) (Marcy & Butler 2000), transit photometry (Charbonneau et al. 2000), gravitational microlensing (Gaudi et al. 2008), astrometry (Benedict et al. 2006), and pulsar timing (Wolszczan & Frail 1992) each rely upon measurements of the star but not the planet itself. The evidence is often a periodic signal superposed onto the star's signature (e.g., its relative position in the sky, brightness, location of spectral

lines) and is compelling enough to infer the existence of a companion.[1] Such observations, however, often leave important physical characteristics, such as mass, radius, effective temperature, and chemical composition poorly constrained (Table 1-1). Direct imaging is an intuitive alternative that yields explicit photometric and spectroscopic information. In this regard, it represents the future of exoplanetary science.

Table 1-1. Comparison chart of planet detection techniques – February 2008

| | RV | Transits | Astrometry | Lensing | Pulsar Timing | Imaging |
|---|---|---|---|---|---|---|
| Mass | $\sim$ | ✓ | $\sim$ | ✓ | $\sim$ | ✓ |
| Radius | x | ✓ | x | x | x | ✓ |
| $T_{eff}$ | x | $\sim$ | x | x | x | ✓ |
| Composition | x | $\sim$ | x | x | x | ✓ |
| Orbit[a] | proj. | ✓ | proj. | proj. | proj. | proj. |
| Obser. Bias[b] | age, $P$ | $P$ | $P$ | $P$ | neutron stars | $P$ |
| Efficiency | $\geq 1P$ | $\geq 2P$ | $\geq 1P$ | hours | $\geq 1P$ | hours[c] |
| Detections | 221 | 36[d] | 1[e] | 6 | 5 | 1 |

x = no information; $\sim$ = weak constraint; ✓ = strong constraint

[a]Most techniques provide information only on the projected orbit (proj.). The inclination of a transiting planet is approximately $90^0$.

[b]All approaches, including pulsar timing, have an intrinsic observational bias to the orbital period, $P$. The bias is most severe with transit photometry.

[c]The members of entire planetary systems can, in principle, be detected and characterized simultaneously via direct imaging.

[d]More than one-third were originally detected with RV and later found to eclipse the star.

[e]*HST* astrometric measurements have confirmed the RV planet $\epsilon$ Eridani b (Benedict et al. 2006), and shown another candidate, HD 33636 b, to be a low-mass star (Bean et al. 2007).

All such techniques are naturally most sensitive to companions with substantive mass. For instance, Jupiter ($M_{Jup} \sim 332 M_{Earth}$) serves as a convenient fiducial for the bulk of discoveries listed above. There is even a class of short-period planets known as "hot-Jupiters" whose existence has revealed that planets can migrate during the latter stages of formation (Lin et al. 1996). However, to address other questions regarding the origin and structure of planetary systems, it is necessary to detect lower-mass bodies, of

[1] A planet orbiting a white dwarf has even been discovered using stellar oscillation (pulsation) timing (Mullally et al. 2008).

order Neptune and smaller, by refining these methods and building instruments for space. Current data (Fig. 1 − 1) and the leading formation theory of "core-accretion" (Pollack et al. 1996) suggest that low-mass planets may indeed be common (Ida & Lin 2004).

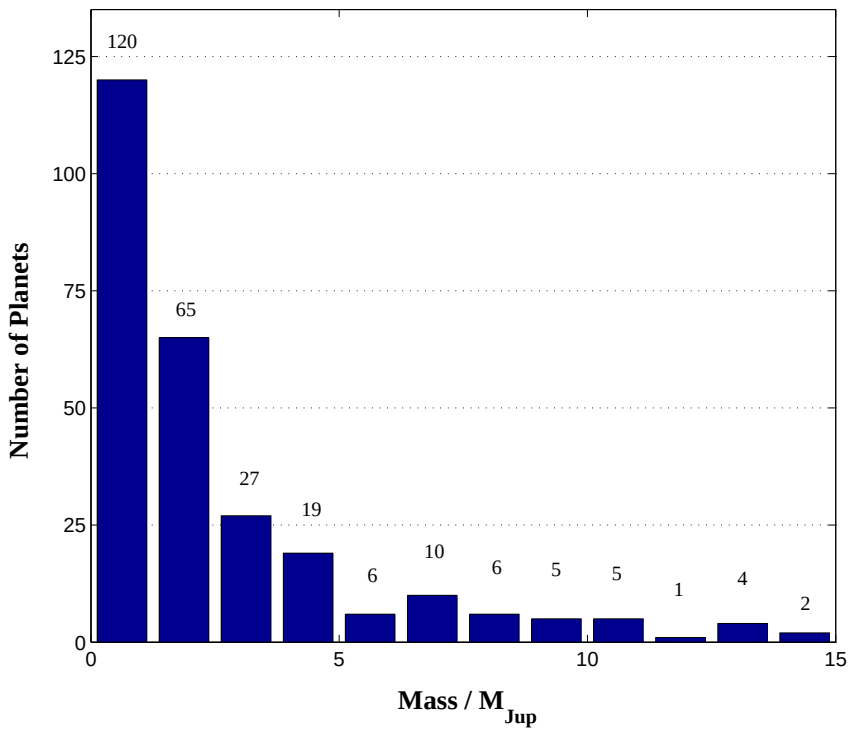


Figure 1-1. Number of planets detected orbiting other stars as a function of mass (data from the Exoplanet Encyclopedia, Schneider, J. – March 7, 2008). Evidence for a paucity of brown-dwarfs is clear, given the current sensitivity, $\sim 1$ m/s, of RV instruments (Marcy & Butler 2000). The prospects for an abundance of low-mass planets are promising.

One of astronomy's principle goals in the next century is to detect a terrestrial planet orbiting in the habitable zone (Kasting et al. 1993) of a nearby star. The space missions COROT (transit photometry – launched December 2006), Kepler (transit photometry – scheduled launch 2009), and SIM (astrometry – launch date uncertain) will each be sensitive to rocky worlds located at orbital distances where water can persist in the liquid phase. Their observations will place the first constraints on the population statistics of planets with potentially hospitable environments. However, only a direct imaging

instrument will be able to unambiguously detect atmospheric biomarkers, such as $H_2O$, $CO_2$, $O_2$, $O_3$, $CH_4$, and $N_2O$, which are indicative of life (Kaltenegger et al. 2007).

NASA has therefore proposed two additional missions, a series of Terrestrial Planet Finders, that will obtain spectra of "Earth-like" exoplanets (should they exist). The first instrument, TPF–C, will utilize a coronagraph and single-dish telescope operating at visible wavelengths to collect reflected light (§3), while the second, TPF–I, will complement these observations at mid-IR wavelengths, with a long-baseline interferometer. The TPF–C will be launched before TPF–I, even though the difference in brightness between a star and planet is more favorable in the infrared (§1.2.1). This decision is based on the fact that coronagraphic technologies, such as those described in this thesis, are maturing rapidly (see also http://www.lyot2007.org/), while interferometric-nulling technologies (Wallace et al. 2000), such as precision formation flying[2] – which is required to achieve the necessary spatial resolution – are more risky and difficult to demonstrate pre-launch. (Nevertheless, ESA has elected to move straight to the interferometric approach with the Darwin mission (Fridlund 2004).)

There are several prospective designs for the TPF–C. One of the most promising candidates utilizes a *band-limited mask*: an occulter that resides in the focal plane of the Lyot coronagraph and controls diffraction by manipulating the amplitude of starlight. The band-limited mask provides numerous benefits for high-contrast imaging, such as deep suppression of starlight over a broad bandpass, high off-axis transmission, close inner-working-angle, resistance to low-order aberrations, resistance to finite stellar size, and flexibility in design and manufacturing. It also requires a minimal number of optics

[2] SIM will have a 9m baseline and employ rigid-body beam-combination. The TPF–I calls for multiple baselines exceeding 100m. The positioning of optics, for both missions, must be controlled to a level of order the coherence length of light, $\lambda^2/\Delta\lambda$.

to implement, which limits the number of scattering surfaces and allows for a compact instrument. These advantages also translate to ground-based observations.

The following work describes the band-limited mask (§2) and its performance in numerical simulations (with respect to both space (§3) and ground-based (§4) observations) and lab experiments (§5), as well as on-sky tests using an "extreme" adaptive optics system (§6) and coronagraphic observations of visual binary stars (§7). The remainder of this chapter outlines the various goals and challenges of high-contrast imaging in general and introduces the Lyot coronagraph. The discussion assumes single main-sequence stars as the astrophysical targets of interest, unless otherwise stated.

## 1.2 Essential Concepts

Contrast, $C$, is defined as the relative brightness between a companion and its host,

$$C = \int_{\lambda_{min}}^{\lambda_{max}} B_{companion}(\lambda)\, d\lambda \;/ \int_{\lambda_{min}}^{\lambda_{max}} B_{star}(\lambda)\, d\lambda \;\; \ll 1, \tag{1–1}$$

where $\lambda_{min}$ and $\lambda_{max}$ indicate the bandpass. Its value depends strongly on the mass ratio and system age, and can change by several orders of magnitude when observations are conducted in visible versus mid-infrared wavelengths. Direct detection requires that instruments generate sensitivities comparable to $C$ at a given angular separation, otherwise companions will remain hidden beneath stellar residuals.

"High"-contrast imaging, as is often written in the literature (even though Equ. 1–1 is the conventional definition), is difficult because optical phenomena that are commonplace and unavoidable, such as diffraction or reflection from a mirror, scatter a large amount of starlight into the search area. Moreover, the pattern, or frequency spectrum, of noise is structured such that contamination increases for regions closer to the star, making detection a considerable challenge. The degree of difficulty depends on the type of companion since the formation mechanisms, which govern the mass and characteristic orbital separation, of terrestrial planets, giant planets, and brown dwarfs, fundamentally differ.

### 1.2.1 Faint Companions

#### 1.2.1.1 Visible wavelengths

In reflected light, the relative brightness can be calculated from the system geometry. Consider a companion with radius $R_p$ placed at a distance $d_p$ from its star. The approximate monochromatic contrast is given by the fraction of starlight intercepted by the companion's surface,

$$C \approx \epsilon \frac{\pi R_p^2}{4\pi d_p^2 \,/\, 2}, \tag{1–2}$$

where $\epsilon$ is an order unity factor that takes into account reflection efficiency effects, such as albedo and orbital phase.

The canonical example is that of an Earth-like planet, $R_p = 6400$ km, located in the habitable zone, $d_p = 1$ AU. Using $\epsilon = 0.4$, Equ. 1–2 yields $C \approx 4 \times 10^{-10}$. More careful calculations, that include spectral features and a reasonable bandpass, find $C \approx 2 \times 10^{-10}$ (Des Marais et al. 2002), as is nominally quoted.

Measurement of any quantity to an accuracy of 1 part in $10^{10}$ requires compensation for a variety of subtle effects. A comparison to experimental results for the values of fundamental physical constants places the number into context: the mass of the electron, Boltzmann's constant, Newton's gravitational constant, Planck's constant, and the elementary charge have relative uncertainties of $4.9 \times 10^{-8}$, $1.7 \times 10^{-6}$, $1.0 \times 10^{-4}$, $5.0 \times 10^{-8}$, $2.5 \times 10^{-8}$ respectively (National Institute of Standards – http://www.nist.gov/). One of the most important and reliably measured quantities, the fine structure constant, $\alpha$, has a relative uncertainty of $6.8 \times 10^{-10}$. Its value was most recently determined by comparing the results from a one-electron quantum cyclotron to a QED calculation involving 891 eighth-order Feynman diagrams (Gabrielse et al. 2006). The analogy is not without flaw, but rightfully conveys the message that imaging an Earth-like exoplanet is non-trivial. Jupiter would be the easiest planet to detect if the solar system were targeted by a distant observer, but it is still a factor of $10^9$ times fainter than the Sun in the visible (Fig. 1-2).

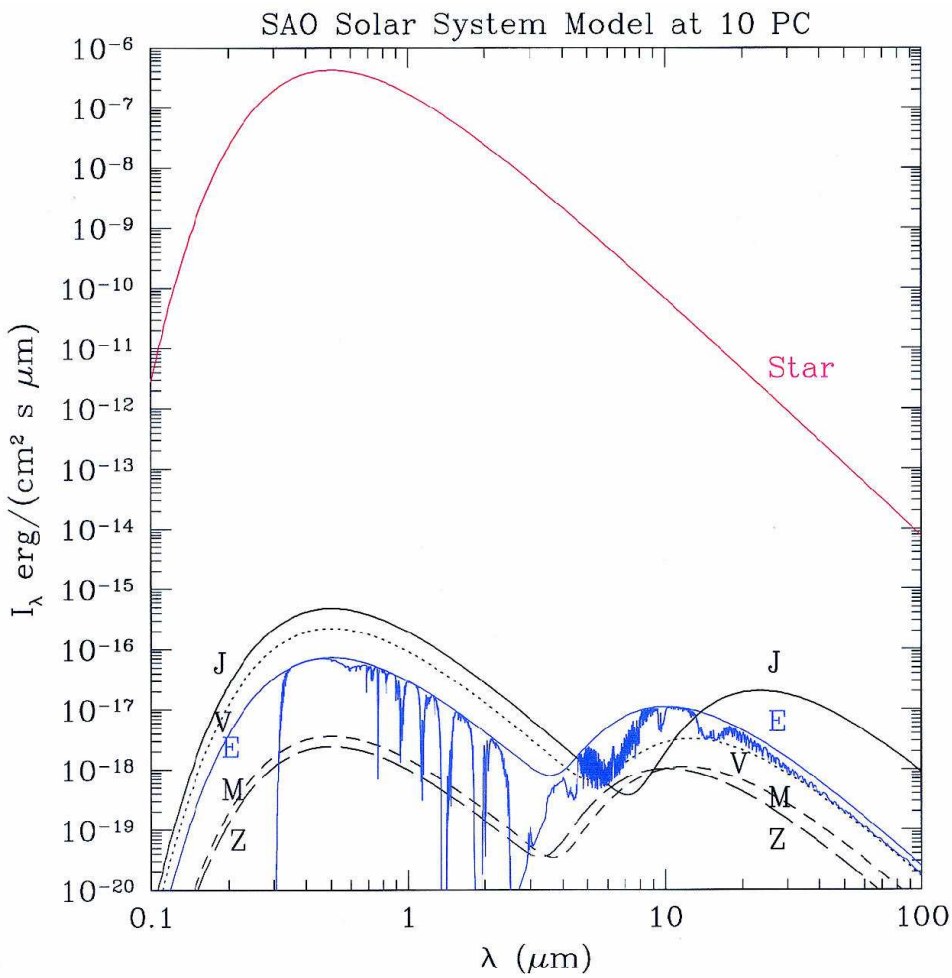


Figure 1-2. Smithsonian Astrophysical Observatory code model of the solar system as seen from 10 pcs (from Des Marais et al. (2002)). Contrast is found by comparing the stellar flux to planet flux in a particular wavelength range, where 'J' is Jupiter, 'V' is Venus, 'E' is Earth, 'M' is Mars, and 'Z' is the zodiacal dust cloud. Important trade-offs exist between required sensitivity, spatial resolution, atmospheric correction, and background noise when considering the bandpass of observations.

Instruments must generate these contrast levels at angular separations smaller than 1" (4.8 microradians) since the closest stars are several parsecs away. These considerations essentially preclude ground-based imaging detections of planets at short wavelengths due to the blurring effects of the atmosphere (see §4), even in the foreseeable future. Only the TPF-C (§3) or similar space-mission can begin to access this observational parameter space.

#### 1.2.1.2 Mid-infrared wavelengths

The sensitivities required in the mid-IR are more reasonable, since the blackbody radiation of a cool companion, $T_{eff} \lesssim 800$ K, peaks where the Rayleigh-Jeans tail of the (presumably much hotter) star declines. For instance, the contrast of the Earth-Sun system at $\lambda = 10\ \mu$m is "only" $10^{-6}$ (Fig. 1-2). Recent lab demonstrations have achieved comparable sensitivities, $C = 6 \times 10^{-5}$, at close separations using a TPF-I candidate design (Labadie et al. 2007).

A number of ground-based instruments operate in this spectral range. They are diffraction limited and some are even equipped with a coronagraph (Telesco et al. 1998; Telesco 2007; Kasper et al. 2007). Nevertheless, exoplanets have yet to be discovered in the mid-IR because bright thermal emission from the sky can only be subtracted out to one part in $\approx 10^5$ at the photon noise limit, e.g., when short exposures are taken in an attempt to "freeze" the thermal pattern before substantial fluctuations occur. The sky is roughly as bright as a 6th magnitude star in the L-band (Phillips et al. 1999) and brighter in M and N.

Companions such as 2MASS1207, GQ Lupi, and AB Pic, whose near-IR images are shown in the next section, may be just bright enough to outshine this sea of thermal noise (Telesco et al. 2008, in prep.). M and N-band photometry can place tight constraints on their effective temperature and mass. However, only the youngest and most massive Jovian planets with large orbital separations will satisfy the detection criterion to circumvent these fundamental limitations. Ground-based imaging at infrared wavelengths longwards of $\lambda \approx 5\ \mu$m can thus play only a minor role in extrasolar planet direct imaging detection in the near-term. The study of brown dwarfs, however, is not preclusive.

Current space missions, such as Spitzer (Fazio et al. 2004), do not have the requisite spatial resolution, which is an issue even for 8-10m telescopes. Instead, TPF-I and Darwin will exploit the advantages of the mid-IR using interferometry. As with SIM and TPF-C, their funds are limited and schedules currently uncertain.

For information regarding mid-IR circumstellar debris disk imaging, which has important implications for planet formation, see the PhD thesis of Margaret Moerchen 2008.

#### 1.2.1.3 Near-infrared wavelengths

Most ground-based efforts have focused on near-IR observations. There are two particularly compelling reasons: (i) the J, H, & K bands, corresponding to $\lambda_{central} \approx 1.25$, 1.65, 2.20 $\mu$m respectively, offer a practical compromise between the competing effects of star-to-planet brightness, spatial resolution, atmospheric correction, and sky background noise; and (ii) atmospheric models predict that young, massive exoplanets, which have a high internal luminosity, preferentially release energy in these bands (Fig. 1-3).

Contrast levels of order $10^{-8}$ are required to detect 100 Myr old Jovian planets (Burrows et al. 2004; Marley et al. 2007), but many stellar clusters, associations, and moving groups are younger and host brighter, more easily detectable companions (see López-Santiago et al. (2006) for an excellent reference). For instance, the expected J-band contrast of a $1M_{Jup}$ planet orbiting a K0V star at 5 Myrs and 50 Myrs is about $1.2 \times 10^{-5}$ and $3.3 \times 10^{-7}$ respectively (Baraffe et al. 2003; Girardi et al. 2002). The only remaining complication is that young stars tend to be relatively distant, and large aperture telescopes cannot achieve the necessary atmospheric correction (§1.2.3) without "extreme" adaptive optics (AO) systems (§4), which do not yet exist.

The next generation of high-contrast instruments, namely GPI (Macintosh et al. 2006a) and SPHERE (Dohlen et al. 2006), which will begin operations within the next three-four years, will feature high-actuator-density deformable mirrors (§3, §4) and coronagraphs coupled to integral field units (McElwain et al. 2007). Near-IR sensitivities of $\sim 10^{-7}$ at $\sim$0.2" are anticipated. This is sufficient to directly detect self-luminous Jovian planets.

Current AO-coronagraph instruments have generated contrast levels of order $10^{-4}$ at 0.5" - 1.0" separations, with final effective sensitivities of $\approx 10^{-5}$ following post-processing

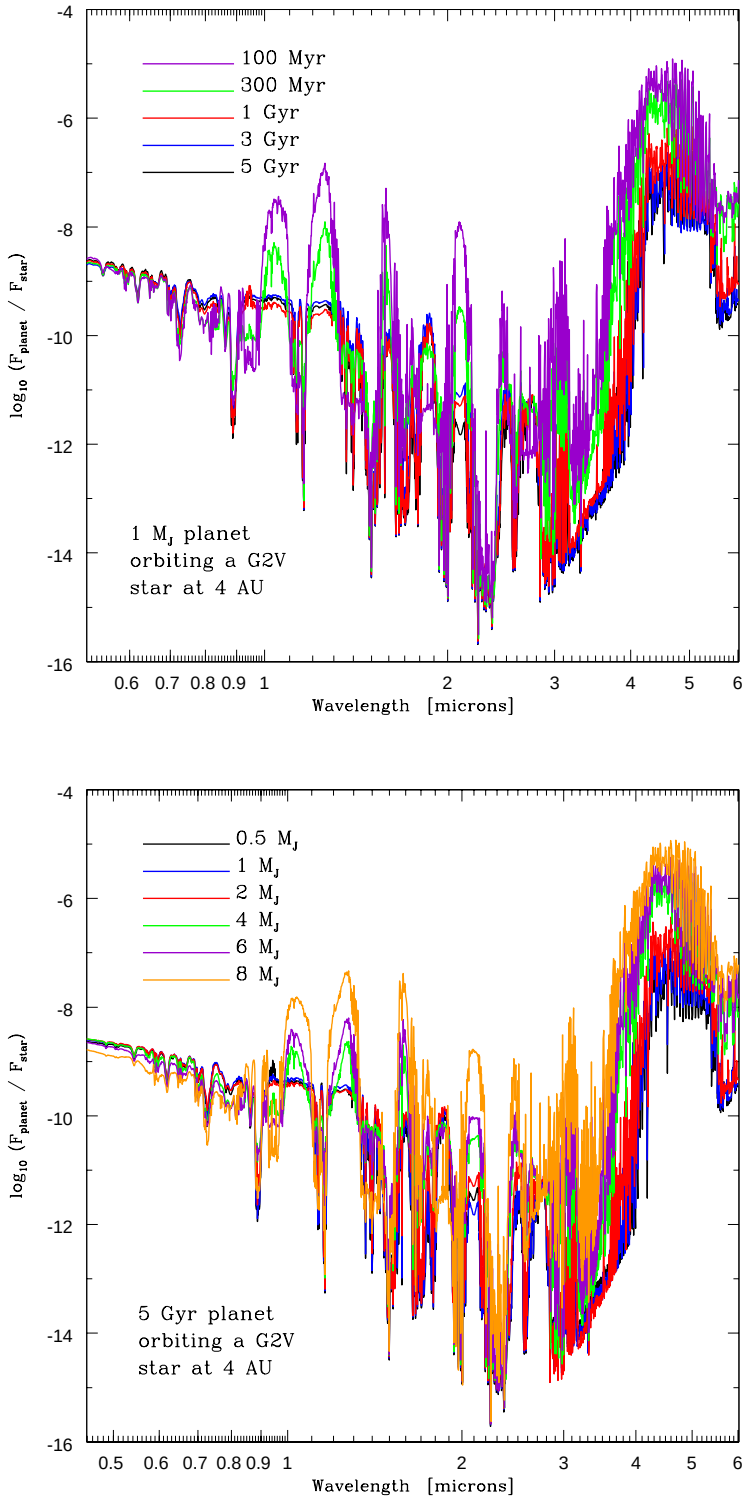


Figure 1-3. Atmospheric model predictions of contrast vs. wavelength for various ages (top) and masses (bottom) of Jovian exoplanets (from Burrows et al. (2004)).

(Lafrenière et al. (2007); Nielsen et al. (2008)). They have placed tight constraints on the population statistics of brown dwarfs ($13M_{Jup} \leq M \leq 80M_{Jup}$) orbiting single stars at intermediate to large ($\gtrsim$ 10 AU) separations (Carson et al. 2006; Metchev & Hillenbrand 2004) and have produced the first images of candidate planetary mass companions.

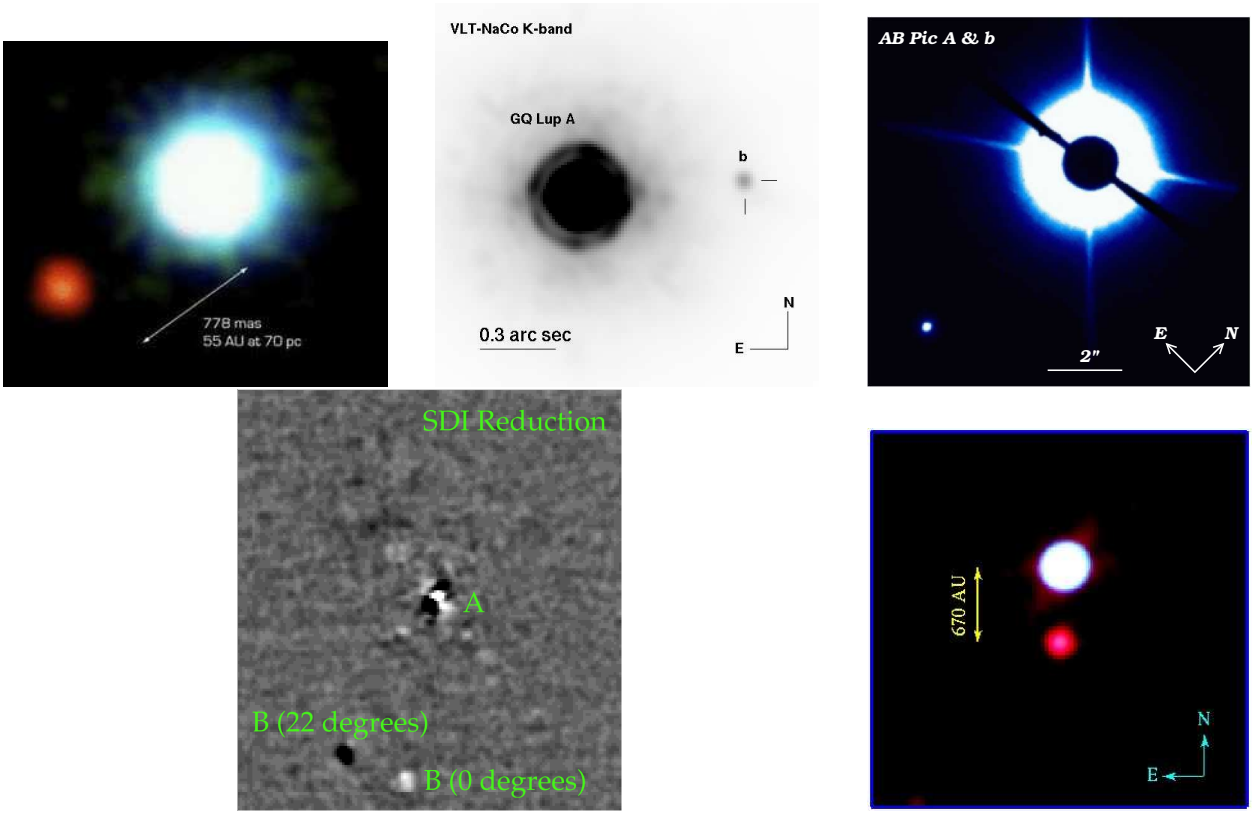


Figure 1-4. The first images of candidate extrasolar planets: (upper-left) 2MASS1207 from Chauvin et al. (2005a), (upper-middle) GQ Lupi from Neuhäuser et al. (2005), (upper-right) AB Pic from Chauvin et al. (2005b), (lower-left) SCR 1845 from Biller et al. (2006), and (lower-right) UScoCTIO from Béjar et al. (2008).

### 1.2.2 Diffraction Management

Diffraction sets the angular scale for which high-contrast imaging instruments can operate. The inner-working-angle (hereafter, IWA) is the closest distance that reasonable sensitivities can be generated. Coronagraphs can typically access regions several $\lambda/D$ away from the star. At smaller scales, the light from low-order diffraction and phase aberration modes (see §1.2.3) is too intense and cannot be properly managed without simultaneously attenuating the companion.

Table 1-2. Direct imaging tradeoffs with bandpass

| | Visible | Near-IR | Mid-IR |
|---|---|---|---|
| bandpass ($\mu$m) | $0.5 - 0.8$ | $1.0 - 2.5$ | $5 - 20$ |
| IWA[a] (mas) | 62 | 193 | 387, 773, 1547 |
| contrast needed | $< 10^{-9}$ | $< 10^{-7}$ | $< 10^{-5}$ |
| AO correction | not feasible | "extreme" AO | low-order AO |
| active optics[b] | precision $< 1$ Å | precision $< 1$ nm | low-order correction |
| sky background | negligible | manageable | limiting |
| (exo)zodiacal light | faint | moderate | bright |
| terrestrial | space | space | space |
| Jovian | space | ground / space | space[c] |

[a]Inner-working-angle (IWA) is defined here as $3\,\lambda_{max}/D$, where $D = 8$ m. The mid-IR IWA's are for $\lambda_{max} = 5$, 10, and 20 $\mu$m respectively.
[b]Correction of quasi-static wavefront errors (§3). Values are quoted for space applications.
[c]Ground-based imaging in the mid-IR can potentially access the youngest and most massive exoplanets that have large ($\gtrsim$ 15 AU) orbital separations.

A slice of the Airy pattern is shown in Fig. 1-5. It is clearly not an optimal direct imaging point-spread function (hereafter, PSF): the contrast at 3 $\lambda/D$ is $1.4 \times 10^{-3}$. A coronagraph can suppress the Airy pattern while efficiently passing off-axis light. Entrance apertures with central obstructions and support structures complicate the issue by requiring more restrictive stops to block diffraction, resulting in throughput losses. For this reason, the baseline design for TPF-C incorporates an off-axis primary mirror (Ford et al. 2006). Chapter 6 describes a ground-based approach involving a clear aperture.

Interferometers can create a PSF consisting of very deep nulls by changing the phase of light in one or more arms. This circumvents the problem of building occulting spots that have a physical size of several diffraction widths[3] and results in an improved IWA ($\approx 0.5\,\lambda/d$, where $d$ is the baseline). However, the total search area decreases as a result of alternating bright and dark fringes (planets can only be found in the dark ones), requiring instrument rotations and hence losses in duty-cycle efficiency. This fundamental

[3] Another option is to change the shape of the entrance aperture. The "shaped-pupil" coronagraph (Kasdin et al. 2003) is a former TPF-C design candidate – at least in this author's opinion. It requires that too much throughput be sacrificed to be viable.

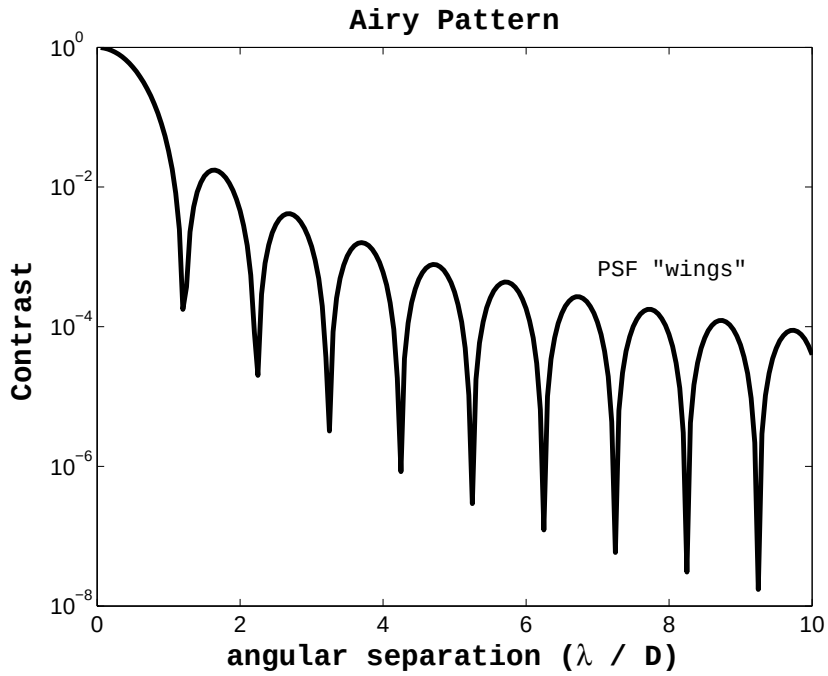


Figure 1-5. Diffraction-limited point-spread-function from an unobstructed circular aperture. The contrast is insufficient to detect extrasolar planets.

tradeoff is a result of interference, which forms the basis for diffraction. The mathematics for understanding coronagraphy (§1.3) are similar to high-contrast interferometry; in coronagraphy, however, the multiple (virtual) dishes can overlap.

### 1.2.3 Speckle Formation

Wavefront errors transfer energy from the PSF-core to a halo of 'speckles' surrounding the source. They arise from non-uniformities in the optical path length (phase errors) and transmission (amplitude errors). Active optics, such as deformable mirrors or light modulators, can be used to compensate for these effects over low spatial frequencies that are commensurate with the search area.

Phase errors result from temperature fluctuations in the atmosphere (which lead to changes in the index of refraction) and the surface roughness of optical components. Atmospheric phase errors change on a millisecond timescale and have a larger amplitude than the systematics produced by telescope and instrument optics. Left uncorrected, both sources can limit sensitivities at the $10^{-3}$ level.

Amplitude errors result from deviations in the throughput of parcels of air and reflectivity of optics. They are, however, much less problematic than phase errors and can be categorized as a $\lesssim 10^{-7}$ effect, provided the system is free of large dust particles. For example, the baseline GPI strategy is to correct for phase errors only (Bruce Macintosh, private communication), in order to maximize search area (see §3).

Wavefront errors manifest as speckles in the image plane. One can gain an intuition for their formation from the following example. Consider a complex field passing through a one-dimensional telescope entrance aperture given by $A(u)$ where $u$ is the physical coordinate and has units of $D/\lambda$. Assume that the phase aberration, $\phi(u)$, consists of a single sine-wave ripple of frequency $f$ cycles per aperture and amplitude $a$ in radians. The electric field in the pupil plane is:

$$E(u) = A(u)\, e^{i\phi(u)} \tag{1–3}$$

where $A(u)$ is a top-hat function,

$$A(u) = \begin{cases} 1 & \text{where } |u| < 1/2 \\ 0 & \text{elsewhere.} \end{cases} \tag{1–4}$$

For small aberrations ($a << 1$) we can expand the exponential and keep the first term, $e^{i\phi(u)} \approx 1 + i\, a\, sin(2\pi f u)$. In the Fraunhofer or far-field diffraction regime (Hecht & Zajac 1974), the electric field in the image plane is found by taking a Fourier transform, FT{...}:

$$\begin{aligned} \hat{E}(x) &= \mathrm{FT}\{E(u)\} \\ &= \mathrm{FT}\{A(u)\} * (\delta(x) - a/2\,[\delta(x+f) - \delta(x-f)]) \end{aligned} \tag{1–5}$$

where the hat, $\hat{-}$, denotes an image plane quantity, $*$ is the convolution operator, and $x$ corresponds to an angle with units $\lambda/D$.

We now let $\mathrm{FT}\{A(u)\} = \hat{A}(x)$, which is simply the diffraction-limited PSF, and recognize that it is copied at the location of the three delta functions, $x = 0$, $x = -f$, and

$x = +f$, but with a different weighting,

$$\hat{E}(x) = \hat{A}(x) - a/2\ \hat{A}(x+f) + a/2\ \hat{A}(x-f). \tag{1–6}$$

An ideal coronagraph will remove the zero-frequency component, $\hat{A}(x)$, but cannot eliminate the other two terms, otherwise the companion would be attenuated. Thus, a sine-wave phase ripple creates two peaks of light, or speckles, at locations in the image plane that correspond to the spatial frequency $f$. This forms the basis for understanding high-contrast imaging wavefront aberration theory, since any general wavefront shape can be constructed from of a series of sines and cosines. A deformable mirror (DM) can suppress speckles by reshaping the phase of starlight (Fig. 1-6).

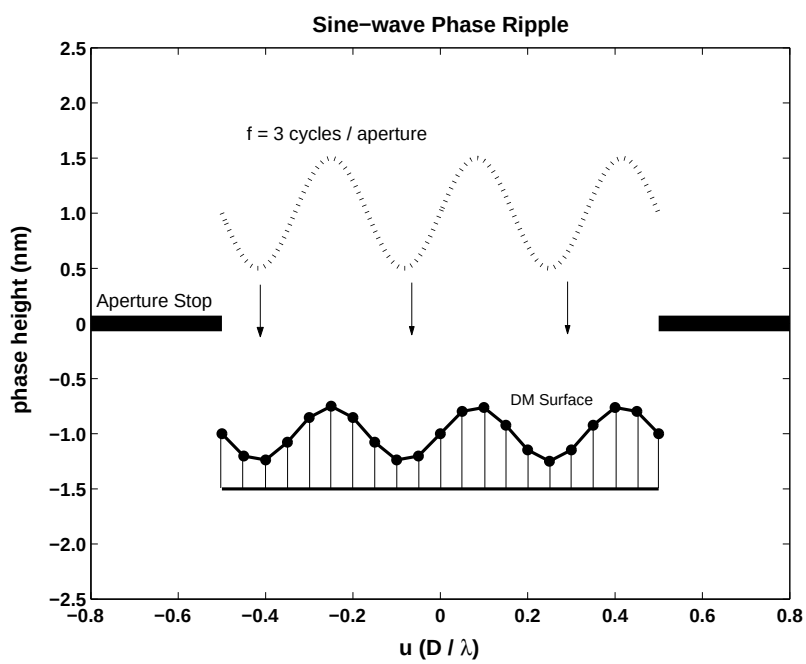


Figure 1-6. Cartoon of a single frequency 1 nm peak-to-trough phase error across the telescope entrance aperture and a 19 actuator DM for conjugation. The $f = 3$ sine-wave aberration would normally create 2 speckles at $\pm 3\ \lambda/D$ in the image plane. Instead, the phase errors are suppressed to a level given by how well the DM can match the in-coming wavefront shape (fitting-errors). The DM surface need only be half the wavefront phase height due to the reflection. The light is then sent to the coronagraph.

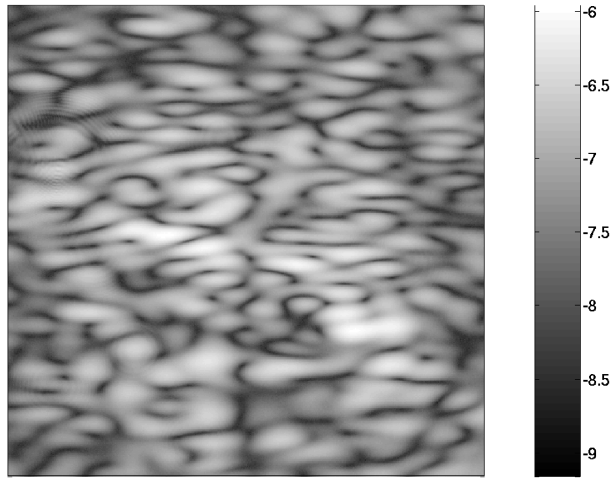


Figure 1-7. Monochromatic speckles at the detector of a lab experiment using a Lyot coronagraph. The contrast is of order $10^{-6}$ (§5) as is indicated by the intensity gray-scale shown to the right.

Notice also that the speckle intensity, $|\hat{E}|^2$ (§1–6), scales as $a^2$. This relation has been verified with numerical simulations in §3. Phase errors of order 1 nm limit contrast at the $\approx 10^{-7}$ level at the coronagraph IWA in the visible. Therefore, to detect an Earth-like planet, the phase of light must be controlled to better than $\approx 1/\sqrt{10^3}$ nm, or $\approx 0.6$ Bohr radii, over the spatial frequencies of interest.

The phase amplitudes, $a(f)$, form a frequency spectrum (§3) that dictates the spatial distribution of power or energy in the image. The power-spectra of atmospheric aberrations differ from that of lenses and mirrors, but both can be reasonably well-modeled with a monotonically decreasing power-law or broken power-law in $f$. In other words, more stellar residuals are located close to the optical axis than further away.

Figure 1-7 shows quasi-static speckles from a lab experiment using a coronagraph (Crepp et al. 2006). The contrast is limited at the $10^{-6}$ level at the IWA, implying that wavefront phase errors are several nanometers in size. This was verified explicitly with profilometer measurements of the surface of the most critical optic.

Image quality is often characterized by the Strehl ratio, $S$, which is defined as,

$$S = \frac{\text{measured peak intensity of source}}{\text{theoretical max peak intensity of source}} < 1. \tag{1–7}$$

A Strehl of 0.6 indicates that the atmosphere or instrument optics have scattered $\sim 40\%$ of the PSF core energy. Much of that light lands in the search area.

The Strehl ratio can be related to the rms wavefront error by the Marichal formula,

$$S \approx e^{-\sigma_{rms}^2} \tag{1–8}$$

where $\sigma_{rms}$ is the root-mean-square wavefront error in radians. If we substitute for $\sigma_{rms}$ the previous result that the wavefront must be controlled to better than $1/\sqrt{10^3}$ nm at $\lambda = 650$ nm in order to generate $10^{-10}$ contrast, we find that $S = 0.99999990656$. Hence, ground-based imaging of terrestrial planets at visible wavelengths is impractical (see also Guyon (2005) for other reasons).

At near-IR wavelengths, the Strehl ratio of 8-10m telescopes is often less than 10% without wavefront correction. With current adaptive optics (AO) technology, Strehl ratios of $\approx 40\%$ are possible. This value is still insufficient and serves as the motivation for the development of "extreme" AO and the work done in Chapter 6.

## 1.3 The Lyot Coronagraph

There are many kinds of coronagraphs. They can be roughly categorized into two groups: 'interferometric' coronagraphs and modifications of the Lyot coronagraph. Most designs fall into the latter category, although there still exists an impressively large diversity amongst individual approaches. Guyon et al. (2006) have compiled a list of coronagraphic concepts that can, in principle, achieve $10^{-10}$ contrast at 5 $\lambda/D$ – the so-called "Coronagraph Tree of Life". Their abbreviated names are: the AIC, CPAIC, VNC, PSC, CPA, PPA, PIAAC, PIZZA, APLC, APLCN, BLM4, BLM8, PM, 4QPM, APKC, OVC$m$, AGPMC, and ODC.

Guyon et al. (2006) have also compared their performance on an equal footing using a 'useful throughput' metric. In the ideal case, the OVC – Optical Vortex (Mawet et al. 2007), PIAAC – Phase Induced Amplitude Apodization (Guyon 2003), BLM4 – 4th-order Band-limited Mask (Kuchner & Traub 2002), and BLM8 – 8th-order Band-limited Mask

(Kuchner, Crepp, & Ge 2005) coronagraphs yield the best results. The differences between their individual benefits are: the OVC and PIAAC have sharper PSF's, better IWA's, and higher throughput than the BLM4 and BLM8, and can therefore detect more targets per time, but are *significantly* more susceptible to low-order optical aberrations (§2,§4, §5) and finite stellar size (§3). These practical tradeoffs (which are studied in this work), along with chromaticity considerations, will determine the design of the TPF-C (see also Cash (2006) and §3). The BLM4 and BLM8 are unique amongst this elite list in that they are also useful from the ground (§4, §6, §7). They, along with the optical vortex (phase) mask, are located in the image plane of the Lyot coronagraph, which is described below. The BLM4 and BLM8 are described in detail in §2.

The Lyot coronagraph (Lyot 1939) controls diffraction with a combination of an image mask and aperture stop. The mask and stop work together to suppress light from a source that is aligned to the optical axis. Light emanating from an off-axis source, such as a debris disk or substellar companion, enters the coronagraph at a small angle and suffers minimal attenuation. The result is a gain in the *relative* number of photons received from faint objects located in close angular proximity to the star. A well-calibrated coronagraph operates like a high-pass filter and can improve sensitivities by many orders of magnitude. Figure 1-8 depicts a transmissive design without wavefront control.

The first-order diffraction theory for light propagation through the Lyot coronagraph is as follows: The electric-field at the entrance aperture is given by,

$$E(u, v) = E_0(u, v)A(u, v), \tag{1–9}$$

where $E_0$ is the complex field and $u$, $v$ are pupil plane quantities. For simplicity, we assume here that no aberrations are present and set $E_0 = 1$. We also neglect telescope obstructions so that $A(u, v)$ is just a circle or two-dimensional top-hat function.

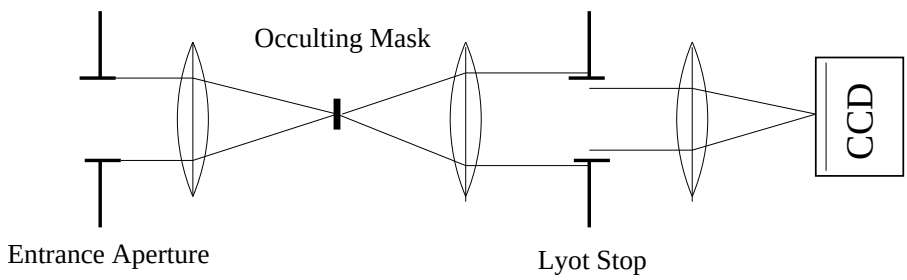


Figure 1-8. Optical layout of a transmissive Lyot coronagraph. The design is similar to a spectrograph, except there is a mask and stop instead of a slit and grating.

Light entering the coronagraph is focused onto an occulting mask in the first image plane. The electric-field is then,

$$\hat{E}(x,y) = \hat{A}(x,y)\hat{M}(x,y), \tag{1–10}$$

where $M(x,y)$ is the mask amplitude transmission profile. The mask intensity transmission is $|\hat{M}(x,y)|^2$ and, typically, $M(x=0,y=0)=0$.

The electric field at the subsequent pupil plane is found by taking another Fourier transform,

$$E_{Lyot}(u,v) = A(u,v) * M(u,v). \tag{1–11}$$

This equation is the key to understanding Lyot coronagraphy. The field at the Lyot stop is the convolution of the entrance aperture with the mask spatial frequency function. In order to generate dynamic range, the light pattern must be faint near the center of the pupil and bright near the edges. This way the Lyot stop can effectively remove starlight while allowing most of the off-axis light to reach the detector.

The field at the detector is,

$$\hat{E}_{final} = \hat{L}(x,y) * \hat{A}(x,y)\,\hat{M}(x,y), \tag{1–12}$$

where $L(u,v) \rightleftharpoons \hat{L}(x,y)$ is the Lyot stop. The intensity is $|\hat{E}_{final}|^2$. Images of the field at various locations along the path are shown in §4.

# CHAPTER 2
# THE BAND-LIMITED MASK

## 2.1 Basic Principle

The band-limited mask is an occulter located in the image plane of the Lyot coronagraph (Kuchner & Traub 2002). It diffracts starlight into spatially succinct regions that follow the contour of the telescope entrance aperture. The combination of a band-limited mask and appropriately shaped Lyot stop can *completely* remove the on-axis light from an optical system when it is free of aberrations.

Equation 1–11 provides the basis for understanding its operation. Consider a one-dimensional coronagraph with monochromatic light as in §1.2.3. We again model the telescope entrance aperture as a top-hat in the pupil. The question is: "What function, or set of functions, when convolved with the telescope entrance aperture, create an ideal diffraction pattern at the Lyot pupil?" (Fig. 2-1).

An example of an ideal mask function is one that places all of the starlight exterior to a certain region or distance from the optical axis. A simple stop, one that is opaque on the outside and transparent in the center, can then block it all while still passing light from the companion. Such a function would satisfy the following criterion,

$$\int_{\epsilon/2}^{\epsilon/2} M(u)du = 0, \tag{2–1}$$

and

$$M(u) = 0, \text{ for } |u| > \epsilon \,/\, 2 \tag{2–2}$$

where $M(u)$ is the image mask spatial frequency function and $0 \leq \epsilon \leq 1$ is a dimensionless parameter that controls the bandwidth. The function is said to be *band-limited* because only a range of low spatial-frequencies are present. Equ. 2–1 ensures that no starlight "leaks" through the coronagraph when the $A(u)$ and $M(u)$ functions overlap during convolution, while Equ. 2–2 ensures the same when the functions do not overlap.

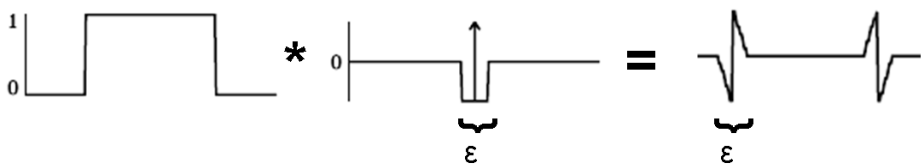


Figure 2-1. Convolving $A(u)$ with a band-limited mask function $M(u)$ produces an optimal diffraction pattern at the Lyot pupil plane (Kuchner & Traub 2002). The resultant electric field is multiplied by another top-hat, the Lyot stop (not shown), in order to remove all on-axis starlight.

The mask function shown in Fig. 2-1 is

$$M(u) = N\left[\delta(u) - \frac{1}{\epsilon}\,\Pi\left(\frac{u}{\epsilon}\right)\right] \tag{2–3}$$

where $N$ is a normalization constant. The Fourier transform of Equ. 2–3 gives the amplitude transmission,

$$\hat{M}(x) = N[1 - \mathrm{sinc}(\pi\epsilon x)]. \tag{2–4}$$

Band-limited masks are graded masks. Their intensity transmission, $0 \leq |\hat{M}(x)|^2 \leq 1$ (i.e. the part we actually build), varies smoothly in opacity. In broadband light, we design the mask to operate at $\lambda_{max}$, since shorter wavelengths are diffracted *outside* the Lyot stop.

Examples of other band-limited functions are: $\hat{M}(x) = \sin^2(\pi\epsilon x/2)$, $1 - \mathrm{sinc}^n(\pi\epsilon x/n)$, where $n$ is an integer, and $1 - J_0(\pi\epsilon x)$. They generally trade IWA with off-axis attenuation. In other words, masks with intrinsically close IWA's, such as the $\sin^2(..)$ design, have more 'ringing' (opaque regions) in the search area. If $\epsilon$ is increased to improve the IWA, then the Lyot stop throughput decreases.

For instance, consider the linear $1 - \mathrm{sinc}^2(\pi\epsilon x/2)$ mask. A two-dimensional coronagraph with an IWA of $4\lambda/D$, where IWA is taken as the location where the intensity transmission reaches 0.5, would have a Lyot stop throughput of 64%. Other band-limited masks, such as the radial design, $\hat{M} \rightarrow \hat{M}(r)$, and separable design, $\hat{M} \rightarrow \hat{M}(x)\,\hat{M}(y)$, are also available. They likewise trade search space for throughput.

## 2.2 Eighth-Order Masks

A linear combination of band-limited functions creates another band-limited function. The masks described in §2 are "fourth-order" masks: their intensity transmission near the optical axis increases as the fourth-power with distance. It is possible to generate higher-order mask functions, such as an eighth-order (Kuchner, Crepp, & Ge 2005) or twelfth-order mask, by combining fourth-order mask functions .

The motivation for this concept is that intrinsically wider masks help filter low-order aberration content. They are also more robust to pointing errors and the finite size of stars. For example, an eighth-order mask would allow the TPF-C to operate with a pointing accuracy no better than that of the Hubble Space Telescope, $\sim 3$ mas, whereas a fourth-order mask would require $\sim 0.7$ mas. The price for relaxing such tolerances is a modest cost in off-axis throughput.

To construct an eighth-order mask, we need the amplitude transmission term responsible for quadratic leakage to equal zero,

$$\frac{d^2}{dx^2}\,\hat{M}(x)\bigg|_{x=0} = 0. \tag{2–5}$$

This can be accomplished by adding an appropriately weighted $C\sin^2(k_1x) \approx (C/2)(k_1x)^2$ function to any $1 - \mathrm{sinc}^n(k_2x/n) \approx (k_2x)^2/(6n)$ function. Notice that the individual terms also automatically satisfy Equ. 2–1 and 2–2. Setting $k_1 = k_2$ we find $C = -1/(3n)$. To ensure $\hat{M}(x) \leq 1$, we renormalize the mask by multiplying $\hat{M}(x)$ by a constant, $N$.

Putting everything together and using physical units yields a series of eighth-order band-limited masks,

$$\hat{M}_{BL}(x) = N\left[\frac{3n-1}{3n} - \mathrm{sinc}^n\frac{\pi x\epsilon}{n\lambda_{max}f} + \left(\frac{1}{3n}\right)\cos\frac{\pi x\epsilon}{\lambda_{max}f}\right], \tag{2–6}$$

where $f$ is the focal ratio at the mask and $\lambda_{max}$ is the longest wavelength at which the mask is to operate. Figure 2-2 shows $\hat{M}(x)$ for the first few linear masks in the series.

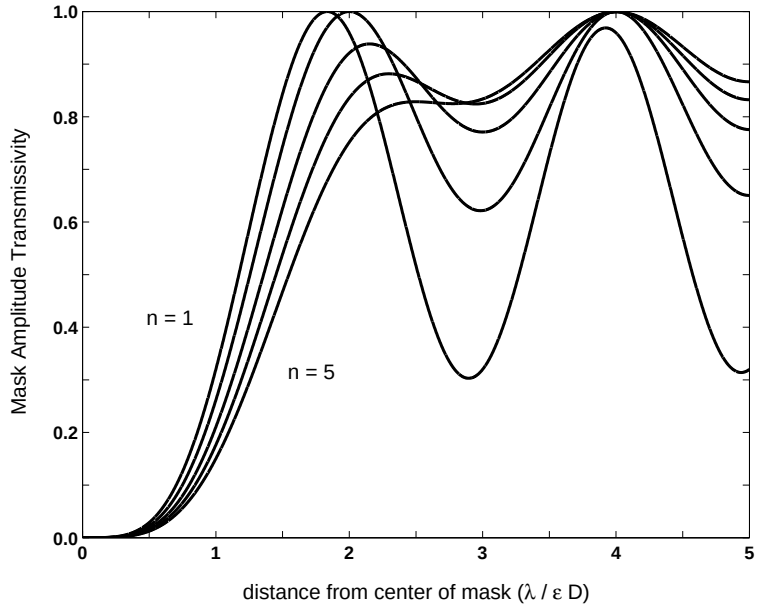


Figure 2-2. Eighth-order band-limited mask functions described by Equation 2–6 for $n = 1 - 5$.

We can create another series of eighth-order masks with less off-axis attenuation by combining two $1 - \mathrm{sinc}^n$ masks using the same procedure:

$$\hat{M}_{BL}(x) = N\left[\frac{l-m}{l} - \mathrm{sinc}^l \frac{\pi x \epsilon}{l \lambda_{max} f} + \frac{m}{l}\,\mathrm{sinc}^m \frac{\pi x \epsilon}{m \lambda_{max} f}\right]. \tag{2–7}$$

This series is parameterized by two integer exponents, $l$ and $m$; we assume $l > m$. Figure 2-3 shows $\hat{M}(x)$ for $m = 1$ and $l$ =2–5. The $m = 1$ and $l$ =2–3 masks have throughput similar to the $n = 3$ $\sin^2$ mask from above. Using large values of $m$ and $l$ reduces the 'ringing' further, but also decreases the Lyot stop throughput.

Figure 2-4 compares the intensity transmission, $|\hat{M}(x)|^2$, for the $1 - \mathrm{sinc}^2$ fourth-order mask and the $m = 1$, $l = 3$ eighth-order mask. While the $1 - \mathrm{sinc}^2$ mask has an IWA of $(1.448/\epsilon)(\lambda/D)$, the $m = 1$, $l = 3$ eighth-order mask has an IWA of $(1.788/\epsilon)(\lambda/D)$. The $m = 1$, $l = 3$ mask offers a good compromise between ringing and throughput, and also reaches 100% transmission at its first maximum, a critical region for planet searching. This mask design is recommended for the TPF-C.

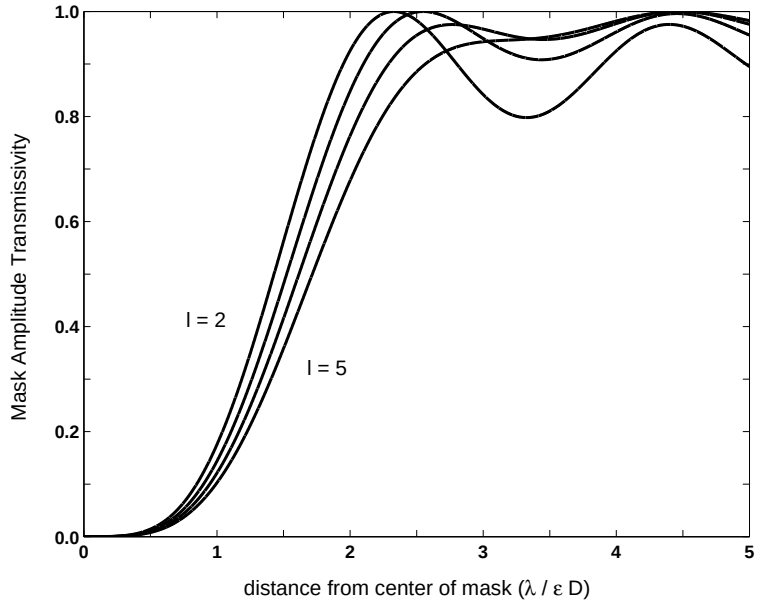


Figure 2-3. Eighth-order band-limited mask functions described by Equation 2–7 for $m = 1$, $l = 2 - 5$.

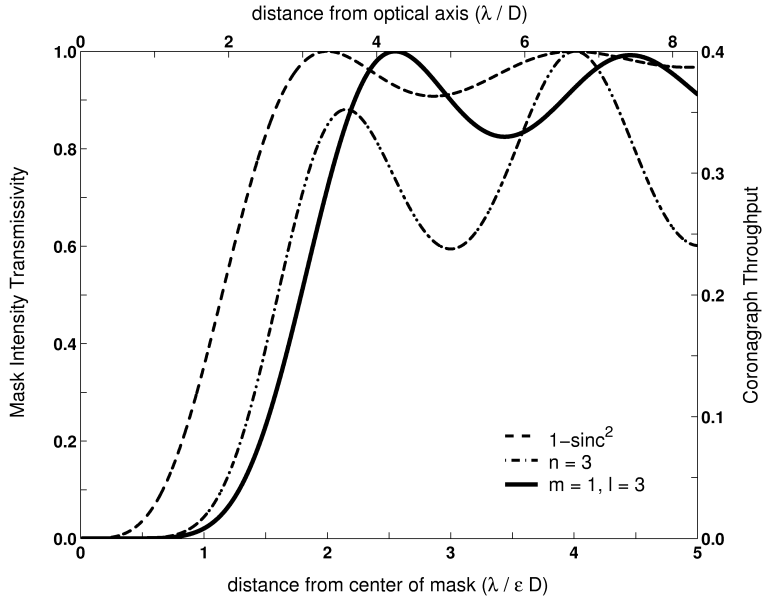


Figure 2-4. Intensity transmission for the $1 - \mathrm{sinc}^2$ fourth-order mask, the $n = 3$ eighth-order mask, and the $m = 1$, $l = 3$ eighth-order mask. Coronagraph throughput and distance from optical axis were calculated with $\epsilon = 0.6$. The $m = 1$, $l = 3$ eighth-order mask, recommended for TPF-C, has 100% transmission at its first maximum.

Masks of higher-order can also be derived. They suppress low spatial-frequency aberrations even further, but have significantly less Lyot stop throughput. The twelfth-order mask is a viable tool when the IWA is large – for example if one wanted to search the extended habitable zone of a giant star (§3).

### 2.3 Higher Spatial-Frequencies

There is an additional degree of freedom that we can exploit to construct band-limited masks that are potentially easier to fabricate. Close inspection of Fig. 2-1 and Equ. 2–2 reveals that power at mask spatial frequencies $|u| > 1 - \epsilon/2$ results in starlight being diffracted well outside the Lyot stop opening. Masks that utilize this design freedom are called notch-filter masks (Kuchner & Spergel 2003). They need not have smooth intensity transmission profiles. Instead, notch filter masks can be sampled or binary, or both. In the following, we use a technique similar to the one employed in §2.2 to find eighth-order notch filter masks (Kuchner, Crepp, & Ge 2005). To be consistent with §2.2, we refer to the various designs by the exponents of their constituent functions ($n$, $l$, $m$).

We start with a linear combination of fourth-order notch filter masks,

$$\hat{M}_{notch_8}(x) = N\left[\hat{M}_{notch_{4A}}(x) + C\hat{M}_{notch_{4B}}(x)\right], \tag{2–8}$$

where $N$ ensures that $\hat{M}_{notch_8}(x) \leq 1$. The constant $C$ is found by substituting Equ. 2–8 into Equ. 2–5, where

$$\frac{d^2}{dx^2}\,\hat{M}(x)\bigg|_{x=0} = \int_{-\epsilon/2}^{\epsilon/2}(-2\pi i u)^2 M(u)du = 0, \tag{2–9}$$

and the derivatives are taken only over the low spatial frequencies (see Kuchner, Crepp, & Ge 2005 for details). The answer is:

$$C = -\frac{\int_{-\epsilon/2}^{\epsilon/2} u^2 M_{notch_{4A}}(u)\,du}{\int_{-\epsilon/2}^{\epsilon/2} u^2 M_{notch_{4B}}(u)\,du}, \tag{2–10}$$

where $-1 \leq C \leq 0$.

To finish the derivation, we need to calculate $M_{notch_4}(u) \rightleftharpoons \hat{M}_{notch_4}(x)$. Fourth-order sampled masks are defined by the following prescription (Kuchner & Spergel 2003):

$$\hat{M}_{notch_4}(x) = \hat{M}_{samp_4}(x) - \hat{M}_0, \tag{2–11}$$

where

$$\hat{M}_{samp_4}(x) = \hat{P}(x) * \left( \hat{M}_{BL_4}(x)\, \Delta x \sum_k \delta(x - (k+\zeta)\Delta x) \right), \tag{2–12}$$

$$M_{samp_4}(u) = P(u) \left( M_{BL_4}(u) * \sum_k \delta(u - k/\Delta x) e^{-2\pi i u \zeta \Delta x} \right), \tag{2–13}$$

and

$$\hat{M}_0 = \int_{-\epsilon D/(2\lambda)}^{\epsilon D/(2\lambda)} M_{samp_4}(u)\, du = \int_{-\infty}^{\infty} M_{BL_4}(u) P(u)\, du = \hat{M}_{BL_4}(x) * \hat{P}(x) \Big|_{x=0}. \tag{2–14}$$

Here, $M_{BL_4}$ represents any fourth-order band-limited mask function and $k$ ranges over all integers. The sampling points are offset from the mask center by a fraction $\zeta$ of $\Delta x$. The kernel, $\hat{P}(x)$, can represent the "beam" of a nanofabrication tool. It should be normalized so that $\int_{-\infty}^{\infty} \hat{P}(x)\, dx = 1$, and $\hat{P}(x)$ must be everywhere $\leq 1/(\Delta x)$, so $\hat{M}_{samp_4}(x)$ remains $\leq 1$. The constant $\hat{M}_0$ ensures that the mask satisfies Equation 2–1. Though the sampled mask is derived from $\hat{M}_{BL_4}(x)$, the function being sampled is $\hat{M}_{BL_4}(x) - \hat{M}_0$.

Substituting Equ. 2–11 into Equation 2–8 we have

$$\hat{M}_{notch_8}(x) = N \left[ (\hat{M}_{samp_{4A}}(x) - \hat{M}_{0_A}) + C(\hat{M}_{samp_{4B}}(x) - \hat{M}_{0_B}) \right], \tag{2–15}$$

and using Equ. 2–13 and 2–14 the constant $C$ becomes

$$C = -\frac{\int_{-\epsilon/2}^{\epsilon/2} u^2 P(u) M_{BL_{4A}}(u)\, du}{\int_{-\epsilon/2}^{\epsilon/2} u^2 P(u) M_{BL_{4B}}(u)\, du}. \tag{2–16}$$

We can now construct a variety of eighth-order notch filter masks analogous to the variety of eighth-order band-limited masks.

In the following, we provide example calculations for making sampled binary and sampled graded eighth-order notch filter masks using the $m = 1$, $l = 3$ design. We assume a linear mask geometry and consider broadband light.

### 2.3.1 Binary Masks

Binary masks are everywhere either completely opaque or completely transparent. To build one that satisfies the various diffraction criterion we assemble a collection of identical parallel stripes, where a notch filter mask function provides the width of each stripe,

$$\hat{M}_{stripe}(x, y) = \begin{cases} 1 & \text{where } y < \hat{M}_{notch}(x)\, \lambda_{min} f \\ 0 & \text{elsewhere.} \end{cases} \tag{2–17}$$

The mask function is

$$\hat{M}_{binary}(x, y) = \sum_{j=-\infty}^{\infty} \hat{M}_{stripe}(x,\ y - j\lambda_{min} f), \tag{2–18}$$

where $\lambda_{min}$ is the shortest wavelength in the band of interest. Band-limited masks leak light at wavelengths longer than $\lambda_{max}$, whereas notch filter masks can also leak light at wavelengths shorter than $\lambda_{min}$. In other words, the notch filter mask operates like a band-limited mask so long as the optical system does not resolve its intricate features.

If we like, we can use the band-limited mask functions described by Equations 2–6 or 2–7 in place of $\hat{M}_{notch}(x)$, resulting in a mask formed of continuous curves. However, sampled binary masks may prove to be easier to manufacture since their features are not as small near the optical axis. The binary mask shown in Fig. 2-6 is sampled. It can be made entirely from rectangles of opaque material using $e$-beam lithography (§5).

The function we actually sample is $N[(\hat{M}_{BL_{4A}}(x) - \hat{M}_{0_A}) + C(\hat{M}_{BL_{4B}}(x) - \hat{M}_{0_B})]$. Figure 2-5 shows a plot of this function to illustrate how $\zeta$ may be chosen. To guarantee that $\hat{M}_{notch}(x) \geq 0$, the parameter $\zeta$ must be in the range $|\zeta| \leq \zeta_0$, where $\zeta_0$ is defined by the condition $\hat{M}_{BL_{4A}}(\zeta_0 \lambda_{min} f) + C\hat{M}_{BL_{4B}}(\zeta_0 \lambda_{min} f) = \hat{M}_{0_A} + C\hat{M}_{0_B}$. For our binary mask, we choose $\zeta = \zeta_0$, to make the central rectangles contiguous.

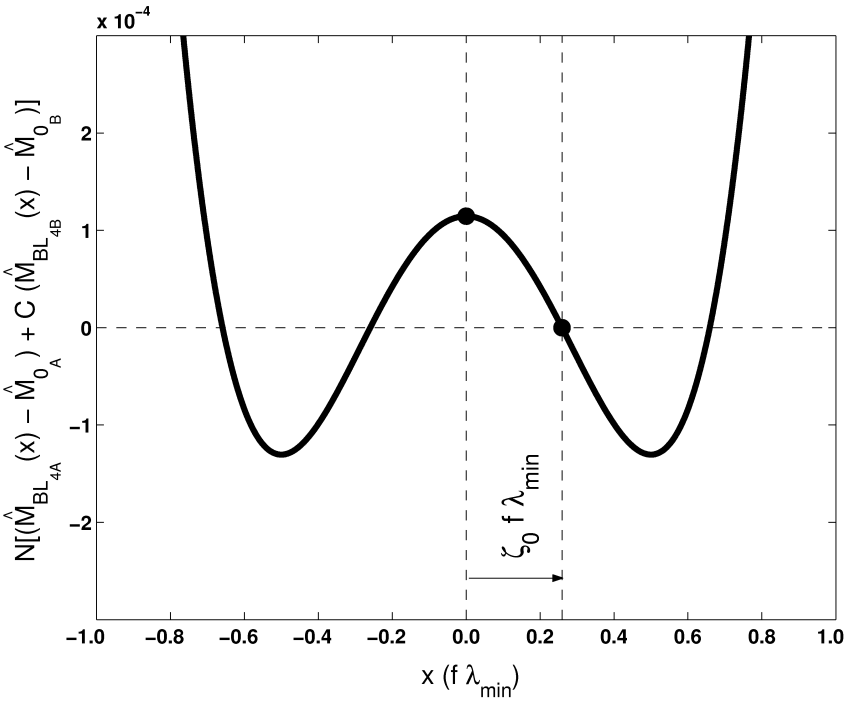


Figure 2-5. An example of the function $N[(\hat{M}_{BL_{4A}}(x) - \hat{M}_{0_A}) + C(\hat{M}_{BL_{4B}}(x) - \hat{M}_{0_B})]$ for an $m = 1$, $l = 3$ sampled mask. Choosing $\zeta = \zeta_0$ allows us to create a binary mask of contiguous stripes. Choosing $\zeta = 0$ allows us to create a graded mask with the most favorable optical density requirement.

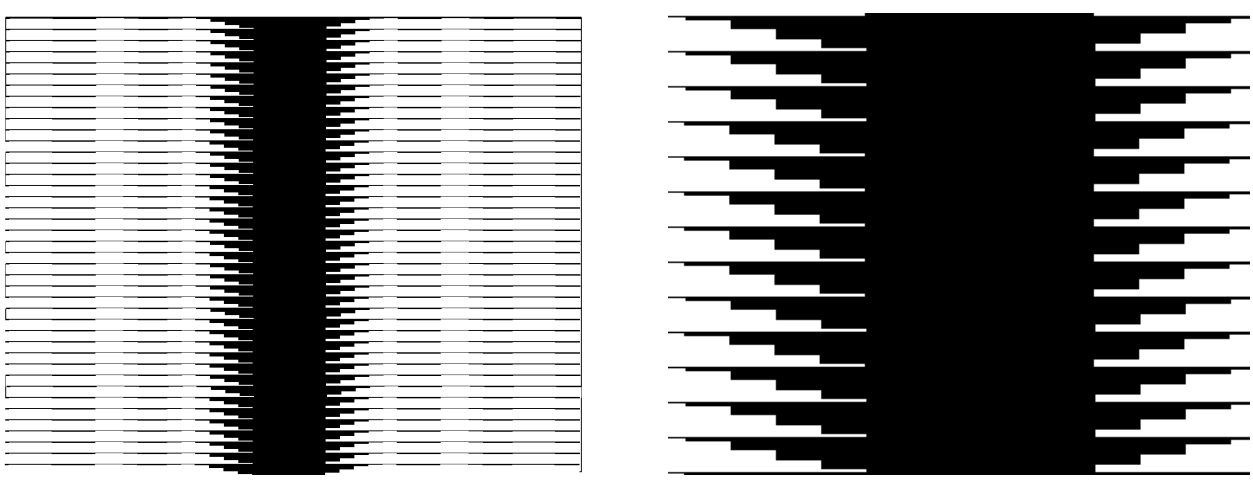

Figure 2-6. Simulated low and high magnification pictures of an $m = 1$, $l = 3$ linear eighth-order sampled binary mask. Dark areas are completely opaque and white areas perfectly transmissive. The high-magnification picture (right) illustrates the sampling. See §5 for microscope photographs of linear eighth-order binary masks.

For the $m = 1$, $l = 3$ mask with IWA $= 3\,\lambda_{max}/D$, spacing $\Delta x = \lambda_{min} f$, and bandpass 0.5–0.8 $\mu$m, we find that $\hat{M}_{0_A} = 0.00630889$, $\hat{M}_{0_B} = 0.01882618$, $C = -0.33935486$, and $\zeta_0 = 0.25941279$. Table 2.3.2 lists normalization constants and sampled mask parameters for eighth-order notch filter masks of various IWA's using a top-hat kernel, $\hat{P}(x) = (D/\lambda_{min})\Pi(xD/\lambda_{min})$, and 0.5–0.8 $\mu$m bandpass.

If the resolution of our nanotool is $\sim$ 20 nm, we require a telescope with an f/115 or slower beam (see Kuchner & Spergel 2003). The physical size of an entire mask is generally a few hundred diffraction widths. A 1" $\times$ 1" mask would consist of $\gtrsim$ 440 vertically repeating segments, where each segment is $\leq \lambda_{min} f = 57.5\ \mu m$ wide. This coronagraph design would have a Lyot stop throughput of 40%. Figure 2-6 shows an example of what an $m = 1$, $l = 3$ linear eighth-order binary mask would look like.

### 2.3.2 Sampled Graded Masks

Sampled graded masks may be easier to construct than smooth graded masks. Moreover, they can be designed so that they do not require their darkest regions to be perfectly opaque. This flexibility limits the demands on the lithography tool used to make the masks. The $1 - \mathrm{sinc}^2$ mask with IWA $= 2.9\,\lambda_{max}/D$, $\epsilon = 0.4$, can be built with a maximum optical density of 4. The $\sin^2$ mask with $\epsilon = 0.4$ can be built with a maximum optical density of 3.

When we design eighth-order graded notch filter masks, we can reduce the required maximum optical density by beginning the sampling at $\zeta = 0$, so long as our sampling size is large enough to straddle the valleys shown in Figure 2-5. Choosing $\Delta x = \lambda_{min} f$ satisfies this condition for all of the masks listed in Table 2.3.2. Figure 2-7 shows a graded version of the $m = 1$, $l = 3$ eighth-order mask described in §4.1. The mask is defined by $\hat{M}(x, y) = \hat{M}_{notch}(x)$; its optical density is $-\log_{10} |\hat{M}_{notch}(x)|^2$. To make the darkest stripe of the mask as transparent as possible, we chose $\zeta = 0$. With this choice, the darkest stripe of the mask has optical density $-2\log_{10} |\hat{M}_{notch}(0)| \approx 7.882$. Table 2.3.2 lists the maximum optical densities (O.D.$_{\mathrm{max}}$) of sampled graded masks with $\zeta = 0$.

Table 2-1. Sampled eighth-order mask parameters

| n | N[a] | $\theta_{IWA}$ ($\lambda_{max}/D$) | $\epsilon$ | $\hat{M}_{0_A}$ | $\hat{M}_{0_B}$ | $C$ | $\zeta_0$ | O.D.$_{\max}$[b] |
|---|---|---|---|---|---|---|---|---|
| 1 | 0.966115405054 | 3 | 0.453 | 0.01092315 | 0.01631996 | -0.67562610 | 0.25945500 | 8.004 |
| | 0.960497496515 | 4 | 0.340 | 0.00616927 | 0.00923329 | -0.67167174 | 0.25954657 | 9.012 |
| | 0.959860814806 | 5 | 0.272 | 0.00395309 | 0.00592117 | -0.66985758 | 0.25958912 | 9.791 |
| 2 | 0.999927046667 | 3 | 0.487 | 0.00632078 | 0.01883265 | -0.34113344 | 0.25944228 | 7.969 |
| | 0.999967637078 | 4 | 0.366 | 0.00357716 | 0.01068997 | -0.33769399 | 0.25953913 | 8.969 |
| | 0.999991487843 | 5 | 0.292 | 0.00227903 | 0.00682024 | -0.33609563 | 0.25958482 | 9.757 |
| 3 | 0.994355716928 | 3 | 0.533 | 0.00505061 | 0.02250740 | -0.22964671 | 0.25941276 | 7.860 |
| | 0.992967898001 | 4 | 0.400 | 0.00284944 | 0.01275232 | -0.22635050 | 0.25952294 | 8.868 |
| | 0.992249764357 | 5 | 0.320 | 0.00182510 | 0.00818418 | -0.22484879 | 0.25957404 | 9.649 |
| 4 | 0.999920502046 | 3 | 0.578 | 0.00445606 | 0.02640459 | -0.17384571 | 0.25937869 | 7.744 |
| | 0.999959029620 | 4 | 0.434 | 0.00251629 | 0.01499184 | -0.17065228 | 0.25950368 | 8.751 |
| | 1.000006649135 | 5 | 0.347 | 0.00160975 | 0.00961517 | -0.16919646 | 0.25956186 | 9.534 |
| $l$ (for $m = 1$) | | | | | | | | |
| 2 | 1.865785172445 | 3 | 0.557 | 0.00825681 | 0.01646433 | -0.50505400 | 0.25942680 | 7.923 |
| | 1.862096989484 | 4 | 0.412 | 0.00452972 | 0.00904463 | -0.50274761 | 0.25953456 | 8.977 |
| | 1.856230853161 | 5 | 0.334 | 0.00298028 | 0.00595415 | -0.50180101 | 0.25957920 | 9.710 |
| 3 | 1.434216871605 | 3[c] | 0.596 | 0.00630889 | 0.01882618 | -0.33935486 | 0.25941279 | 7.882 |
| | 1.429552473250 | 4 | 0.447 | 0.00355642 | 0.01063737 | -0.33669458 | 0.25952307 | 8.890 |
| | 1.427349701514 | 5 | 0.357 | 0.00227076 | 0.00679929 | -0.33546973 | 0.25957440 | 9.674 |
| 4 | 1.312506672966 | 3 | 0.637 | 0.00540801 | 0.02147409 | -0.25623997 | 0.25623997 | 7.813 |
| | 1.308947497039 | 4 | 0.478 | 0.00305104 | 0.01215389 | -0.25348152 | 0.25951079 | 8.819 |
| | 1.306220598720 | 5 | 0.382 | 0.00195033 | 0.00778076 | -0.25221408 | 0.25956647 | 9.603 |

[a]Normalization constant for $\zeta = \zeta_0$ and $f\lambda_{min}$ sampling.
[b]For a graded mask with $\zeta = 0$.
[c]Suggested for TPF-C.

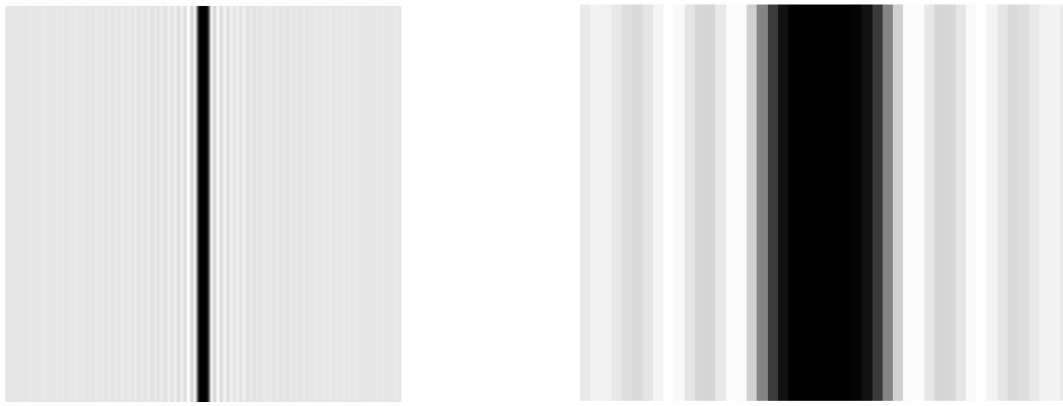

Figure 2-7. Simulated low and high magnification pictures of an $m = 1$, $l = 3$ linear eighth-order sampled graded mask with $\zeta = 0$. The low magnification picture (left) shows $\sim 400$ diffraction widths. Each stripe has uniform shading and is $f\lambda_{min}$ wide.

In summary, we conclude that eighth-order masks can control diffracted starlight while simultaneously offering resistance to tip/tilt and low spatial-frequency optical aberrations compared to fourth-order masks. This is confirmed with explicit lab tests in §5. Eighth-order masks also help to prevent leakage due to the finite size of stars, as is shown with numerical simulations in the next chapter. Graded designs can be fabricated with HEBS (High-Energy-Beam-Sensitive) glass, and notch-filter masks can be fabricated with HEBS glass or regular glass and a deposition of opaque material that is subsequently etched by an electron-beam lithography machine. We provided examples of sampled binary, smooth binary, and sampled graded eighth-order masks. The $m = 1$, $l = 2$ design is recommended for the TPF-C.

# CHAPTER 3
# PROSPECTS FOR SPACE OBSERVATIONS

This Chapter describes the technologies associated with a space-based internally occulting coronagraph that using band-limited image masks. Quasi-static wavefront errors and scattered light removal are first briefly described. Then, the performance of a TPF-C-like instrument is examined as a function of stellar angular diameter.

It is shown that incoherent light leakage resulting from the finite size of stars can be suppressed by using the eighth-order image masks from Chapter 2. This benefit enables sensitive imaging measurements of the circumstellar regions surrounding nearby evolved stars. We discuss the science that such observations can deliver regarding both terrestrial and Jovian exoplanets.

## 3.1 Introduction: Quasi-Static Wavefront Errors and "The Dark Hole"

The TPF-C will generate unprecedented contrast within several AU of nearby stars (see Traub et al. (2006) for a review). Currently, there are two different architectures undergoing feasibility studies: (i) an internal occulter that utilizes one (or more) of the promising designs mentioned in §1.3, and (ii) an external occulter design that utilizes a distant, specially shaped, star-shade that casts a dark shadow over the entire telescope (Cash (2006); Lyon et al. (2007)). Each have their advantages.

The internal occulter allows for integration of all optical components locally into a single instrument, whereas the external occulter must be separated from its detector by $\approx 50,000$ km, hence requiring a sophisticated orbital dynamics scheme. To maximize observing efficiency, the external occulter will also likely require at least two star-shades. While one is aligned, the other(s) will travel to the next target. The concept expends copious amounts of energy but is still less expensive than any internal occulting design by nearly a factor of 2, since it does not require as large a primary mirror. These practical and budgetary considerations along with the intended scope of the general astrophysics program will decide the TPF-C's architecture. Hybrid designs are also being considered.

For instance, a discovery-class instrument could eventually operate as the detector for a star-shade launched several years later (Shaklan & Levine 2007), or a closer-in star-shade could work in tandem with an internal occulter to save fuel.

Any internal occulter design will have to deal with wavefront phase and amplitude errors introduced by the telescope primary mirror and subsequent optics, such as beam-splitters, dichroics, condensers, filters, lenses, ... etc. The effects of these systematic disturbances manifest as slowly undulating, quasi-static speckles in the image plane (see §1.2.3) that change on a timescale commensurate with thermal fluctuations. Such aberrations are inherent to all of the coronagraphs mentioned in §1.3 and unavoidable at the contrast levels required for circumstellar science.

Speckle-nulling is the act of removing quasi-static residual starlight from a pre-selected region of the image plane. By including one or more deformable mirrors (DM's) in the optical train to reshape the phase of starlight (or, more generally, to alter the complex field), a sharply defined region of deeper contrast can be generated over a fraction of the search area. The size of this so-called "dark hole" is governed by the number of DMs and their actuator densities. This technique greatly improves the chances for direct detection by properly isolating the companion's signal.

As with most correction schemes, scattered light removal generally relies upon three steps: (i) wavefront sensing, (ii) wavefront reconstruction, and (iii) wavefront manipulation or control. The steps are often executed in succession and each may require the development of specialized algorithms to optimize the procedure for a given active optics system. For instance, from space it is possible to perform wavefront sensing at the science camera since the speckle lifetime is long compared to a typical integration. This approach requires phase diversity to reconstruct the shape of the wavefront but it minimizes non-common-path errors (§6.3) and the number of optics. Ground-based instruments, on the other hand, must sense the wavefront directly in order to keep pace with the rapidly changing field. In fact, high-contrast imaging instruments such as GPI

(Macintosh et al. 2006a) and the PALM-3k/P1640 (Dekany et al. 2007) will need to sense the wavefront twice, before and after the coronagraph, in order to generate a dark hole while simultaneously correcting for the atmosphere.

Figure 3-1 shows simulated images from a coronagraph operating in tandem with a single deformable mirror in broadband light after correction has been applied. The dark hole (hereafter, DH) is the central square region surrounding the star in the image. Its maximal extent, $s_{max}$, is related to the number of actuators across the DM by $s_{max} = (N_{act}/2)\ \lambda_{min}/D_{tel}$, where $N_{act}^2$ is the total number of actuators. The right-hand-side of the DH is deeper than the left because this simulation includes amplitude errors, which break the symmetry between the location of speckles on either side of the optical axis (see Bordé & Traub (2006)). Amplitude errors might be caused by reflectivity variations across a mirror for example. The complex field was reconstructed on the right-hand-side of the DH, so that is the side with optimal sensitivity.

The DM surface shape is calculated using an energy minimization technique invented by Give'On et al. (2007). We briefly describe the method as it would be used in practice. First, the electric field (phase and amplitude) at the detector is reconstructed by changing the shape of the DM several times with relatively arbitrary phase ripples – sines or cosines for instance. Then, the DM shape is commanded to be flat and each actuator is poked individually. The resultant wave is propagated through the coronagraph numerically (i.e. with a computer model) and the electric field at the detector is recorded each time. This data cube of electric fields is finally compared to the original electric field to provide a first estimate for the actuator heights. Several iterations converge upon the optimal shape.

Figure 3-2 shows an image of a 12x12 Boston Micromachines DM. The maximum surface stroke is 1.5 $\mu$m (3 $\mu$m max phase correction) and the electronics provide 14-bit resolution, corresponding to 1.5 $\mu$m / $2^{14} \approx 1\mathring{A}$ precision. This device will be used in laboratory experiments to test the theoretical predictions shown in the next section.

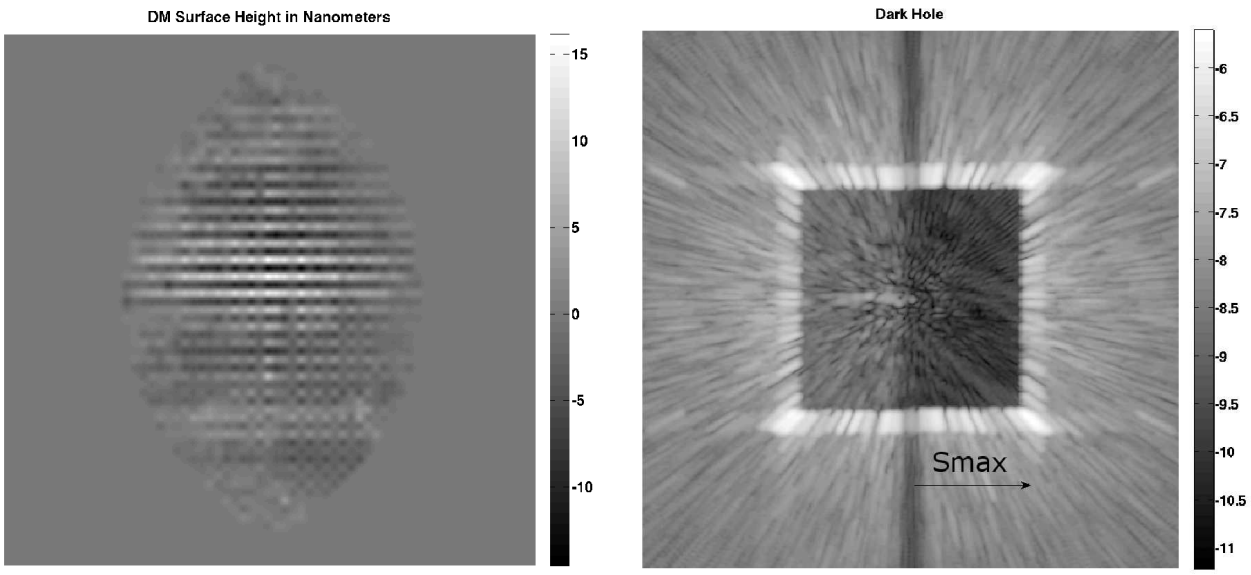


Figure 3-1. Simulated images of a 64x64 DM and resulting dark hole. The DM compensates for scattered starlight up to a spatial frequency equal to the Nyquist limit, in this case $s_{max} = 32\ \lambda_{min}/D_{tel}$ away from the optical axis. Contrast levels of order $10^{-10}$ are generated in the region on the right. Details of the model are discussed in §3.2.3.

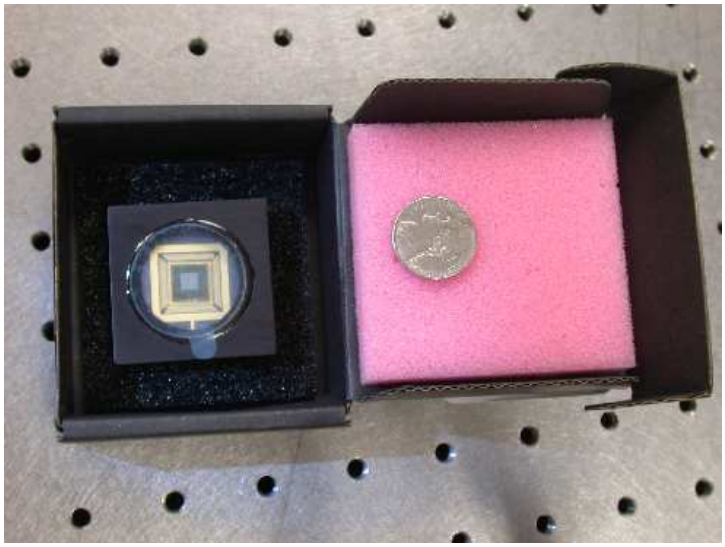

Figure 3-2. Boston Micromachines 12x12 deformable mirror. This device has recently been integrated into the University of Florida coronagraphic testbed.

## 3.2 Targeting Evolved Stars

The current preliminary TPF-C observing strategy is optimized to search for Earth-like planets orbiting a highly selective list of nearby F, G, and K main-sequence stars. In this section, we provide motivation for potentially expanding this set of targets to include evolved stars that subtend an appreciable angular size on the sky. To substantiate this concept, we calculate the light leakage resulting from the finite size of such stars in terms of contrast for one of the front-running TPF-C design candidates.

### 3.2.1 Motivation

To gain a fundamental understanding of planet formation and evolution, and to place the existence of Earth in the broadest possible context, a large and relatively unbiased sample of stars must be searched. This precept can be understood by considering the potential for diversity amongst extrasolar planetary systems. One notable effect is that the physical processes governing planet formation and evolution are nonlinear. Small changes in initial conditions can lead to large-scale differences in overall system architecture. As a result, stars of comparable mass and composition can yield a substantially dissimilar set of companions. Significant diversity is implicated on these grounds alone. This inherent complexity, however, is further amplified by the variety in stellar hosts that supply the material out of which planets originate. Their bulk characteristics are markedly disparate:

- the range of masses over the full span of the main sequence covers more than 3 orders of magnitude
- the range of metallicities in the solar neighborhood covers $\sim 1.5$ orders of magnitude (Luck & Heiter 2006, 2007)
- most stars are members of multiple systems (Tokovinin 2004)
- and individual stellar luminosities can vary by as many as $\sim 7$ orders of magnitude over a lifetime, when the red giant to early compact object stages of stellar evolution are included (Iben 1967; Iben & Laughlin 1989)

Given this information, there is no reason to expect that extrasolar planets will be any less unique or complex than the satellites of our solar system.

Direct imaging offers an efficient approach towards exploring this large parameter space for it is a technique whereby the members of entire planetary systems can, in principle, be detected and characterized simultaneously, depending on the separation and brightness of the inner-most companion. It is reasonable that sensitive space instruments, such as the TPF-C, TPF-I, and Darwin, consider a moderately comprehensive set of targets, otherwise a limited scope or severe predisposition to certain kinds of stars neglects large classes of interesting systems, including those that may tell us where to look next.

In addition to single main-sequence stars of intermediate spectral-type, which comprise the canonical list of high-contrast imaging targets, evolved stars, binaries, and M-dwarfs offer a variety of environments for testing theories of planetary science and other promising avenues in the search for life (Lopez et al. 2005; Haghighipour & Raymond 2007; Tarter et al. 2007). The motivation for observing them stems from their statistical significance: all stars will eventually evolve off of the main-sequence to become giants; binaries constitute approximately 50% of all stellar systems (Duquennoy & Mayor 1991); and M-dwarfs represent approximately 75% of all stars in the Galaxy (Henry 2004). Moreover, recent radial velocity, transit photometry, and astrometric observations have already provided strong evidence for the existence of planets in each category (Johnson 2007; Bonfils et al. 2007; Mugrauer et al. 2007, and references therein).

In this section, it is suggested that high-contrast imaging observations of different types of stars is more than just a compelling notion. The discussion focuses primarily on evolved stars (luminosity classes IV-I), their habitable zones, and the interface between "point" sources and resolved sources. As such, calculations of achievable sensitivity as a function of stellar angular diameter are provided for one of the leading TPF-C design candidates. It is shown that a Lyot coronagraph (Lyot 1939) with wavefront control (Trauger & Traub 2007) and access to an assortment of band-limited image masks (Kuchner & Traub 2002; Kuchner, Crepp, & Ge 2005) can handle a diverse set

of observations. This work is also relevant to close-separation visual binaries.[1] We do not deal with M-dwarfs since interferometers are likely required to access their narrow temperate surroundings.

### 3.2.2 Extended Sources

High-contrast imaging is contingent upon the destructive interference of starlight (§1.3). Losses in spatial coherence due to the finite size of a star, whose surface is comprised of many independently radiating elements, can therefore result in light leakage. This places a fundamental limitation on a coronagraph's sensitivity.

Many nearby stars subtend an appreciable angle on the sky compared to the spatial resolution of a large optical telescope. Evolved stars, in particular, have intrinsically large radii and may be several $\lambda\ /D_{tel}$ in width, even though they tend to be somewhat more distant than the closest main-sequence stars. For instance, Betelgeuse, the largest star in the Northern sky, $D_* = 55$ mas, illuminates an 'area of coherence' (Born & Wolf 1999) that is smaller than the primary mirror with which TPF-C may operate – only 2.3m in diameter when observed in quasi-monochromatic light centered on $\bar{\lambda} = 0.55\ \mu$m. For comparison, a star of radius $R_\odot = 6.96 \times 10^{10}$ cm located at 10 pcs would coherently illuminate an area of diameter $\sim$ 138 m. An interesting regime lies between these two values where: (i) the stars are marginally resolved and (ii) their habitable zones are extended but expanding at a rate slow enough to provide sufficient time for life to develop and proliferate.

#### 3.2.2.1 Imaging terrestrial planets

As stars evolve off of the main-sequence, their luminosity increases and the habitable zone widens as it moves outward. Planets that were previously too cold to support life

[1] It is possible to suppress the light from two stars simultaneously by employing a coronagraph with a linear attenuation profile. This principle has recently been demonstrated from the ground using adaptive optics (§7).

will warm. A recent study of the continuously habitable zone by Lopez et al. (2005) has shown that there are two eras of post-main-sequence evolution where hospitable conditions may persist. They occur during the sub-giant and horizontal branches. Terrestrial planets orbiting a solar mass star in the 2-9 AU range, before the Helium flash, and 7-22 AU range, after the Helium flash, may have moderate climates for $10^8 - 10^9$ years.

Life emerged on the Earth within the first $\approx 10^9$ years after formation (Lazcano & Miller 1996). However, progress was hindered by frequent asteroidal impacts. Life may have been extinguished several times, even as late as 800 million years after formation (Mayer & Stevenson 1988). This raises the question of whether life can arise significantly faster under quiescent conditions, such as those provided by an older planet that is member of a more dynamically inactive system. Spectroscopic measurements of terrestrial planets orbiting evolved stars at several AU can help to constrain this timescale.

More distant planets will, depending on their albedo and radius (see Seager et al. (2007) for a discussion of super-Earths), generally be fainter than the Earth-Sun system (contrast $\approx 2 \times 10^{-10}$; §1.2.1.1) in reflected light. A coronagraph can, however, accommodate for this effect by sacrificing spatial resolution. Observations at longer wavelengths decreases the intensity of quasi-static speckles by a factor of $\sim (\lambda/\lambda_0)^2$ in the search area. Another option is to increase the inner-working-angle. With a band-limited mask design, this results in higher Lyot stop throughput, which increases the amount of companion light, decreases integration time, and makes the point-spread-function (PSF) more spatially succinct.[2] Notice that both approaches, and combinations thereof, improve the coronagraph's resistance to stellar size.

Figure 3-3 shows how the habitable zone scales linearly with stellar angular size, a relationship that can be derived from the Stefan-Boltzman law. Members of the TPF-C

[2] Highly concentrated PSF's facilitate discrimination of companion light amongst diffuse zodiacal and exozodiacal dust emission.

"Top 100 List" (http://sco.stsci.edu/starvault/), red-giant stars within 30 pcs from Lopez et al. (2005), and sources from Ochsenbein & Halbwachs (1982) with large angular diameters, which were directly measured using interferometry, are included in the plot. The habitable zones of several dozen evolved stars are accessible in the near-IR. This is a lower-limit to the number of potential targets since the list is only representative and not complete. The habitable zone of super-giant stars, such as Betelgeuse and R Doradus, may be as large as an arcsecond, but they are likely too young for life to develop. Discovery-class missions that employ a small aperture cannot afford further sacrifices in spatial resolution but will be capable of detecting Jovian planets orbiting giant stars at visible wavelengths.

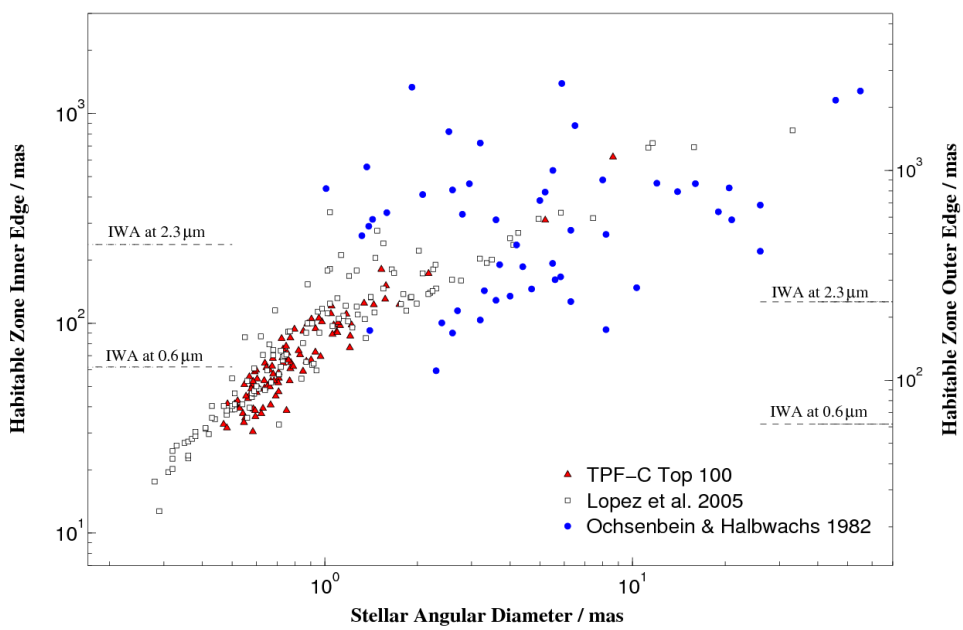


Figure 3-3. Inner and outer-edge of the habitable zone for nearby stars. Targets with a large angular diameter leak light through a coronagraph (§3.2.4) but also have more distant habitable zones. Observations in the near-IR, or with a coronagraph having a larger inner-working-angle (IWA), improve sensitivity at the expense of spatial resolution and permit the direct detection of terrestrial planets orbiting at several AU. The IWA's shown are for an 8m telescope operating at 4 $\lambda/D_{tel}$. To first order, the ratio of the habitable zone outer-edge distance to the inner-edge depends only on the temperature of water, $\mathrm{HZ_{outer}}/\ \mathrm{HZ_{inner}} \approx (373\ \mathrm{K}/\ 273\ \mathrm{K})^2 = 1.87$.

#### 3.2.2.2 Imaging Jovian planets

Precision RV measurements have now established baselines exceeding 10 years making possible the detection of Jovian planets orbiting several AU from their host stars. Not only are giant planets being discovered orbiting main-sequence stars, but they are also being discovered orbiting giant stars (Johnson et al. 2008), which rotate slowly and have sharp spectral features. Preliminary results have already revealed correlations between stellar mass and planet properties. For instance, more massive stars tend to produce more massive Jovian planets in wider orbits (Johnson 2007).

An example of such a system with a known exoplanet is the bright (V=1.15) K-giant $\beta$ Gem (POLLUX). RV observations spanning nearly 25 years are consistent with the presence of an $M\sin i = 2.6 M_{Jup}$ planet with a semi-major axis of 1.6 AU (Hatzes et al. 2006). $\beta$ Gem is a K0 III star at a distance of 10.3 pcs with an angular diameter of $7.96 \pm 0.09$ mas (Nordgren et al. 2001) and mass of $1.7 \pm 0.4\ M_{\odot}$ (Allende Prieto & Lambert 1999).

A space-based direct imaging instrument will be capable of fully characterizing such planets. Moreover, their orbit will already be determined and the spectra will have a high signal-to-noise ratio compared to terrestrial planets. As the sample of target stars on the high-mass-end of the stellar spectrum grows, we will acquire a better understanding of the planet formation process. In the following, we explore the challenges of generating sufficient sensitivity to detect planets orbiting partially resolved stars.

### 3.2.3 Numerical Simulations

We model a TPF-C-like instrument with code written in Matlab assuming an internally occulting Lyot-style design. The simulations are broadband and incorporate: primary mirror phase and amplitude errors, image mask phase errors, a single 64x64 actuator DM, and the finite size of the star. We assume that all optics are located in pupil or image planes and use Fourier transforms to propagate the electric field. The telescope is circular and unobscured.

Stars are modeled by a uniform disk of mutually incoherent point sources. Light from each source is sent through the optical train with a tip/tilt error that corresponds to its location on the stellar surface. The number of sources across the disk well exceeds the Nyquist frequency in $\lambda_{min}/D_{tel}$ units. The intensity from each add together at the detector to form the final image. Ten wavelength channels sample the various 100 nm wide bandpasses.

Primary mirror phase errors follow a broken power-law power-spectral-density (PSD) given by:

$$\mathrm{PSD}(k) = \frac{A_0}{1 + (k/k_0)^n} \tag{3–1}$$

where $A_0$ is a constant with units m$^4$, $k$ is the spatial frequency, $k_0 = 4$ cycles / m, and $n = 3$. This is the PSD typical of an 8m primary mirror (Shaklan & Green 2006; Bordé & Traub 2006). The mirror surface figure is scaled to have an rms value of 1 nm (2 nm in wave-front phase). Amplitude errors are modeled as white noise with an rms of 0.005 and maximum value of unity. We do not include scattering from other optics in the path other than the glass on the image mask.

Mask defects are included because different sections of the stellar surface fall onto different locations in the image plane. These non-common-path errors limit the achievable sensitivity since they cannot each be compensated for simultaneously; correcting for one may amplify another. The imperfections are modeled as uncorrelated phase errors, e.g. the worst case scenario.

We use both 4th-order and 8th-order linear band-limited masks to make a comparison study since they have different resistances to stellar size. Their amplitude transmissions follow sinc(..)$^2$ and $m = 1$, $l = 2$ profiles respectively (see §2 for details). The default inner-working-angle is 4 $\lambda_{max}/D_{tel}$.

The DM is placed at a pupil and its surface is shaped by a square grid of actuators that map perfectly onto the primary mirror. The influence of each actuator is modeled with a Gaussian function that drops to 6% of its peak value at the location of adjacent

actuators. The 64x64 system can correct for wavefront errors with spatial frequencies as high as 32 cycles per aperture, creating the dark-hole region shown in Fig. 3-1 that defines the search area. We sacrifice correction of the highest spatial frequencies, 30-32 cycles per aperture, to improve correction of the lower-order modes, further reducing the intensity of speckles close to the optical axis. A smaller search area can yield even deeper contrast, such as is done at the HCIT (Give'on et al. 2007), but here we are also interested in distant planets. The sensitivity is limited by DM fitting errors.

We calculate the optimal DM shape using the linear energy minimization algorithm developed by Give'On et al. (2007). The technique is quite general and relies upon accurate modeling of the coronagraph, electric-field reconstruction at the science camera, and a form of phase diversity to solve for the actuator heights. The procedure is efficient once a rather computationally expensive metric, the "G-matrix", is established for the optical system. It needs calculating only once, unless changes to the coronagraph are made. In this chapter, we use several different coronagraphs, of different order, bandpass, inner-working-angle, and size of mask phase errors, so had to utilize multiple processors in parallel (but with no message passing interface). The optimal DM shape is found using only the central (on-axis) portion of the star. The surface is then fixed – a DM cannot compensate for stellar size – and contrast is measured as a function of angular diameter.

Sensitivity calculations use information from a single image. The instantaneous contrast, $C$, is found using the formula in Green & Shaklan (2003), Shaklan & Green (2005), and Crepp et al. (2007), which we show here:

$$C(x,y) = \frac{I(x,y)}{I(0,0)\,|M(x,y)|^2}, \tag{3–2}$$

where $I(x,y)$ is the intensity at the coordinates, $(x,\ y)$, in the final image, $I(0,0)$ is the peak stellar intensity as would be measured *without* the image mask in the optical train, and $|M(x,y)|^2$ is the mask intensity transmission. Both $I(x,y)$ and $I(0,0)$ are measured with the Lyot stop in place. A linear mask has no dependence on $y$. We do not model the

integral field unit that will take low-resolution spectra and use this color information to discriminate between speckles and companions.

### 3.2.4 Contrast vs. Angular Size

We compare 4th and 8th-order masks in systems optimized for two different bandpasses at visible wavelengths, $\lambda = 0.5 - 0.6$ $\mu$m and $\lambda = 0.7 - 0.8$ $\mu$m, and a bandpass in the near-IR, $\lambda = 2.2 - 2.3$ $\mu$m. We also include a mask with a larger inner-working-angle and place limits on the size of mask phase errors as a function of stellar diameter. Results from our simulations are shown in Fig. 3-4. The smallest and largest targets from the TPF-C Top 100 list and the largest star in the sky, R Doradus, are shown for comparison. The upper horizontal axis of each plot also indicates the characteristic angular diameter of a variety of stars placed at 15 pcs.

The top panel of Fig. 3-4 shows how the 8th-order mask has a higher tolerance than the 4th-order mask to stellar angular size. This result makes intuitive sense since the 8th-order mask is less susceptible to tip/tilt errors (§2, 4, 5). Both masks, however, leak diffracted starlight before the stellar surfaces are fully resolved: 0.55 $\mu$m / 8m = 14.2 mas; 0.75 $\mu$m / 8m = 19.3 mas; 2.25 $\mu$m / 8m = 58.0 mas.

It is evident that the sensitivity improves at longer wavelengths according to the scaling relation $C \propto (\lambda_0/\lambda)^2$. For small stars, the instantaneous contrast in the near-IR is an order of magnitude deeper than in the visible, at the expense of a factor of 3-4 in spatial resolution. This trade-off is well justified for evolved stars with extended habitable zones. The relative improvement grows to several orders of magnitude with further increases in angular diameter.

We also notice that the largest TPF-C Top 100 List candidate target requires an 8th-order mask in the visible. One might guess that a star with an angular diameter of 8.6 mas is near the lower-end of the priority list; however, this star is ranked #1. It is $\alpha$ Centauri A.

Table 3-1. Physical parameters for the $\sim 5$ Gyr old $\alpha$ Centauri triple system. The third component, Proxima Centauri, is a distant M dwarf that appears to be weakly bound (Wertheimer & Laughlin 2006). The TPF-C rank is currently defined by the first-visit completeness per integration time (http://sco.stsci.edu/starvault/).

| $\alpha$ Cen | A | B | C |
|---|---|---|---|
| Spec. Type | G2 V | K1 V | M5.5 V |
| v mag | -0.01 | 1.35 | 11.1 |
| mass ($M_\odot$) | 1.11 | 0.93 | 0.12 |
| radius ($R_\odot$) | 1.24 | 0.87 | 0.15 |
| luminosity ($L_\odot$) | 1.60 | 0.45 | 0.0002 |
| [Fe/H] | 0.22 | 0.26 | -1.00 |
| a (AU) | 23.4 | 23.4 | $\approx$ 12,000 |
| e | 0.52 | 0.52 | ? |
| i | $79.2^{\mathrm{o}}$ | $79.2^{\mathrm{o}}$ | ? |
| diameter (mas) | 8.6 | 6.0 | 1.0 |
| TPF-C Rank | #1 | #2 | – |

In addition to the usual reasons for targeting the Sun's closest neighbor, $d = 1.35$ pcs, the $\alpha$ Centauri AB system offers a unique testing ground for planet formation theories. Depending on the orbital phase, the stars may be separated by 11.2-35.6 AU. Currently, it is not clear whether the presence of an intermediately spaced stellar companion promotes or inhibits formation, and the answer likely differs for terrestrial planets compared to Jovian planets. The leading theories of "core-accretion" (Lissauer & Stevenson 2007; Pollack et al. 1996) and "gravitational instability" (Durisen et al. 2007) must account for this extra source of radiation and gravitational perturbations. Thus, high-contrast imaging observations of $\alpha$ Centauri AB may help to discriminate between the two. Indeed, numerical simulations indicate that planets in the habitable zone, should they form in the first place, can remain stable provided the inclination angle between the stellar and planetary orbital planes is not large (Quintana et al. 2007). Table 3-1 lists the $\alpha$ Centauri system parameters.

The bottom panel of Fig. 3-4 compares 8th-order masks with different surface errors, $\sigma_{\mathrm{rms}} = 0.5$, 2.3, and 5.0 nm. An 8th-order mask with an IWA of 7.27 $\lambda_{max}/D_{tel} = 150$

mas is also shown. Each were optimized for the $0.7 - 0.8$ $\mu$m bandpass. The $\sigma_{rms} = 0.5$ nm, IWA=4 $\lambda_{max}/D_{tel}$ curve is the same from the upper panel.

Increases to the size of mask errors scatters more light into the dark hole. The relationship obeys a similar quadratic dependence, $C \propto (\sigma_{\mathrm{rms}}/\sigma_{\mathrm{rms}_0})^2$, as with the size of primary mirror phase errors and wavelength. Notice that the 0.5 nm $\rightarrow$ 2.3 nm case does not scale according to this relation, because the primary mirror phase errors, surface rms=1.0 nm, dominate.

Diffracted light from the mutually incoherent sources on the stars' surface quickly degrade contrast when the angular diameter exceeds 10 mas. The system with IWA= 7.27 $\lambda_{max}/D_{tel}$ passes more planet light and is also less susceptible to stellar size. Changes to the telescope diameter slide the curves in both graphs horizontally if we neglect differences in the manufacturing processes that change the PSD and thus the speckle pattern.

Table 3-2 displays a series of high-contrast images for three nearby stars of increasing angular diameter. The current inner and outer-edge of the habitable zone for each is overlaid for reference. Only half of the dark-hole is accessible since we include primary mirror amplitude errors and only one deformable mirror (Bordé & Traub 2006). The gray-scale is on a logarithmic stretch and indicates the value of $I(x, y)/I(0, 0)$.

The images qualitatively verify the results from Fig. 3-4. Starlight leakage is a serious problem for the 4th-order mask in both visible bandpasses, whereas the 8th-order mask is able to suppress the light from extended sources to more acceptable levels. Sacrificing spatial resolution by conducting observations in the near-IR provides a substantial improvement in dark-hole depth and resistance to stellar size. Equipping the TPF-C with a near-IR camera can increase the signal-to-noise ratio of spectra, enable the detection of more distant planets, and complement visible light observations.

These considerations also suggest that near-IR observations may be more appropriate for accessing the habitable zone of the TPF-C's highest priority target, $\alpha$ Centauri A.

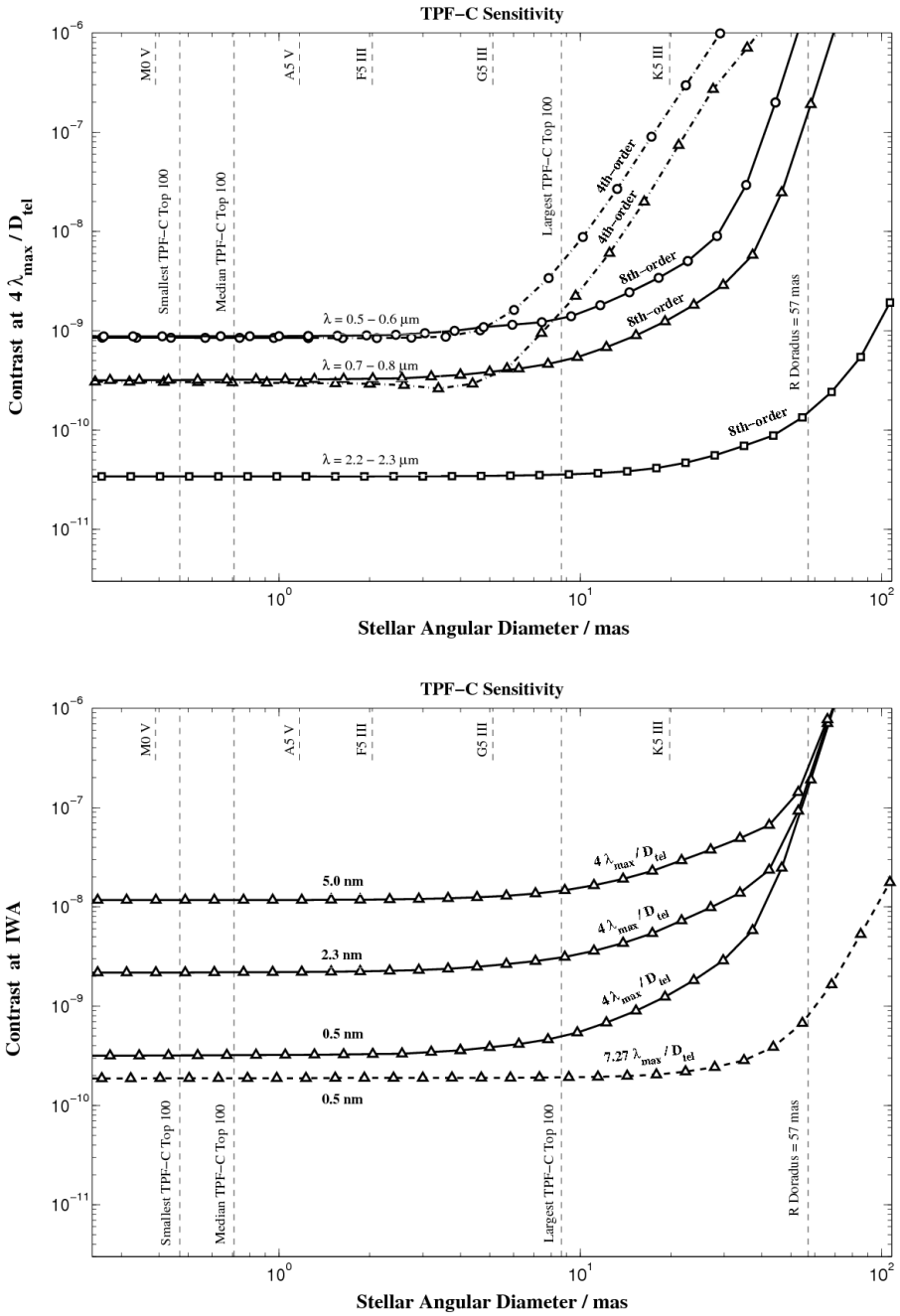


Figure 3-4. TPF-C stellar angular diameter sensitivity for an 8m telescope. The characteristic size of various stars placed at 15 pcs are shown across the top axis for reference. R Doradus is the largest star in the sky. The largest TPF-C Top 100 star, $\alpha$ Centauri, also has the highest priority. Triangles represent $\lambda = 0.7 - 0.8$ $\mu$m data. To avoid confusion between curves, the near-IR 4th-order mask result is not shown.

Table 3-2. High-contrast images of stars with large angular diameters. The gray-scale is on a log-stretch and shows the value of $I(x,y)/I(0,0)$.

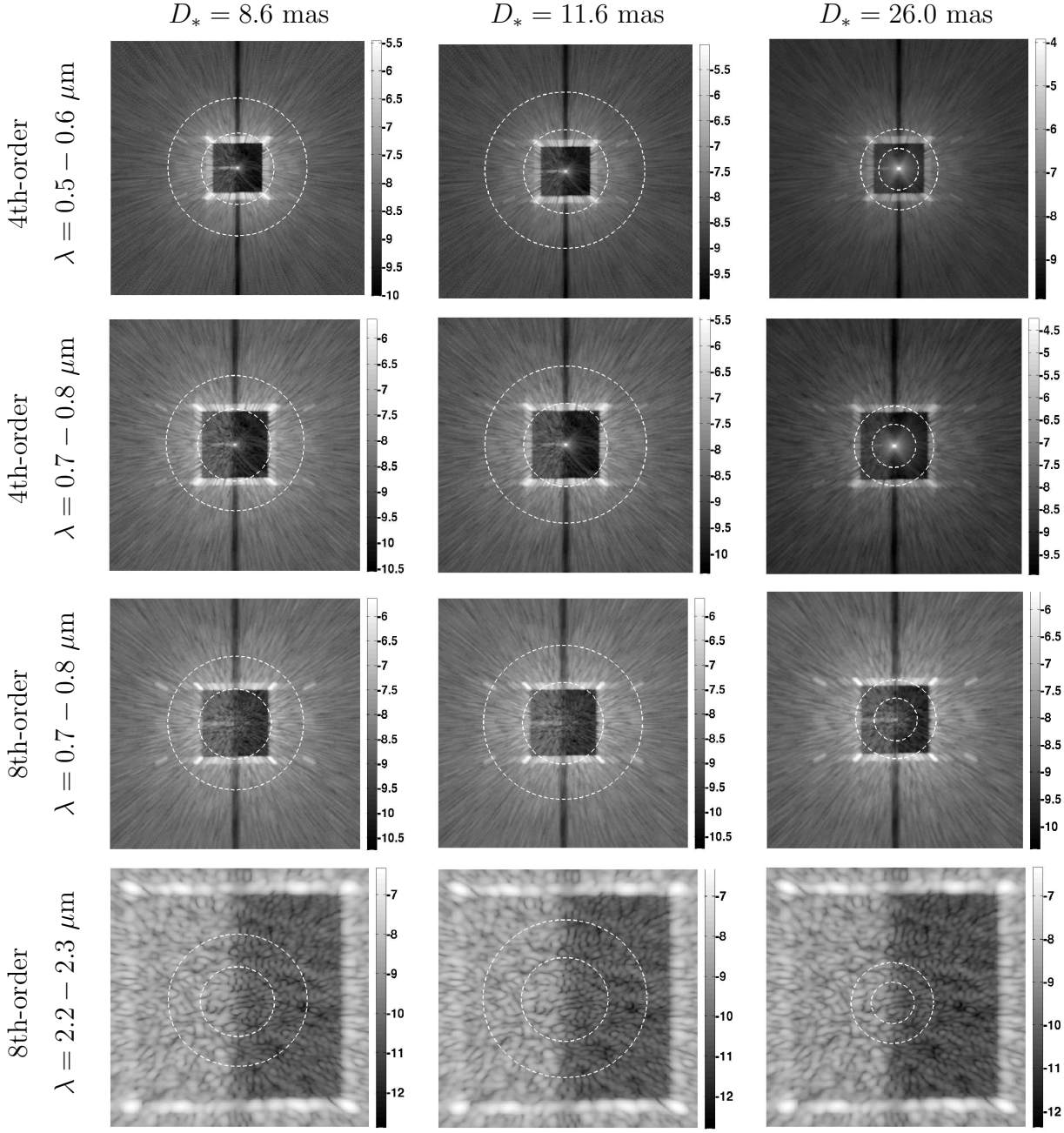


| $\alpha$ Cen A, TPF-C #1 | HD 124897 | HD 146051 |
|---|---|---|
| G2 V | K1.5 III | M0.5 III |
| $d = 1.4$ pcs | $d = 11.3$pcs | $d = 52.2$ pcs |
| $\mathrm{HZ_{inner}} = 0.8$ AU | $\mathrm{HZ_{inner}} = 8.2$ AU | $\mathrm{HZ_{inner}} = 19.1$ AU |
| $\mathrm{HZ_{inner}} = 1.6$ AU | $\mathrm{HZ_{outer}} = 15.5$ AU | $\mathrm{HZ_{outer}} = 36.1$ AU |

Otherwise, a DM with more than 64x64 actuators may be required. Near-IR observations of evolved stars are preferable when searching for the reflected light of distant terrestrial planets. It is possible to detect planets orbiting HD 146051 in the visible, as well as targets with similarly large angular diameters, but an 8th-order mask is necessary.

### 3.2.5 PSF Role-Subtraction

Depending on the bandpass, the signal of many terrestrial planets may lie just beneath the instantaneous noise floor, even inside the darkest regions of the dark-hole. Point-spread function (PSF) subtraction can enhance the effective contrast by more than an order of magnitude and help to discriminate between planets and speckles. Figure 3-5 illustrates the technique.

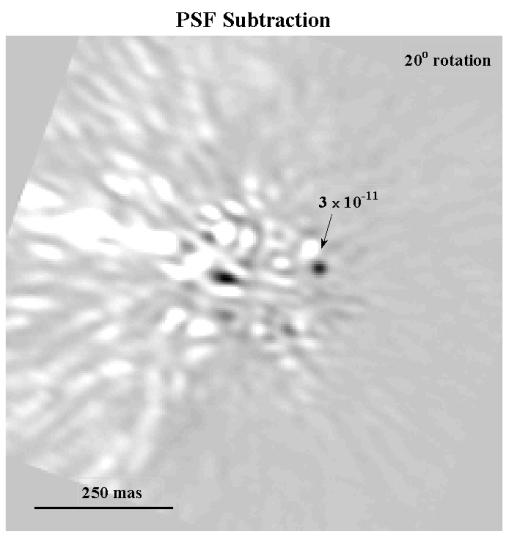


Figure 3-5. PSF subtraction enables unambiguous detection of planets that are fainter than the instantaneous noise floor.

Our PSF subtraction model combines images that differ by a small role-angle through which the telescope rotates. Since the wavefront errors are produced solely by the telescope and instrument optics, the speckle pattern rotates by the same amount. Companions, however, do not move. When the images are differenced, the speckles cancel and companions generate two characteristic spots, one dark and one bright, that are separated by the role-angle. The technique relies on the stability of the environment.

In space, the speckle lifetime is sufficiently long to preserve the structure of sequential images.

We added two sources of realistic noise that limit the subtraction of scattered light from within the dark-hole. The first and most consequential affect is thermal changes to the system that occur during and in between exposures. They were modeled by adding low-order aberrations to the previously optimized wavefront. Equal contributions from the first 10 Zernike modes were combined to form a wavefront that differed by 10 picometers rms in phase. We also added 5 e- / pixel of rms read noise to each image.

Fig. 3-5 demonstrates the detection of a terrestrial planet that is $3 \times 10^{-11}$ times as bright as its host star in the $\lambda = 0.7 - 0.8$ $\mu$m band. The separation is 6 $\lambda_{max}/D_{tel}$ and an 8th-order mask was used. The star has an angular diameter of 0.709 mas – the median value of TPF-C Top 100 List targets. The planet is not detectable in a single image using these parameters.

We also performed PSF subtraction with larger stars. The purpose of the experiment was to determine whether the speckle noise floor, which is presumably smoother for resolved sources, can be subtracted out with higher precision. We find that the improvement is negligibly small, of order a few percent for an $D_{tel} \leq 8$m primary mirror in the visible.

## 3.3 Conclusions

We have quantified the sensitivity of a space-based coronagraph as a function of stellar angular diameter. Observations of resolved sources would complement the TPF-C baseline strategy by sampling planet formation as a function of stellar mass. Detections of terrestrial planets in the extended habitable zones of sub-giant and horizontal giant-branch stars can place constraints on the timescale for the development of life. It is also possible to study previously clement planets that are now located interior to the habitable zone. These hot companions would provide a lab for investigating the run-away green house effect and making comparisons to Venus. Forecasts regarding Earth's eventual fate are

also implicit. The radial velocity technique has detected many Jovian planets with orbital separations exceeding 1 AU. Their physical characteristics, surface gravity, chemical composition, and effective temperature could be measured.

Our results show that a fourth-order mask leaks starlight for the TPF-C's highest priority star, $\alpha$ Centauri A. Observations with an 8th-order mask generate sufficient levels of contrast for this star and even larger targets. However, the outer-edge of the dark-hole generated by a 64x64 DM truncates critical regions of the search area. Near-IR observations can help remedy the situation; they would also provide complementary spectra, increase the signal-to-noise ratio for characterization, and quite naturally enable studies of distant terrestrial planets orbiting giant stars.

# CHAPTER 4
# PROSPECTS FOR GROUND-BASED OBSERVATIONS

As adaptive optics technology continues to improve, the stellar coronagraph will play an ever increasing role in ground-based high-contrast imaging observations. Though several different image masks exist for the most common type of coronagraph, the Lyot Coronagraph, it is not yet clear what level of wavefront correction must be reached in order to gain, either in starlight suppression or observing efficiency, by implementing a more sophisticated design. In this chapter, we model image plane Lyot-style coronagraphs and test their response to a range of wavefront correction levels, in order to identify regimes of atmospheric compensation where the use of hard-edge, Gaussian, and band-limited image masks becomes observationally advantageous. To delineate performances, we calculate the speckle noise floor mean intensity. We find that apodized masks provide little improvement over hard-edge masks until on-sky Strehl ratios, $S$, exceed $\sim 0.88\, S_{qs}$, where $S_{qs}$ is the intrinsic Strehl ratio provided by the optical system. Above this value, 4th-order band-limited masks out-perform Gaussian masks by generating comparable contrast with higher Lyot stop throughput. Below this level of correction, hard-edge masks may be preferentially chosen, since they are less susceptible to low-order aberration content. The use of higher-order band-limited masks is relegated to situations where quasi-static residual starlight cannot be sufficiently removed from the search area with speckle-nulling hardware.

## 4.1 Introduction

In recent years, great strides in the development of adaptive optics (AO) technology have ushered in a new era of high resolution diffraction-limited imaging. Despite these advances, the ability of the stellar coronagraph to generate deep contrast remains limited by insufficient levels of wavefront control: uncorrected phase and amplitude errors induced by the atmosphere and instrument optics manifest as bright, dynamic 'speckles' of scattered light in the search area. Even the most basic coronagraph, a Lyot coronagraph

equipped with a focal plane hard-edge occulter (Lyot 1939), is incapable of reaching its peak performance when coupled to state-of-the-art AO (Oppenheimer et al. 2004).

Numerous high-contrast observations have been conducted using AO on the world's largest telescopes (Marois et al. 2006; Mayama et al. 2006; Itoh et al. 2006; Carson et al. 2005; Close et al. 2005; Metchev & Hillenbrand 2004; Debes et al. 2002; Liu et al. 2002, and references therein); some rely solely on AO imaging, while others combine AO with coronagraphy[1] and/or speckle reduction techniques. These efforts have provided the first image of a candidate extrasolar planet (Chauvin et al. 2005a), as well as direct detections of sub-stellar companions near the planet-brown dwarf boundary (Biller et al. 2006; Neuhäuser et al. 2005; Chauvin et al. 2005b), as shown in §1. However, to image older, less-massive, and closer-in companions from the ground, wavefront sensing and correction techniques must improve substantially.

"Extreme" advances in high-contrast imaging technology are anticipated in the coming years. Deformable mirrors employing several thousand actuators and wavefront sensing of laser guide stars can, in principle, drive Strehl ratios above 90% on 8-10m class telescopes. With the proper coronagraph, these systems will be capable of detecting the near-IR emission of Jovian planets over a broader range of ages, masses, and separations (Macintosh et al. 2003). Extremely large telescopes such as the proposed Thirty Meter Telescope (TMT) (Macintosh et al. 2006b; Troy et al. 2006; Ellerbroek et al. 2005) and 100m OverWhelmingly Large telescope (OWL) (Brunetto et al. 2004) will improve spatial resolution, and hence the inner-working-angle (hereafter IWA) on the sky.

An interesting and more immediate alternative, which uses current AO technology, can also provide highly corrected wavefronts by instead sacrificing spatial resolution in

[1] Interferometers are likewise capable of suppressing starlight, and generally have a better inner-working-angle but a more restricted search area (Absil et al. 2006; Serabyn et al. 2005).

return for improved pupil sampling. Serabyn et al. (2007) have demonstrated K-band Strehl ratios approaching 94% by reimaging a 1.5m diameter circular unobstructed subaperture of the Hale 200-inch telescope onto the existing deformable mirror via relay optics. Combining this technique with a coronagraph that has an intrinsically small IWA ($< 3\,\lambda/D$) shows promise for generating deep contrast for separations as close as $\sim$ 0.5" (§6).

These considerations motivate the need for a quantitative understanding of how the stellar coronagraph's utility will depend on future gains in AO proficiency. To address this topic, we have modeled systems that are equipped with a variety of amplitude image masks, and examined their performance in a broad, nearly continuous range of corrected wavefront levels. In essence, we seek to provide a concise guide to the use of Lyot-style image plane coronagraphs. Most notably, we answer the question: "What is the appropriate choice of image mask for an extreme AO system operating at a given Strehl ratio?".

Mask performances are compared by calculating the direct output of the coronagraph, i.e. the mean intensity, with the understanding that differential and post-processing techniques can always be used on top of direct imaging to improve the prospects for discovery.

### 4.2 Model of Atmosphere & Wavefront Correction

The theoretical model used for our simulations consists of an extreme AO system linked in series to a Lyot coronagraph that is observing a stellar point source. Wavefront correction levels spanning from not quite diffraction limited ($\sim$ 77% Strehl) to highly corrected ($\sim$ 96% Strehl) are generated with an IDL routine based on simulations described in Carson et al. (2005). The code is optimized to simulate the operation of PHARO (Hayward et al. 2001) with the PALAO system (Troy et al. 2000) on the Hale 200-inch telescope at Palomar.

To clearly elucidate the sometimes subtle differences in performance between coronagraphic image masks, we restrict our analysis to monochromatic light ($\lambda = 2.2\,\mu m$), and ignore the effects of central obstructions, their support structures, and inter-segment mirror gaps. To first order, the addition of each of these complexities can be understood by convolving the telescope entrance aperture with the spatial frequency spectrum of the mask, and observing the resultant light distribution in the Lyot plane (§1.3). The net effect is often simply a loss in off-axis throughput, as the Lyot stop size is necessarily reduced to reject the additional diffracted starlight. Abe et al. (2006), Sivaramakrishnan & Yaitskova (2005), Sivaramakrishnan & Lloyd (2005), Soummer (2005), and Murakami & Baba (2005) discuss the prospects for Lyot coronagraphy with non-trivial entrance aperture geometries. We use a circular unobstructed entrance aperture, radial image mask, and (hence) a circular Lyot stop.

Kolmogorov phase screens mimic the effects of atmospheric turbulence, where a fixed Fried parameter of 20 cm at 2.0 microns, which has previously been found to best match actual PHARO data (Carson et al. 2005), is used throughout. To emulate AO correction, the phase screens are Fourier transformed, multiplied by a parabolic high-pass filter (Sivaramakrishnan et al. 2001; Makidon et al. 2005), and then inverse-transformed. Improving the degree of wavefront correction is accomplished by increasing the actuator density, which, in turn, raises the critical frequency of the high-pass spatial filter. The linear number of actuators across the pupil ranges from 35 to 94 (962 to 6939 total actuators). In terms of root-mean-square (rms) residual error, this provides a range in correction from $\lambda/13$ to $\lambda/30$.

The resulting AO-corrected wavefronts are then sent to a separate MATLAB coronagraph code for analysis, where the starlight passes through a series of consecutive pupil and image planes. We assume idealized interactions with the optical elements and the image mask (i.e. no scattered light, dust, fabrication errors, ... etc.), and use scalar diffraction theory to calculate the propagation of the electric field. The telescope pupil

is constructed as a perfect disk of unit transmission and diameter 512 pixels placed at the center of a 3072 x 3072 padding matrix in order to provide sufficient image plane resolution (6 pixels per $\lambda/D$). This choice of matrice sizes results in numerical noise levels below $10^{-12}$ in contrast, which is negligible compared to the physical speckle noise floor set by the AO system.

We do not explicitly simulate speckle-nulling on top of atmospheric correction. Instead, in §4.3.1 and §4.3.2, we assert that the quasi-static aberrations are compensated for to the level of the noise floor mean intensity set by diffraction and the atmosphere, for a given AO actuator density. Speckle-nulling is discussed more in depth in §4.3.3. This assumption is justified given the HCIT laboratory experiments at JPL that demonstrate removal of residual starlight to contrast levels below $10^{-9}$ within the fractional search area; although, in practice more timely methods for finding the optimal shapes of the extra DMs (preferably $< 1$ minute) will need to be employed.

## 4.3 Comparative Lyot Coronagraphy

Our study focuses on the subclass of Lyot coronagraphs that control diffracted starlight with amplitude image masks - that is, focal-plane masks that do not modulate the phase of transmitted light in theory.[2] Such masks reside in the focal-plane wheel of many coronagraphs in operation at major observatories. Among the choices of amplitude image masks, band-limited masks (Kuchner & Traub 2002) can perform the best in principle. In the ideal case, they diffract *all* transmitted on-axis starlight into a narrow region surrounding the edges of the Lyot pupil, and leave an area of infinite dynamic range in the center (§2). Moreover, band-limited masks with arbitrarily broad central nulls can

[2] Masks that manipulate the phase of starlight in the image plane generally have better inner-working-angles but poorer broadband performance (Roddier & Roddier 1997; Rouan et al. 2000); although, fully achromatic designs are being developed (Mawet et al. 2005, e.g.). See Guyon et al. (2006) for a review of the myriad of other different coronagraphic designs and how they compare in a space-based application, such as the TPF-C.

also be constructed (Kuchner, Crepp, & Ge 2005), and have been shown to help combat low-spatial-frequency optical aberrations in numerical simulations (Shaklan & Green 2005) and in laboratory experiments (§5; Crepp et al. (2006)).

We include a hard-edge mask, a Gaussian mask, and band-limited masks (hereafter, BL mask or BLM) with 4th-order ($\mathrm{sinc}^2$), 8th-order (sinc, $\mathrm{sinc}^3$), and 12th-order (sinc, $\mathrm{sinc}^2$, $\mathrm{sinc}^3$) intensity transmission profiles near the optical axis (Figure 1). Each mask is azimuthally symmetric and designed with an IWA $= 4\ \lambda/D$, so as to make fair comparisons. The IWA is defined as the half-width-at-half-maximum of the intensity transmission profile; for these masks, this value differs by less than 1% from the equivalent width, which can also be used as an alternative definition (Aime 2005). The masks are not truncated in the image plane; in practice, it is easy to include enough resolution elements such that this effect does not contribute significantly to the noise floor. Equations describing the masks are shown below. The radial coordinate, $r$, measures the distance from the optical axis, where $\tilde{r} = r\ D/\lambda$. Constants, which can be derived from (Kuchner, Crepp, & Ge 2005), are given to four decimals of precision. The amplitude transmissions, $M(r)$, are:

$$M_{\mathrm{H}}(r) = \mathrm{circ}\,(\tilde{r}/4) \tag{4–1}$$

$$M_{\mathrm{G}}(r) = 1 - e^{-(\tilde{r}/3.6097)^2}, \tag{4–2}$$

$$M_{\mathrm{BLM}_{4th}}(r) = 1 - \mathrm{sinc}^2(0.4500\ \tilde{r}), \tag{4–3}$$

$$\begin{aligned} M_{\mathrm{BLM}_{8th}}(r) &= 0.9485 + 0.4743\ \mathrm{sinc}(1.4043\ \tilde{r}) \\ &\quad - 1.4228\ \mathrm{sinc}^3(0.4681\ \tilde{r}), \end{aligned} \tag{4–4}$$

$$\begin{aligned} M_{\mathrm{BLM}_{12th}}(r) &= 0.7526 - 0.9408\ \mathrm{sinc}(1.9006\ \tilde{r}) \\ &\quad + 5.2684\ \mathrm{sinc}^2(0.9503\ \tilde{r}) \\ &\quad - 5.0802\ \mathrm{sinc}^3(0.6335\ \tilde{r}), \end{aligned} \tag{4–5}$$

where circ $(\tilde{r}/a)$ is a step-function equal to zero for $\tilde{r} \leq a$ and unity elsewhere.

To provide intuition for each mask's potential performance, we first present coronagraph simulations using perfect incident wavefronts (Fig. 4-2). A qualitative understanding of the coronagraph's functionality can be gleaned by examining the light distribution pattern in the Lyot pupil plane, since the total amount of rejected starlight depends strongly on the Lyot stop size and shape. For hard-edge and Gaussian masks, the contrast is limited by residual diffracted starlight, whereas the combination of a BLM with a matching Lyot stop can completely remove all on-axis starlight, in this ideal case. This capability is seen in the 4th-, 8th-, and 12th-order BLM mask final image plane patterns; they are composed entirely of numerical noise.

"Degeneracies" in contrast can occur however when large phase errors are present. In other words, different masks may generate indistinguishably similar levels of contrast when uncorrected atmospheric scattered starlight, rather than diffracted starlight, is the dominant source of noise. Under these circumstances, throughput, quasi-static aberration sensitivities, and fabrication considerations should more heavily influence the decision for which mask to implement in practice.

In the following sections, image mask performances are quantified in terms of these parameters and as a function of AO system correction. References to both the rms wavefront error (WFE), $\sigma_{AO}$, in the pupil plane and resulting Strehl ratio, $S_{AO}$, in the image plane are made. The relationship $S_{AO} \approx 1 - (2\pi\sigma_{AO})^2$ is valid in the high Strehl regime, and is adopted for our calculations. We begin by comparing hard-edge masks to the class of graded or apodized masks as a whole.

At this point it is convenient to define contrast, $C(r)$, as it will be used throughout the remainder of the text:

$$C(r) = \frac{I(r)}{\hat{I}(0)\,|M(r)|^2}, \tag{4–6}$$

where $I(r)$ is the intensity at the radial coordinate in the final image, $\hat{I}(0)$ is the peak stellar intensity as would be measured *without* the image mask in the optical train, and $|M(r)|^2$ is the mask intensity transmission. Note that $I(r)$ and $\hat{I}(0)$ are both measured

with the Lyot stop in place. This is the non-differential (i.e non-SDI, single roll-angle, ... etc.) contrast.

### 4.3.1 Hard-Edge vs. Apodized Image Masks

A stellar coronagraph will begin to noticeably improve contrast relative to standard AO imaging only when a sufficient amount of starlight is concentrated in the Airy pattern central core. This occurs at Strehl ratios as low as 50%; however, substantial gains over a significant fraction of the search area are not attained until the Strehl ratio exceeds $\sim 80\%$ (Sivaramakrishnan et al. 2001). We seek to identify the required level of wavefront correction above this value where apodized masks begin to out-perform hard-edge masks.[3]

For this comparison, we hold the Lyot stop size fixed at 60% throughput; images from the Lyot Plane column in Fig. 4-2 and results from §4.3.2 help to clarify why this is a useful simulation control. Contrast curves for the hard-edge, Gaussian, and 4th-order BLMs are shown in Figure 4-3 using several different levels of wavefront correction. For clarity, higher-order BLMs are not included here, but are discussed in the next sections. They provide intermediate levels of contrast, between that of the hard-edge and the 4th-order BLM.

At $\sim$ 77% Strehl (rms WFE = $\lambda/13$), the advantage in using the image plane coronagraph is evident only for separations smaller than $\sim 8\ \lambda/D$; this is a result of the limited wavefront correction and reduced aperture stop in the Lyot plane. Moreover, the Gaussian and 4th-order BLMs provide only a factor of $\sim 1.6$ improvement over the hard-edge occulter at the IWA, and contrast degeneracy sets in at a distance of $\sim 1.5\,\lambda/D$ from there. As AO correction improves, starlight is redistributed from the scattered light halo into the Airy diffraction pattern, the PSF 'shoulder' drops and extends, and the

[3] Notice that the IWA is rather loosely defined, and apodized masks can, in principle, work interior to the hard-edge mask. This benefit is likely difficult to exploit in practice, but constitutes an important caveat to the analysis.

diffracted light limitations of the hard-edge mask are revealed. The sharp edges of the mask prevent further improvements in contrast below $\sim 10^{-4}$ at the IWA, even as Strehl ratios exceed $\sim 88\%$.

The Gaussian and 4th-order BLMs, which more effectively diffract starlight onto the opaque portions of the Lyot stop, are capable of generating contrast levels of $\sim 6 \times 10^{-6}$ at IWA $= 4\ \lambda/D$ with $\sim 94\%$ Strehl. They provide an improvement in contrast at the IWA over the hard-edge mask by factors of approximately 2.7 at $\sim$ 82% Strehl (rms WFE $= \lambda/15$), 5.1 at $\sim 88\%$ Strehl (rms WFE $= \lambda/18$), and 21.7 at $\sim 94\%$ Strehl (rms WFE $= \lambda/26$). These results are consistent with the hard-edge versus Gaussian mask lab experiments of Park et al. 2006, taking into consideration the differences in PSF structure and IWAs.

Curves showing contrast at the IWA and the relative improvement are shown in Figure 4-4 as a more continuous function of wavefront correction. Though Gaussian and 4th-order BLMs out-perform the hard-edge occulter at currently achievable Strehl ratios, they remain degenerate with one another into the realm of extreme AO. We next identify the conditions and parameters for which this performance degeneracy is broken.

### 4.3.2 Gaussian vs. Band-Limited Masks

In order to compare apodized masks to one another, consideration of the light distribution pattern in the Lyot pupil plane must be made. It is clear from the previous section that Gaussian masks are competitive with BLMs in terms of contrast even at very high Strehl ratios. Thus, we can use the Lyot plane patterns shown in the third column of Fig. 4-2 for qualitative guidance.

Consider the effect of changing the Lyot stop diameter, $D_L$, for each of the apodized masks. With small non-zero stop sizes, the contrast at a given location on the detector is governed by the competing effects of speckle noise intensity and the achievable peak intensity of an off-axis source. The speckle noise intensity scales as $D_L^2$, whereas the companion peak intensity, $\hat{I}(0)\ |M(r)|^2$, scales as $D_L^4$. The result is a net improvement in

contrast and the apodized masks perform comparably, until $D_L$ grows large enough to leak significant levels of diffracted starlight.

As the Lyot stop size increases further, the contrast generated by BLMs does not degrade in as smooth a fashion as the Gaussian mask, since the diffracted light is tightly concentrated into a small region that follows the contour of the telscope entrance aperture. Instead, the transition away from optimal performance is more abrupt. The width of the transition region in the Lyot plane narrows as the wave front correction improves, and the transition occurs at progressively smaller Lyot stop sizes for masks of higher-order (8th-, 12th-, ... etc.).

These effects are seen in Figure 4-5, where we plot contrast at the IWA against Lyot stop throughput for two levels of wavefront correction. At $\sim$ 90% Strehl (rms WFE $= \lambda/20$), the apodized masks are clustered to within an order of unity in contrast from one another, but clearly out-perform the hard-edge occulter. At $\sim$ 96% Strehl (rms WFE $= \lambda/30$), the apodized mask performance degeneracy is broken, and optimum Lyot stop sizes become more evident. In particular, the 4th-order band-limited mask affords an $\sim$ 10% gain in Lyot stop throughput over the Gaussian mask (60% vs. 50%). The 8th-order and 12th-order masks generate slightly worse contrast and with $\lesssim$ 40% and $\lesssim$ 15% throughput respectively. These exact values depend upon the entrance aperture geometry, operating bandwidth, IWA, mask-function, and mask-type (linear, radial, or separable), but the trend is nevertheless the same at this level of wave front correction.

Generating Strehl ratios beyond 96% on large ground-based telescopes in the near future is rather unlikely.[4] Additional complications such as differential chromatic wavefront sensing and correction limitations and photon noise are significant at this level (Nakajima 2006; Guyon 2005). The potential benefits in using higher-order BLMs

[4] The JWST however will provide a unique and stable platform for coronagraphy in the $3-5\,\mu$m band from space (Green et al. 2005).

from the ground are thus restricted to guarding against low-order aberrations introduced downstream from the AO system, but at the expense of contrast, throughput, and angular resolution.

### 4.3.3 Tip/Tilt and Low-order Aberrations

Thus far we have neglected quasi-static phase errors, or, at least, have assumed that the resulting scattered light has been judiciously removed with speckle-nulling hardware.[5] In this section we take a closer look at the issue. To get a feel for the problem, we calculate the contrast degradation due to just one error, systematic misalignment, at several characteristic levels of AO correction. Then we combine the results with theoretical low-order phase aberration information gathered from other studies and discuss the implications. This analysis along with that laid out in the previous two sections provides important first-order guidelines for selecting coronagraphic image masks for extreme AO systems.

Image mask response to quasi-static aberrations impacts the dynamic range and duty-cycle efficiency of high-contrast observations. For instance, in the case of tip/tilt errors, on-sky tracking latency or telescope-to-instrument flexure may lead to misalignments that leak significant amounts of light. Clearly, the masks presented here have different levels of resistance to such errors.

To assess pointing sensitivities, systematic tilt phase aberrations were added to the wavefront at the AO-coronagraph (IDL-MATLAB) interface. Optimum Lyot stop sizes were used for each mask, and median, instead of mean, intensities were evaluated to prevent bias towards poor contrast. The $1\,\lambda/D$ annulus directly outside the coronagraph

[5] Actually the light must go somewhere in order to conserve energy. It is sometimes preferable to simply place it on the other side of the image plane during a given integration.

IWA remained centered on the star as it was methodically shifted relative to the mask. Results are shown in Fig. 4-6 for linear alignment errors up to $5\,\lambda/D$.

At relatively low Strehl ratios ($\lesssim$ 88%), hard-edge masks perform comparably with apodized masks provided that the pointing error does not exceed $\sim 2\ \lambda/D$. At higher levels of correction ($\gtrsim$ 88%), mask alignment becomes more critical. In this regime, apodized masks are capable of generating significantly deeper contrast than the hard-edge mask. In particular, the Gaussian and 4th-order BLMs provide optimum contrast when aligned to better than $\sim 1\,\lambda/D$ at $\sim$ 88% Strehl and $\sim 0.5\,\lambda/D$ at $\sim$ 94% Strehl. If such accuracy is difficult to manage, higher-order BLMs may be chosen over the Gaussian and 4th-order BLM, with the usual tradeoffs (§4.3.2).

This analysis is also applicable to low-order aberrations in a more general sense. Shaklan & Green (2005) have shown that the 'order' of the mask (4th, 8th, 12th, ... etc.) uniquely determines a coronagraph's sensitivity to aberrations (tip/tilt, focus, astigmatism, coma, trefoil, spherical, ... etc.). The result is that higher-order masks, which are intrinsically broader, are naturally better filters of any given low-spatial-frequency phase error. For example, expansion of Equ. 4–2 shows that the Gaussian mask intensity transmission profile near the optical axis depends on $r$ raised to the fourth power; thus, it is a 4th-order mask (Fig. 5-1). Figure 4-6 confirms that the Gaussian mask follows the 4th-order BLM tilt sensitivity curve, and that higher-order BLMs follow suit.

The hard-edge mask may be considered in the limit as the exponent of the intensity transmission approaches infinity. It is effectively a mask of infinite order, and thus the most resistant to low-spatial-frequency aberration content. The sharp boundaries of the hard-edge mask however also make the coronagraph leak the most starlight. Combining this information, we recognize that Fig. 4-6 is qualitatively illustrative of a trend applicable to all individual phase aberrations, and sums of (orthogonal) phase aberrations, introduced downstream from the AO DM and wavefront sensor. As the phase

errors increase, the contrast generated by apodized masks will rise (degrade) from the AO noise floor and eventually intersect the hard-edge mask curve.

In general, quasi-static phase errors further reduce the Strehl ratio. Therefore the situation is slightly more complicated than with tip/tilt alone, which, strictly speaking, is a change to the pointing vector and not an aberration. Nevertheless, we can extend the principle to quantitatively include them all.

Consider the final measured Strehl ratio, $S$, written as a decomposition of uncorrelated errors (Sandler et al. 1994):

$$S = S_1 \, S_2 \, S_3 \, ... \, S_n, \tag{4–7}$$

where each $S_i$ with $1 \leq i \leq n$ represents an independent Strehl degradation. An equivalent statement is that uncorrelated wavefront errors add in quadrature. Since the Strehl ratio produced by the AO system is unrelated to the subsequent optical path, we let $S = S_{AO} \, S_{qs}$ describe the final stellar image, where $S_{AO}$ is the AO-corrected Strehl ratio (as has been used throughout the text and figures) and $S_{qs}$ is the Strehl ratio due to *all* quasi-static phase aberrations introduced downstream from the AO DM and wavefront sensor.

Results from §4.3.1 and Fig. 4-6 show that use of an apodized mask, preferably the 4th-order BLM (§4.3.2), is justified only when $S_{AO} \gtrsim 88\%$. Thus, we require that the measured Strehl ratio satisfy the condition:

$$S \gtrsim 0.88 \, S_{qs}, \tag{4–8}$$

where $0 \leq S_{qs} \leq 1$ is the intrinsic Strehl of the optical system. With an internal fiber-coupled source, such as a calibration lamp, $S_{qs}$ can be measured when the AO DM is inactive and flat, so far as one might trust zeroing the actuator voltages. We note that this relationship is valid only in the high-Strehl regime ($\sigma \lesssim \lambda/2\pi$).

The effects of speckle-nulling can be incorporated by noticing that contrast curves such as those shown in Fig. 4-6, and similar graphs for the other phase errors present in a

real system, will be "flattened" by the additional DMs (see §3). In other words, the extra degrees of freedom afforded with this hardware compensate for quasi-static aberrations whose spatial-frequencies match the intended search area. Long-lived speckles may be nulled to an intensity level where the contrast curves in Fig. 4-6 intersect the vertical axes; this is true for any such aberration. A candidate companion would then be noticed by the inability of the instrument to remove its mutually incoherent signal. Subsequent changes to the shape of the DMs and hence location of the dark hole might indicate the presence of other faint sources.

As an example, consider a measured Strehl ratio $S = 85\%$ with a system that has an intrinsic Strehl ratio $S_{qs} = 94\%$. According to Equ. 4–8, we are indeed justified in using the 4th-order BLM for this application. However, if the additional DMs cannot remove quasi-static speckles from the region of interest down to the intensity of the AO-limited noise floor, we may consider switching to a higher-order mask, such as the 8th-order or 12th-order BLM, to help filter stellar residuals before they illuminate the detector.

These results allow us to make rather strong conclusions regarding the implementation guidelines for image masks included in this study. We state them concisely in the next section. For further discussion of low-order phase aberrations within the context of Lyot coronagraphy, see §5 and Crepp et al. (2006), Sivaramakrishnan et al. (2005), Lloyd & Sivaramakrishnan (2005), Shaklan & Green (2005).

### 4.4 Conclusions

One should select an image mask whose rejection of starlight is commensurate with the noise floor set by the AO system. Our numerical simulations imply the following:

(1) Apodized masks should replace the hard-edge mask only when on-sky Strehl ratios, $S$, exceed $\sim 0.88\ S_{qs}$, where $S_{qs}$ is the Strehl ratio due to all quasi-static phase aberrations introduced by the instrument downstream from the AO system – e.g., non-common-path errors. Below this level of correction, the hard-edge mask outperforms apodized masks, not by reaching deeper levels of contrast, but by generating similar

contrast (§4.3.1) and throughput (§4.3.2) with more resistance to quasi-static errors. This result is independent of entrance aperture geometry and bandpass.

(2) Since 4th-order BLMs yield more Lyot stop throughput than the Gaussian mask, and apodized masks with smooth intensity transmission gradients are equally difficult to manufacture, Gaussian masks should not be implemented under any foreseeable conditions on telescopes with uniform transmission entrance apertures.

(3) The selection of higher-order BLMs over the 4th-order BLM is relegated to situations where both the ability to correct for the atmosphere to a very high degree and the *in*ability to adequately null quasi-static speckles is simultaneously present.

For the operating range often considered with a traditional Lyot coronagraph, IWA $= 3-5\ \lambda_{max}/D$, the exact contrast and throughput values will deviate from those reported in §4.3, but in a rather predictable manner. The italicized conclusions however do not change with these considerations. It is also important to mention that Strehl ratios can be somewhat pesky to calculate in practice. Experimentally determined values are accurate only to several percent if the image is not spatially sampled at a rate higher than twice the Nyquist frequency (Roberts et al. 2004).

The hard-edge occulting mask is a remarkably relevant coronagraphic tool in an age of sophisticated wavefront correction techniques and clever applications of Fourier optics. Apodized masks, or binary versions of apodized masks (Kuchner & Spergel 2003), require nano-fabrication capabilities at visible and near-IR wavelengths (Balasubramanian et al. 2006; Crepp et al. 2006; Carson et al. 2005; Debes et al. 2004; Trauger et al. 2004); this can be a strong deterrent and should be avoided unless Equ. 4–8 is satisfied (although, in a fast optical system, the focal ratio may impose stringent tolerances when building a hard-edge mask as well). In the realm of extreme AO, the 4th-order BL mask should be implemented, so long as quasi-static phase aberrations are manageable with speckle-nulling hardware.

Finally, our calculations suggest that the wavefront correction levels required for ground-based observations preclude reliable spectroscopic measurements of close-separation companions that are more than approximately one million times dimmer than their host star without use of an integral-field spectrograph. Presumably, space-based instruments will be able to do much better. Nevertheless, this result is still more than an order of magnitude deeper than current AO-coronagraphs provide.

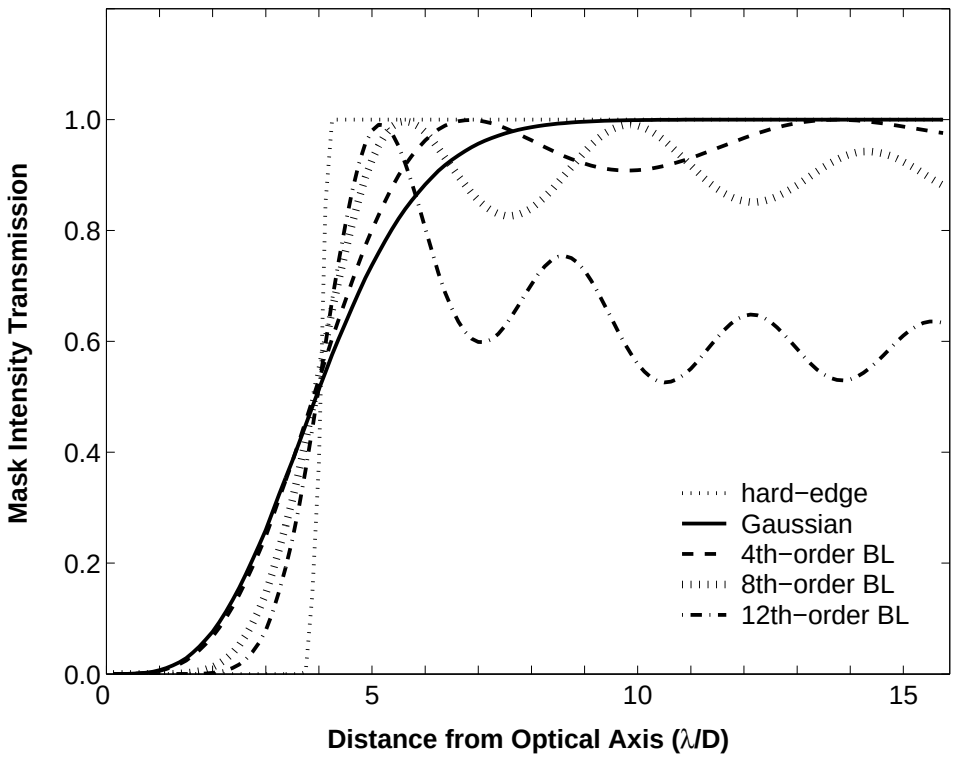


Figure 4-1. Intensity transmission profiles for each radial image mask. The IWA $= 4\ \lambda/D$. Band-limited masks (BLMs) have extended off-axis attenuation, which allows them to be composed of a finite range of low spatial-frequencies. This feature offers unlimited dynamic range as the Strehl ratio approaches 100%. A Lyot-style coronagraph equipped with a BLM is one of the leading candidate designs for the Terrestrial Planet Finder Coronagraph (*TPF-C*) space mission (Ford et al. 2006).

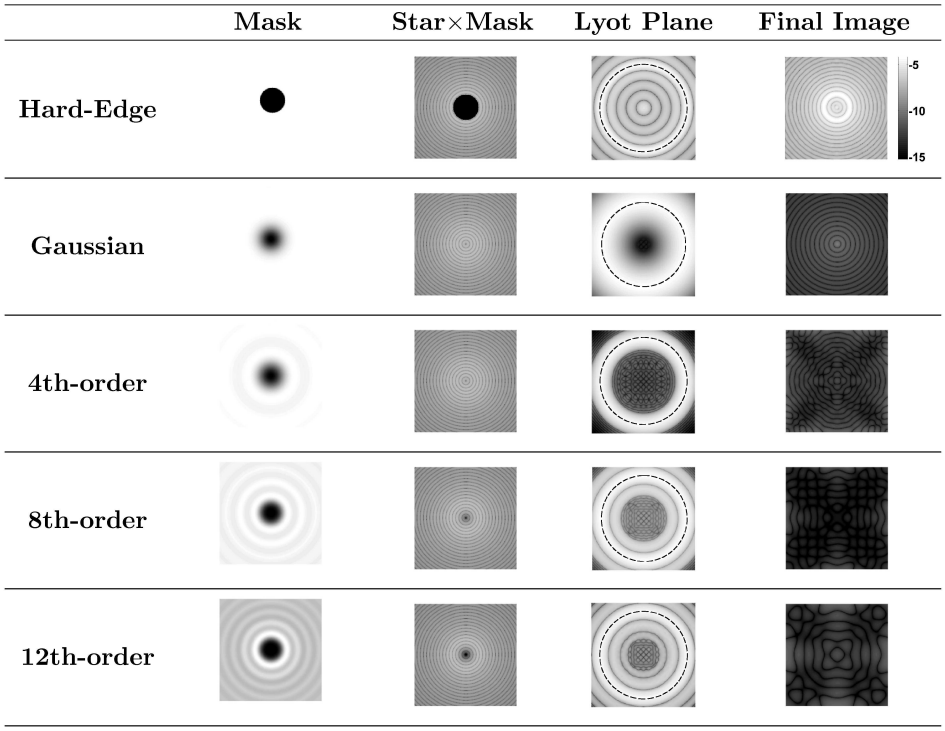


Figure 4-2. Coronagraph simulations with perfect incident wavefronts. Intensities in the first two columns are shown on the same logarithmic scale using the mask profiles, $0 \leq |M(r)|^2 \leq 1$, in Fig. 1 and a normalized Airy pattern. The spatial extent of the image planes are identical and can be estimated from knowing that the hard-edge mask has a diameter of 8 $\lambda/D$. A dashed line in the 'Lyot Plane' column indicates the outline of the circular unobstructed entrance aperture. An ∼60% throughput Lyot stop was used for the hard-edge, Gaussian, and 4th-order BLMs. The 8th-order and 12th-order BLMs offer better rejection of low-order aberrations at a cost of throughput and angular resolution. The 'Final Image' column shows the contrast generated by each mask using the logarithmic scale in the hard-edge mask row; BLMs remove on-axis starlight down to the numerical noise level of the simulations ($< 10^{-12}$).

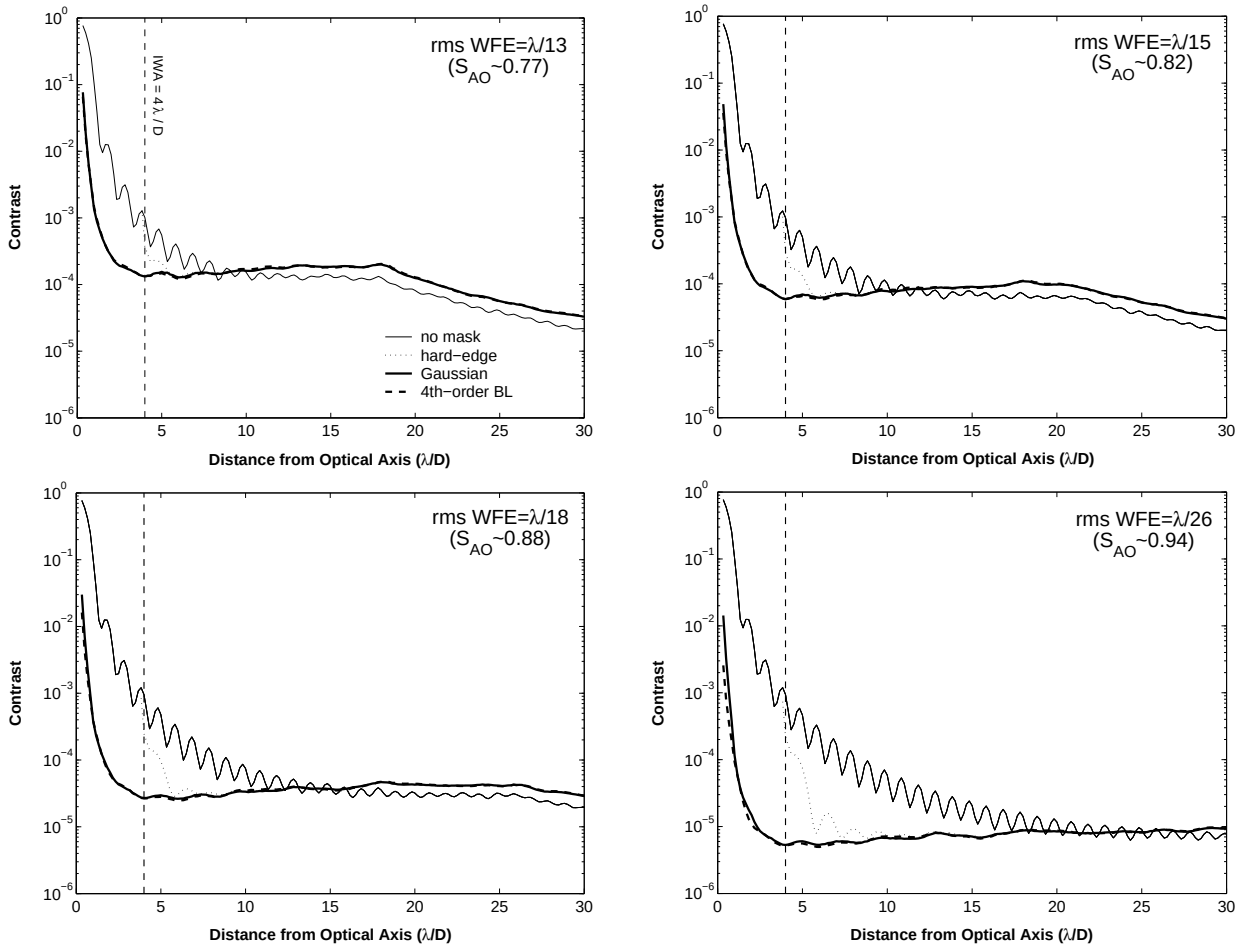


Figure 4-3. Azimuthally averaged contrast curves for the hard-edge, Gaussian, and 4th-order BLM's using a fixed circular Lyot stop size with ∼60% throughput. The Lyot stop for the Airy pattern has 100% throughput.

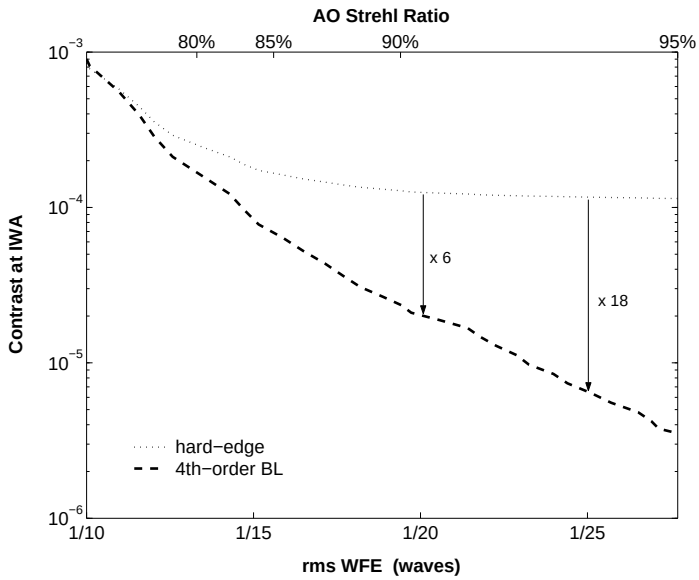


Figure 4-4. Average contrast within the $1\,\lambda/D$ wide annulus directly outside of the coronagraph IWA as a continuous function of atmospheric wavefront correction and the relative gain (shown by arrows) achieved by switching to the 4th-order BLM. The hard-edge mask's performance is limited by starlight diffracted into the interior of the $\sim 60\%$ throughput Lyot stop. This prevents significant improvements beyond $\sim 88\%$ Strehl.

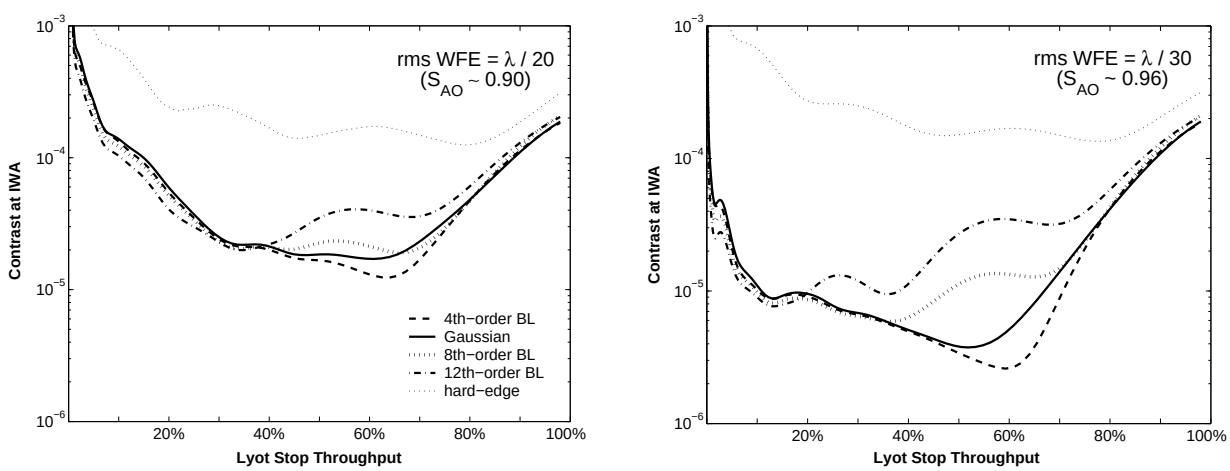


Figure 4-5. Average contrast within the $1\,\lambda/D$ wide annulus directly outside the coronagraph IWA as a function of Lyot stop throughput for $\sim 90\%$ Strehl (left) and $\sim 96\%$ Strehl (right).

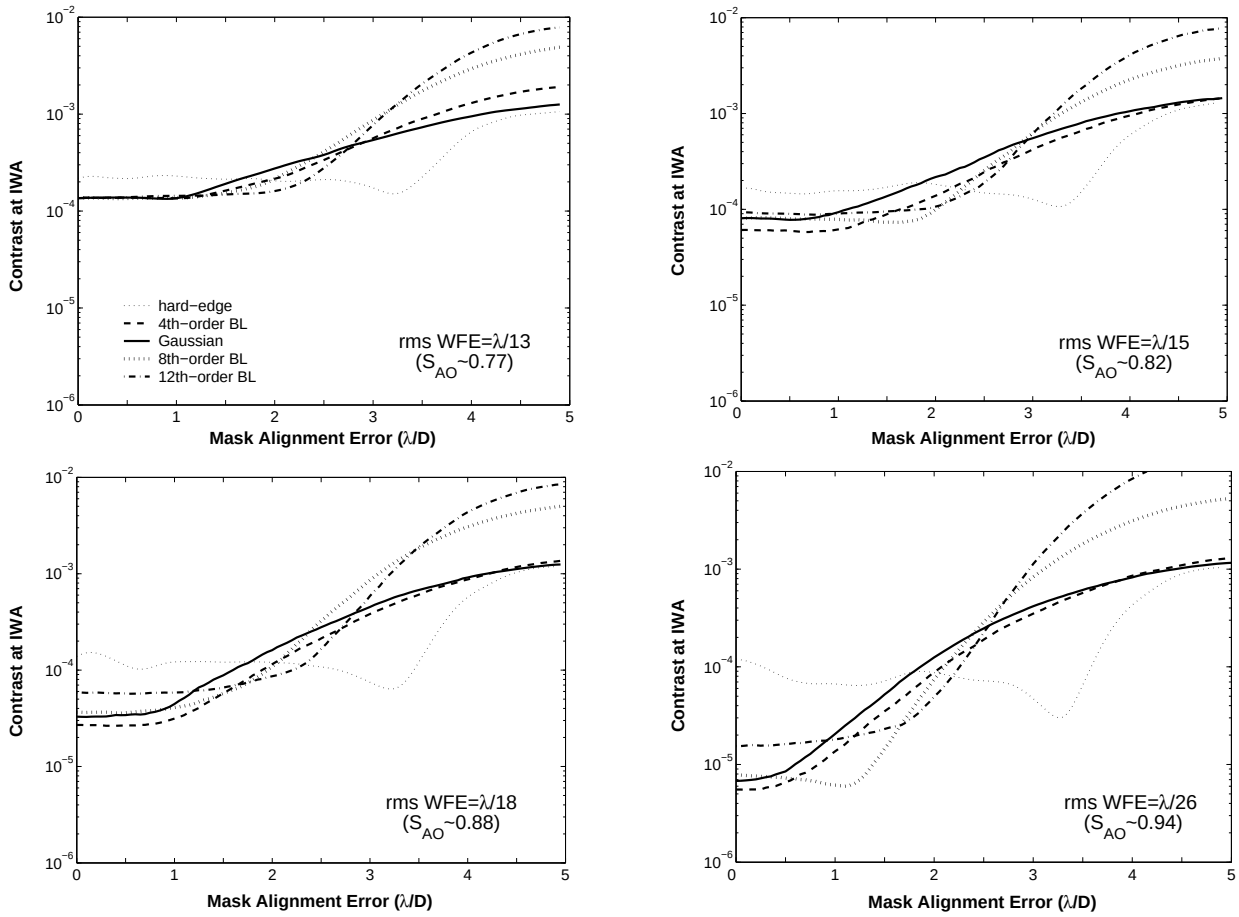


Figure 4-6. Median contrast within the $1\,\lambda/D$ annulus outside the coronagraph IWA as a function of systematic tilt error for several characteristic levels of wavefront correction using optimal Lyot stop sizes. Note that the Gaussian mask is a 4th-order mask. The non-monotonic changes in contrast are a result of calculating the median intensity with alignment errors in a circular geometry and phasing between the Airy pattern and the mask intensity transmission (see Lloyd & Sivaramakrishnan 2005).

# CHAPTER 5
# LABORATORY TESTS

We have built a series of notch filter image masks that make the Lyot coronagraph less susceptible to low-spatial-frequency optical aberrations. In this chapter, we present experimental results of their performance in the lab using monochromatic light. Our tests show that these eighth-order masks (§2) are resistant to tilt and focus alignment errors, and can generate contrast levels of $2 \times 10^{-6}$ at 3 $\lambda/D$ and $6 \times 10^{-7}$ at 10 $\lambda/D$ without wavefront correction. This work supports recent theoretical studies suggesting that eighth-order masks can provide the TPF-C with a large search area, high off-axis throughput, practical requisite pointing accuracy, and resistance to stellar size.

## 5.1 Mask Design and Fabrication

We have manufactured four binary notch filter image masks using *e*-beam lithography: one fourth-order mask and three eighth-order masks. These masks represent a second generation of technology development, where we have improved upon the prototype mask presented in Debes et al. (2004). In the following, we briefly describe our design strategy and nanofabrication techniques.

The base structure used to mechanically support the opaque portions of the masks is a 0.7 mm thick piece of Boroaluminosilicate glass with a scratch/dig of 20/10. A 270 nm thick layer of Chromium serves as the on-axis occulting material, and was deposited onto one side of the glass using a Semicore *e*-gun evaporator. Small structures were then dry-etched from the Chrome layer with an applied materials cluster tool using a high density decoupled plasma composed of Argon, Chlorine, and Oxygen. No anti-reflection coating was applied. Figure 5-1 shows a photo of the substrate containing all of the designs.

Each mask is designed for an $f/163$ or slower beam with a 40 nm bandwidth centered on the $\lambda = 632.8$ nm HeNe laser source. The focal ratio of the system is large to facilitate the fabrication of small features in the masks. The physical size or extent of the masks are

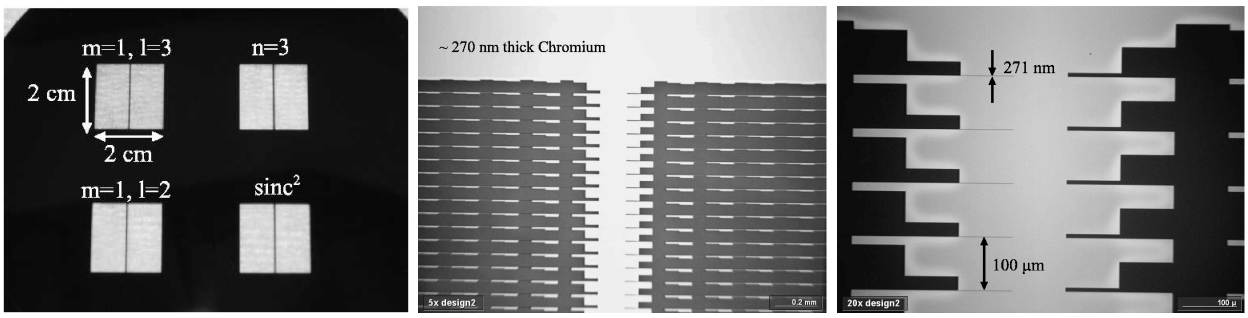


Figure 5-1. The four linear binary notch filer image masks (left), and optical microscope false color images of the $m = 1$, $l = 2$ eighth-order mask at 5x magnification (middle) and 20x magnification (right). The dark areas in the microscope images are transparent; this is where the Chrome has been etched away. The spacing between stripes and the spacing between samples is $\lambda_{min}\, f/\# = 100\, \mu m$.

2 cm to a side. Although truncation sets an outer-working-angle and degrades contrast, notch filter masks can easily be manufactured large enough to ensure that these effects do not place significant constraints on the search area and are not the dominant source of error. Notch filter masks can be designed to have an azimuthally symmetric search area; however, we have chosen to make linear masks so that the effective opacity changes in only one direction. This property simplified the testing of their response to pointing errors. The FWHM of the image masks (i.e. 2× IWA) were designed to be roughly equivalent such that fair comparisons of their performance could be made (Table 5-1). Aime (2005) suggests that the mask equivalent-width serves as a better proxy for making such comparisons; the authors note that the FWHM value differs from the equivalent-width value by $\lesssim 1\%$ for each of the individual masks presented here.

Linear binary masks consist of vertically repeating parallel stripes, where band-limited or notch filter functions describe the curves in each stripe (Kuchner & Spergel 2003). We have made binary masks using the notch filter functions, because sampling makes the intricate features near the optical axis a part of the design, and not the result of the finite resolution of the lithography machine. In general, the sampling is not symmetric

(Fig. 5-1). The low-frequency amplitude transmission of the eighth-order masks follow Equations 2–6 and 2–7.

The smallest features in a mask are often found near the optical axis. Their size depends upon both the IWA and bandwidth, among other parameters. Generally, as the IWA improves (i.e. gets smaller), the size of the smallest features in the mask increases, and as the bandwidth widens, the size of the smallest features decreases. If the IWA is too large or the bandwidth too wide, the smallest features may be too small to build.

An additional constraint is that the minimum feature sizes should not be smaller than the thickness of the opaque material. This helps to minimize the waveguide effects associated with binary masks, and other vector electromagnetic effects that can degrade contrast, especially with broadband light. Lay et al. (2005) describe some of these potential limiting factors for the TPF-C mission, and suggest several alternatives for compensation; one of which includes dramatically increasing the focal ratio at the mask ($> f/60$), as was done in this experiment. This design strategy was also implemented in the Debes et al. (2004) experiment for similar reasons.

Minimum feature size requirements - both practical and theoretical - limited our ability to make eighth-order masks with high Lyot stop throughput. In theory, eighth-order masks can achieve $\sim 60\%$ Lyot stop throughput with IWAs of $\sim 4\,\lambda_{max}/D$. Our masks were *designed* however to achieve only $\sim 20\%$ throughput at most, because we were restricted to making features larger than the thickness of the Chrome; the smallest feature size in each of the eighth-order masks is $\sim 270$ nm, whereas the smallest feature size in the fourth-order mask is 7119 nm. To increase the throughput, we would have to increase the $f/\#$, decrease the bandwidth, or decrease the thickness of the Chrome. Clearly the focal ratio is already large and the bandwidth is already narrow. Also, we show in §5.3 that increasing the thickness of the Chrome is the most notable improvement we have made upon the mask presented in Debes et al. 2004. Thus, future mask development will necessarily involve using a material that is intrinsically more

opaque at visible wavelengths, such as Aluminum (Semaltianos 2001; Lay et al. 2005). This will enable the fabrication of masks that have more opacity and smaller minimum features sizes.

The equations describing the exact structure of linear, binary, sampled eighth-order notch filter image masks are derived in KCG05 . Table 5-1 displays the relevant quantities for our designs, using the same notation (except in KCG05 $f/\# = f$). For each mask, sampling began at a horizontal distance of $x = \zeta_0 \, \lambda_{min} \, f/\#$ from the optical axis.

Table 5-1. Mask design parameters for a bandpass of $632.8 \pm 20$ nm. For an elliptical or circular primary mirror, the Lyot stop throughput of a linear mask is given by: $T = 1 - \frac{2}{\pi}[\epsilon\sqrt{1-\epsilon^2} + \arcsin(\epsilon)]$, where $0 \leq \epsilon \leq 1$ is a dimensionless parameter that controls the width of the zones of diffracted starlight at the edges of the Lyot stop. We were able to achieve $\sim 75\%$ of the maximum theoretical Lyot stop throughput for each mask in the experiment.

| Mask | $\text{sinc}^2$ | $n = 3$ | $m = 1,\, l = 2$ | $m = 1,\, l = 3$ |
|---|---|---|---|---|
| order | 4th | 8th | 8th | 8th |
| IWA/$(\lambda_{max}/D)$ | 2.350 | 2.372 | 2.332 | 2.356 |
| $\epsilon$ | 0.488 | 0.674 | 0.716 | 0.759 |
| $N$ | 1.01444077 | 0.99098830 | 1.93640370 | 1.47114548 |
| $\hat{M}_{0_A}$ | 0.01423518 | 0.07833984 | 0.05989364 | 0.06702707 |
| $\hat{M}_{0_B}$ | — | 0.01803281 | 0.03028228 | 0.02278117 |
| $C$ | — | -0.25123206 | -0.51959437 | -0.35644301 |
| $\zeta_0$ | 0.28800972 | 0.25875213 | 0.25877876 | 0.25874218 |
| Smallest Feature | 7119 nm | 271 nm | 270 nm | 270 nm |
| Theoretical Throughput | 40.4% | 21.2% | 17.4% | 13.7% |
| Experimental Throughput | 30.7% | 15.7% | 13.0% | 10.4% |

## 5.2 Experimental Setup

The design of the University of Florida coronagraphic testbed is that of a standard transmissive Lyot coronagraph without wavefront correction, as depicted in Figure 1-8, and similar to the setup described in Debes et al. (2004). "Starlight", generated by a $\lambda = 632.8$ nm HeNe laser for monochromatic testing, passes first through a set of neutral density (ND) filters and is then focused by a microscope objective lens into a $4\,\mu$m single-mode fiber for spatial filtering. The fiber exit-tip serves as a bright point source. This expanding beam, N.A. $= 0.12$, is collimated and then truncated by a circular $\sim 3$ mm

diameter iris, simulating the primary mirror of an off-axis telescope. Optics downstream from the iris are high quality achromat doublets capable of handling future broadband tests. The first achromat, $f = 500$ mm, focuses the light onto the substrate containing all of the notch filter image masks. The substrate is mounted onto a precision x-y-z stage for fine adjustments. The light is then re-collimated by an identical achromat. In the Lyot plane, an optimized Lyot stop blocks the light diffracted by the mask at the location of the reimaged entrance pupil. The Lyot stop size is adjustable and takes the shape of the intersection of two overlapping circles, since the masks are linear. The remaining light is then focused onto an SBIG ST-2000XM CCD detector where images are taken for analysis. The images are sampled approximately $10\times$ more frequently than the Nyquist frequency with $7.4\,\mu m$ pixels. The anolog-to-digital converter has a bit depth of 16, and the CCD has a factory quoted RMS read noise of 7.9 $e-$. These sources of noise are always at least two orders of magnitude smaller than the measured contrast values when used in concert with our experimental techniques, which are described in the following.

In order to measure contrast, we perform a comparison of images taken with and without the coronagraph in place. Due to the extreme contrast levels involved, we use a combination of the ND filters and the linearity of the CCD to calculate relative intensities and to generate high signal-to-noise ratio images in a reasonable amount of time. We first attenuate the laser light with the ND filters, which are placed upstream from the single-mode-fiber to ensure that their aberration effects are negated, and take an image of the star without the mask and without the Lyot stop in the optical train. Then, the mask and Lyot stop are inserted into place, and the ND filters are removed. In this final image, the intensity values at each pixel are divided by the average flux within the FWHM of the image of the star taken without the coronagraph, and normalized to the integration times and ND filters used. We define the resulting value, at each pixel, as the relative intensity. The contrast then is simply the relative intensity divided by the Lyot stop throughput and band-limited (i.e. low-frequency) part of the mask intensity transmission

at that position. Figure 5-2 shows images of the star at various steps in the procedure. We could have chosen a less conservative definition of contrast by instead normalizing to the interpolated peak intensity of the imaged source, rather than the average flux within the FWHM (Shaklan & Green 2005); however, these two values differ by less than a factor of two. It is not necessary to add and remove the Lyot stop in order to measure contrast, but we find that doing so facilitates calculation of the off-axis throughput.

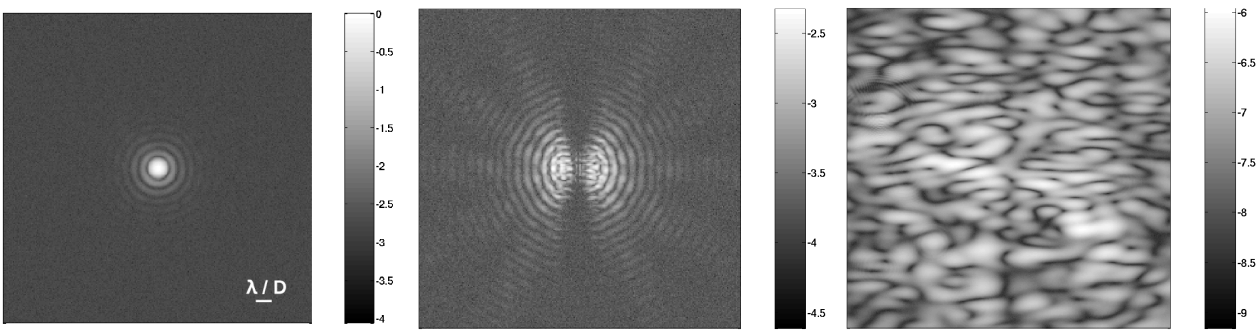


Figure 5-2. Laboratory images of the simulated star without the coronagraph (left), the $m = 1$, $l = 2$ mask aligned over the star (middle), and the star with both the mask and Lyot stop in place (right). Intensities are plotted on a logarithmic scale. The image of the star shows the angular size scale of the telescope. Speckles created by imperfections in the optics limit the dynamic range of the coronagraph creating a noise floor at the $\sim 10^{-7}$ level near the IWA. The contrast is calculated by dividing the relative intensity, shown in the image on the right and later in Fig. 5-3, by the Lyot stop throughput and mask intensity transmission; this accounts for the off-axis attenuation of the coronagraph.

Linear binary masks approximate band-limited masks only when the vertical angular size of the stripes in the mask are smaller than $\lambda_{min}/D$, the resolution of the telescope. To ensure that the masks diffract light appropriately, we increased the focal ratio of the system in the first image plane from the initial design of $f/\# = 163$ to $f/\# \approx 187$, by shrinking the size of the entrance aperture. This also resulted in an improvement of the masks' effective IWA by the same factor. The Lyot stop size was set conservatively to obtain $\sim 75\%$ of the maximum theoretical throughput, so that small mis-alignments did not result in diffracted light leakage through the center of the stop onto the detector.

Table 5-1 shows the designed IWAs before increasing the focal ratio, and the experimental Lyot stop throughput achieved.

## 5.3 Results

### 5.3.1 Chrome Transmission and Relative Intensities

The performance of the prototype mask presented in Debes et al. (2004) was limited by the transmission of light directly through the Chromium occulting layer. In this study, we have increased the thickness of this layer from 105 nm to 270 nm. Using the transmission curve in Debes et al. 2004, we calculate that the peak transmission should improve from $7.5 \times 10^{-4}$ to $9.2 \times 10^{-9}$. We measure a peak transmission of $2.3 \times 10^{-8}$. This is slightly worse than predicted, but opaque enough for this application nevertheless (Fig. 5-3). The discrepency in these values can be understood by considering inhomogenieties in the thickness of the Chromium layers. A $< 5$ nm deviation in each makes up the difference. The contribution of transmission directly through the Chromium to the limiting contrast in this experiment is approximately one order of magnitude smaller than the scattered light floor near the IWA, and less so in the regions where the masks have little off-axis attenuation. A more demanding application, such as the TPF-C, would, of course, require a material with a higher opacity.

Figure 5-3 also shows a difference in the amount of light transmitted near the optical axis, $r \lesssim \lambda/D$, between the fourth-order mask and the eighth-order masks. This is evidence that the eighth-order masks are blocking more scattered light, simply because they are wider, and reducing the effects of low-order aberrations (we test this latter claim more carefully in §5.3.3). These properties are not seen as clearly in contrast curves, where, interior to the IWA, the intensity transmission of the mask controls the detection threshold.

### 5.3.2 Contrast Measurements

We find that the coronagraph's performance is limited by quasi-static scattered light. The image plane speckles seen in Figure 5-2 are the result of wavefront distortions, created

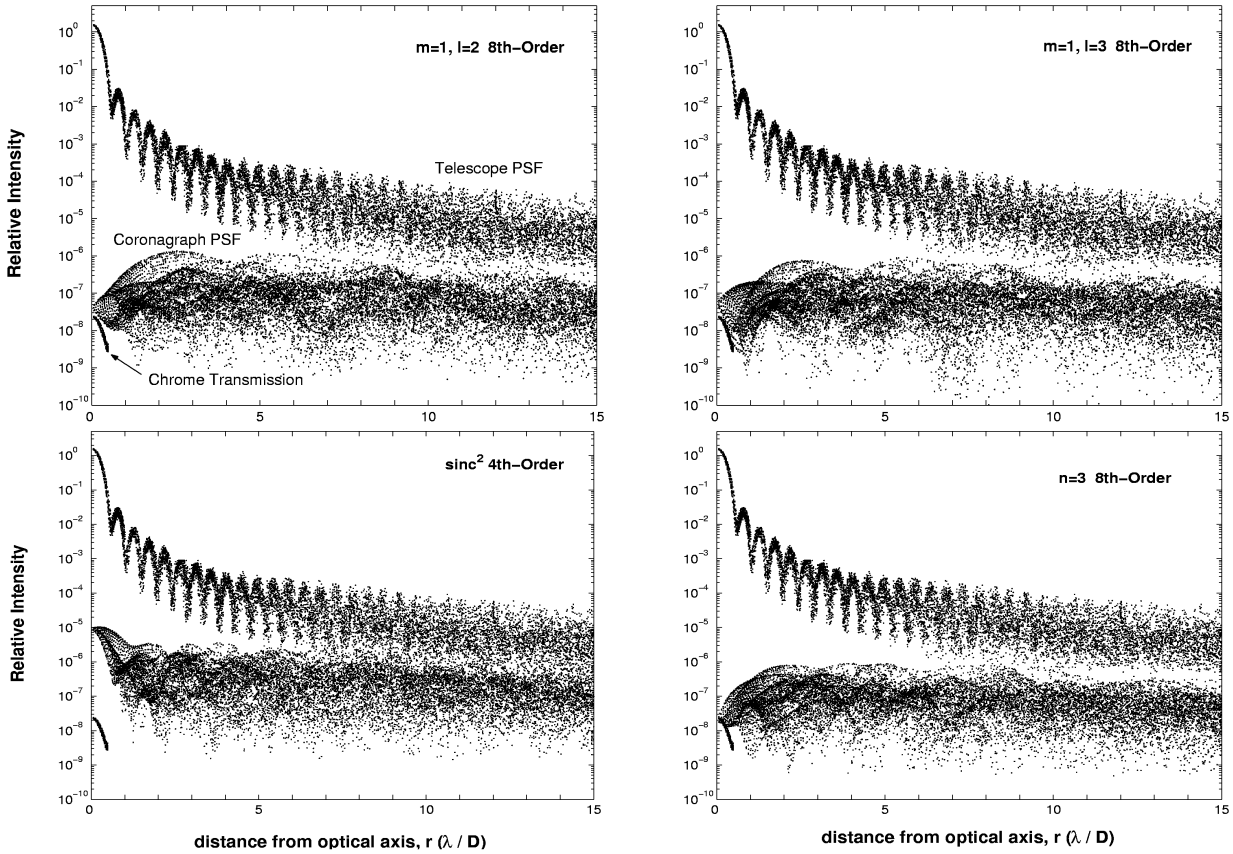


Figure 5-3. Telescope PSF, coronagraph PSF, and Chrome transmission for each mask using a circular entrance aperture. The Chrome transmission was measured at the center of the substrate. Inside the IWA, the eighth-order masks block more scattered light and reduce the effects of low-order aberrations. The thickness of the Chromium does not limit the performance of the coronagraph, but does transmit a non-negligible amount of light which contributes to the noise floor. Contrast is calculated by dividing the coronagraph PSF by the intensity transmission of the mask and the Lyot stop throughput.

by imperfections in the optics. In practice, speckles can mimic and often overwhelm the light of dim companions (§1.2.3,3, 4).

We calculated contrast for pixels within a $10\,\lambda/D \times 30\,\lambda/D$ section across the center of the PSF by dividing the relative intensities by the Lyot stop throughput and band-limited part of the mask intensity transmission, $|\hat{M}(x)|^2$, at each position, $x$, the horizontal distance of pixels from the optical axis. That way, the direction in which the halo of speckles decreased in flux coincided with the direction of opacity change in the masks. We were able to achieve $2 \times 10^{-6}$ contrast at $3\,\lambda/D$ and $6 \times 10^{-7}$ contrast at $10\,\lambda/D$, as quoted

in the abstract. In Figure 5-4, we plot the corresponding $3\,\sigma$ detection limits, where $\sigma$ is defined as the standard deviation of the scattered light noise floor at a given location in the final image plane. The eighth-order masks reduce the amount of scattered light close to the optical axis, and slightly out-perform the fourth-order mask near the IWA as a result of their more steeply increasing intensity transmission in that region. The contrasts in the rest of the search area are essentially identical.

To calculate the Strehl ratio of our system, we compared a model of the Airy pattern incident onto the mask with experimental data. We find that the Strehl ratio exceeds 98%. Combining this with the fact that the coronagraph is speckle dominated and the optical quality of our achromats are high (see §5.3.3), we conclude that the detection limits shown in Figure 5-4 represent the approximate deepest contrast that is achievable from the ground with current AO systems, using this type of coronagraph.

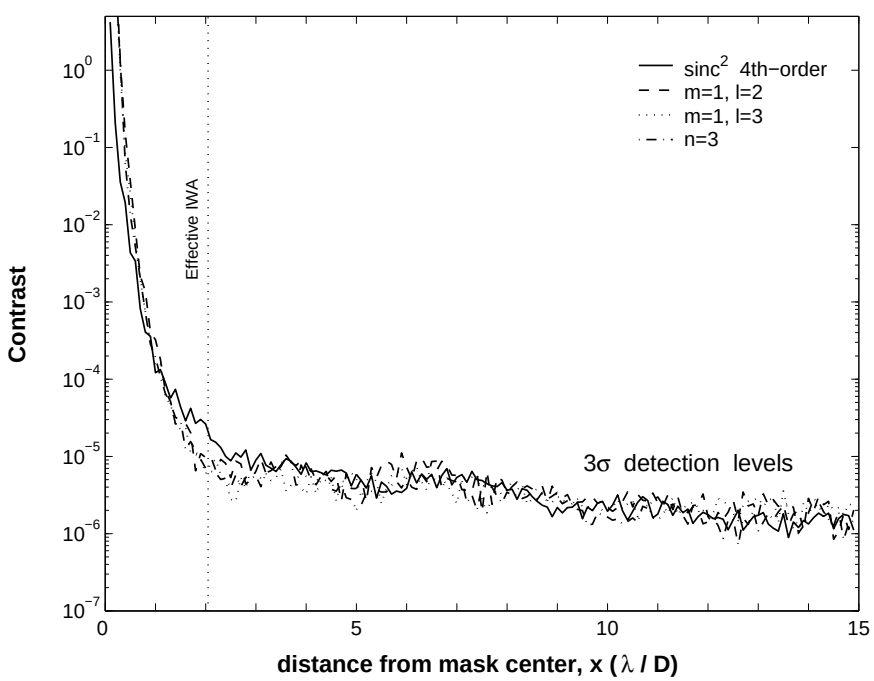


Figure 5-4. Experimental $3\,\sigma$ detection limits for each mask. The effective IWAs were calculated taking into consideration the change in focal ratio from the initial mask designs.

### 5.3.3 Tip/Tilt and Focus Sensitivity

We tested the tilt and focus aberration sensitivities of each mask by introducing small alignment errors to the substrate in the image plane. The results are shown in Figure 5-5, where we plot the contrast at $3\,\lambda/D$ as a function of the distance that the masks were displaced. The scattered light floor limits the dynamic range of the coronagraph at small aberration levels; in this regime, the masks generate contrasts to within a factor of two of one another, as shown in the previous section (Fig. 5-4). At large aberration levels, where diffracted light dictates the contrast, there is a clear dichotomy in the masks' behavior.

To measure the tilt aberration sensitivity of each mask, we moved the substrate laterally across the center of the image of the star in 5 $\mu$m increments. We find that the eighth-order masks are easier to point than the fourth-order mask. To quantify this statement, we calculated the width of the pointing "sweet-spot" for each mask, where the contrast at $3\,\lambda/D$ is flat to within $2\,\sigma$ and limited by scattered light. The mean width of this zone for the eighth-order masks is $1.06 \pm 0.03\,\lambda/D$; the width of this zone for the fourth-order mask is $0.20 \pm 0.05\,\lambda/D$, a factor of $\sim$ 5 smaller. With an 8 m telescope operating at $\lambda = 0.5\,\mu m$, these tolerances correspond to pointing accuracies of 6.8 mas and 1.3 mas respectively. (Lloyd & Sivaramakrishnan (2005) discuss tip/tilt errors in Lyot coronagraphs in detail. For a practical application, see the description of the AEOS coronagraph by Lloyd et al. (2001).)

To measure the focus aberration sensitivity of each mask, we moved the substrate along the optical axis in logarithmic increments of 0.18 dex. With a similar analysis, we find that the eighth-order masks are also less susceptible than the fourth-order mask to focal misalignments. The eighth-order masks provide the same contrast as the fourth-order mask in a system with $\sim$ 4 times as large an RMS wavefront error.

These results (Fig. 5-5) depend upon the amount of scattered light present in the system. If the scattered light levels were reduced, it would be possible to measure the response of the masks to smaller aberrations; the width of the tilt and focus sweet-spots

would decrease as the contrast improves, and the relaxation ratios would change. KCG05 estimate that eighth-order masks should relax pointing requirements relative to fourth-order masks by a factor of $\sim$ 6 in a system with no scattered light designed to achieve $10^{-10}$ contrast at $3\,\lambda/D$. SG05 have performed more careful calculations and predict an even larger relaxation ratio of 16 in the allowable tilt RMS wavefront deviation, when comparing eighth-order masks to fourth-order masks in an ideal system designed to achieve $10^{-12}$ contrast at $4\,\lambda/D$.

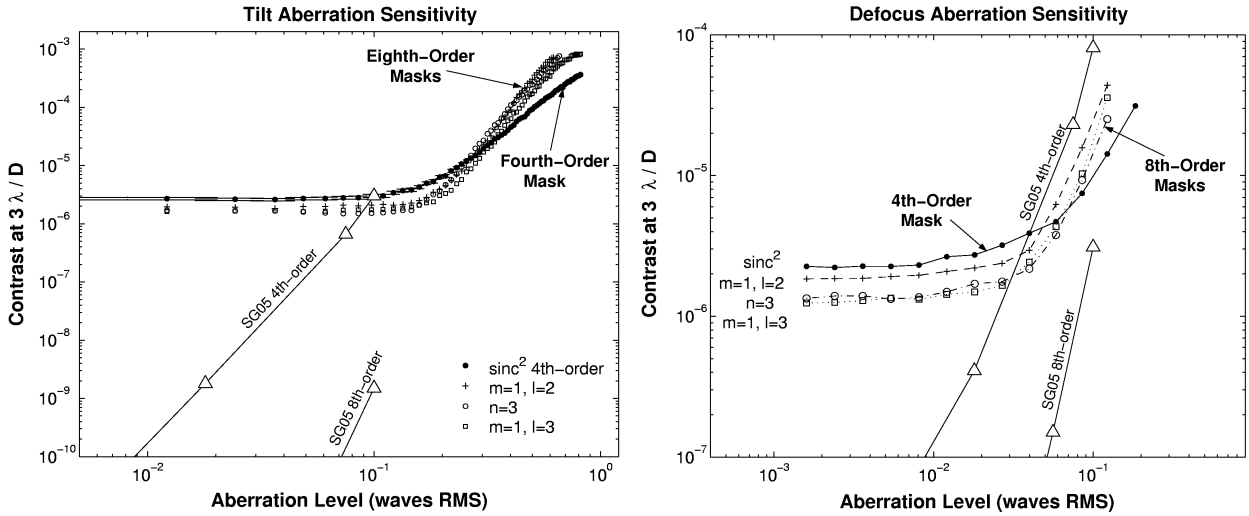


Figure 5-5. Coronagraph sensitivities to tilt (left) and focus (right) aberrations for each mask. The theoretical predictions of Shaklan & Green (2005) are over-plotted for comparison (see text). Scattered light prevented measurement of the diffracted light response of the masks at small aberration levels. Uncertainties in the measurements for the fourth-order mask are shown in the tilt graph; the errorbars are on the order of the size of the datapoints and representative for all of the experimental curves shown in both graphs. The focal ratio of our system was large enough to warrant tilt realignment for each focus datapoint, but not focus realignment for each tilt datapoint; this motivated the linear versus logarithmic measurement increments used for acquiring data.

For comparison, the SG05 theoretical tilt and focus curves are over-plotted in Fig. 5-5 (the triangular data points); these represent the steepest possible slopes that can be achieved in practice, since the model accounts only for diffraction. The general location of our experimental data are in good agreement with theory, and, to first order, simply adding a constant level of scattered light to the Shaklan & Green (2005) diffracted light

curves recovers the eighth-order masks' experimental contrast to within the uncertainty of the measurements. The fourth-order mask however makes exception, by providing better contrast in practice than expected from theory. This apparent discrepancy is resolved by considering a subtle difference between the two studies: the Lyot stop size;[1] the SG05 simulations maximize off-axis throughput by choosing the largest possible Lyot stop shape, whereas we have undersized the Lyot stop in this experiment by $\sim 25\%$ for each mask. In the presence of aberrations, the contrast of a band-limited mask depends upon the size of the Lyot stop. If the light diffracted in the Lyot plane due to aberrations is non-uniform and less intense near the optical axis, decreasing the size of the Lyot stop can improve contrast, at a cost of throughput and resolution (Sivaramakrishnan et al. 2005, see). We find that the introduction of tilt and focus aberrations produces patterns in the Lyot plane that fit this description (Fig. 5-6), and that the undersizing of the Lyot stop is responsible for an enhanced resistance to aberrations. Furthermore, this effect is more pronounced with the fourth-order mask than the eighth-order mask, since low-order aberrations can be partially or completely filtered in the image plane before reaching the Lyot pupil.

It is a good assumption that the fourth- and eighth-order mask phase aberration contrast curves (Fig. 5-5) do not intersect at more than one point for a given aberration: the slope of a mask's dependence on *any* low-order Zernike mode is always at least as steep for eighth-order masks as it is for fourth-order masks (Shaklan & Green 2005). Since we see the intersection in both graphs in Fig. 5-5, we conclude that the eighth-order masks can achieve better contrast than the fourth-order mask when small levels of tilt and focus aberrations are present, even though this regime was not available for direct measurement in our experiment. At intermediate aberration levels, we do indeed see an improvement

[1] Other differences between this study and Shaklan & Green (2005) are: (1) we used a circular entrance aperture, instead of an elliptical entrance aperture, and (2) the contrast was measured at $3\,\lambda/D$, instead of $4\,\lambda/D$.

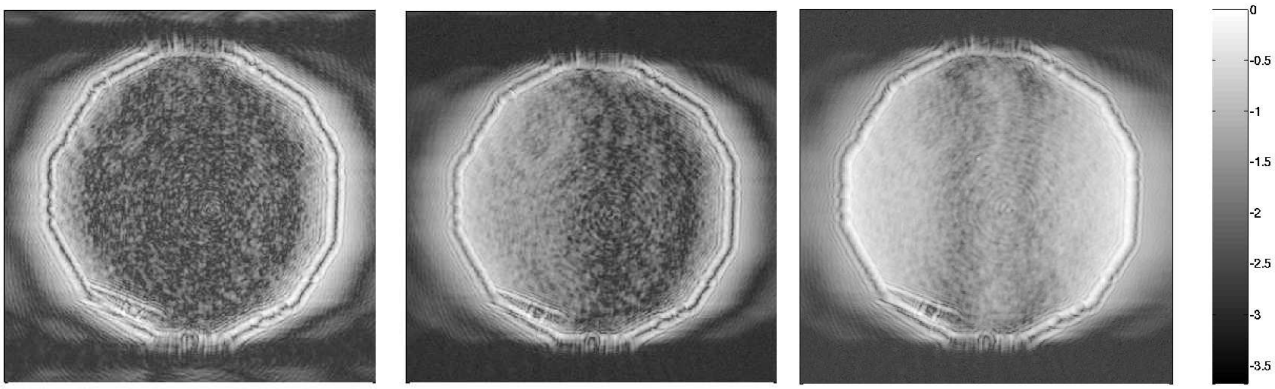


Figure 5-6. Characteristic Lyot plane images with optimum mask alignment (left), and $2 \times 10^{-1}$ waves RMS tilt aberration (middle), and $9 \times 10^{-2}$ waves RMS focus aberration (right) using the $m = 1$, $l = 2$ mask. Intensities are normalized to the peak intensity of the focus image and are on a logarithmic scale. Shrinking the Lyot stop can improve contrast when certain aberrations are present, as is the case here. These images can be compared to the analytic predictions in Fig. 3 of Sivaramakrishnan et al. (2005). Evidently, small amplitude tilt and focus phase aberrations produce a uniform leakage of light into the Lyot pupil interior. Although the aberrations presented here are rather large, aspects of both images appear to reflect this phenomena. More complicated processes such as cross-talk between induced and inherent aberrations as well as frequency-folding from mask construction errors also contribute to the Lyot pupil field, and can create an intensity gradient.

in contrast with the eighth-order masks. This is more evident with tilt, because the intersection between experimental curves occurs well above the scattered light floor.

Reducing the amount of scattered light in the coronagraph by approximately two orders of magnitude will enable a more reliable extrapolation of data to smaller aberrations with future work; however, polishing the optics with such precision is not feasible. The achromat doublets in this experiment are the same that were used in Debes et al. (2004), with rms surface roughnesses of $\lesssim$ 1 nm on spatial frequency scales that correspond to the search area. A better technique to compensate for the scattered light present in the system at this level would be to implement a deformable mirror (Trauger et al. 2004, e.g.).

## 5.4 Summary & Concluding Remarks

We have built and tested three eighth-order notch filter masks and one fourth-order notch filter mask - each with the same IWA - to make a comparitive study of low-spatial-frequency optical aberration sensitivities within the context of Lyot coronagraphy, using monochromatic light. We find that the eighth-order masks are less susceptible to the low-order aberrations of tilt and focus than the fourth-order mask: they provide the same contrast as the fourth-order mask in a system with either $\sim$ 5 times as large a pointing error or $\sim$ 4 times as large an RMS focus wavefront error. Additionally, the eighth-order masks show a stronger dependence to both tilt and focus at large aberration levels (i.e. a steeper slope), as predicted by theory. There was excellent agreement with our results and the SG05 numerical model, once the differences in each study were accounted for. We were unable to extrapolate our data to calculate the exact aberration levels necessary to achieve $\lesssim 10^{-10}$ contrast at the IWA because of the amount of scattered light in the system; doing so would require implementing a deformable mirror to reduce the scattered light levels by approximately two orders of magnitude. Transmission of light directly through the Chromium occulting layer accounted for $\sim$ 10% of the noise floor at the IWA, but significantly less in the extended search area.

With "perfect" alignment, we find that all of the masks generate contrast levels of $\sim 2 \times 10^{-6}$ at $3\,\lambda/D$ and $\sim 6 \times 10^{-7}$ at $10\,\lambda/D$. In essence, the on-axis ('stellar') flux was reduced by 7 orders of magnitude at the expense of attenuating off-axis light by a factor of $4 - 10$. Since our system is "diffraction limited" (i.e. $\gtrsim$ 80% Strehl ratio), we conclude that the $3\sigma$ detection thresholds shown in Fig. 5-4 represent the approximate deepest instantaneous contrast that is achievable from the ground with current AO, using this type of coronagraph.

The Lyot stop throughput penalty in switching from a fourth-order mask to an eighth-order mask was greatly exaggerated in this study, because of nanofabrication limitations. We were able to achieve $\sim$ 31% Lyot stop throughput with the fourth-order

mask and $\sim 10\% - 16\%$ with the eighth-order masks. With a material that is more opaque than Chrome at visible wavelengths, such as Aluminum, eighth-order masks will be able to reach their full potential in future experiments.

These results support the recent theoretical studies of Kuchner, Crepp, & Ge (2005) and Shaklan & Green (2005) suggesting that eighth-order image masks can meet the demands of a space mission designed to image extrasolar terrestrial planets by providing the Lyot coronagraph with a large dynamic range, high off-axis throughput, a large search area, and resistance to low-spatial-frequency optical aberrations.

# CHAPTER 6
# A BAND-LIMITED MASK FOR P.H.A.R.O.

It was shown in Chapters 1 and 4 that large stroke, high bandwidth, high actuator-density DMs are required to detect self-luminous Jovian planets from the ground in the near-IR. These "extreme" AO systems are currently being built and will eventually form the core of next generation high-contrast imaging instruments, such as GPI at Gemini South (Macintosh et al. 2006a), SPHERE at the VLT (Beuzit et al. 2006), and the PALM-3k/P1640 at Palomar (Dekany et al. 2007). However, due to their complexity, they will not be available for another 3-5 years. To test a BLM on a real astrophysical source, we must somehow boost image qualities without replacing the existing DM.

## 6.1 Relay Optics

Fitting errors between the wavefront phase and DM surface limit the ability of an AO system to correct for the atmosphere (Fig. 1-6). For instance, in the case of Kolmogorov turbulence, the residual wavefront variance, $\sigma^2_{\text{fit}}$, can be related to the effective wavefront sensor subaperture size, $d = D_{tel}/N_{act}$, and Fried parameter, $r_0$, by

$$\sigma^2_{\text{fit}} \approx 0.30 \left(\frac{d}{r_0}\right)^{5/3} \text{ rad}^2, \tag{6–1}$$

where the constant of proportionality depends (weakly) on the type of actuator influence function (a Gaussian shape here), $N_{act}$ is the linear number of actuators across the DM, and a least-squares phase-conjugation approach is assumed (Hudgin, JOSA 1977). If the number of actuators in a square grid array used for correction is approximately $\pi(D_{tel}/d)^2/4$, then Equ. 6–1 can be rewritten as

$$\sigma^2_{\text{fit}} \approx 0.25 \left(\frac{D_{tel}}{r_0}\right)^{5/3} N_{act}^{-5/6} \text{ rad}^2. \tag{6–2}$$

In other words, doubling $N_{act}$ (i.e. quadrupling the total number of actuators) reduces the rms wavefront error by a factor of $\sim 1.8$, which in turn improves the instantaneous contrast by a factor of $\sim (1.8)^2$ (§1.2.3). However, increasing the DM sampling by

even a factor of a few, while maintaining minimal electro-mechanical cross-talk between actuators, presents a substantial challenge. A relatively simple method for temporarily side-stepping this obstacle is described below.

DM's are used most often to correct the entire "beam" of starlight, from one edge of the aperture to the other. However, instead of applying corrections over the full diameter of a large telescope, it is possible to improve sampling by correcting only a portion of the pupil. For instance, optics placed between the secondary mirror and AO system can be used to map, or relay, a particular region of the pupil onto the existing DM by shifting and magnifying the beam. The result is an improved spacing between actuators as projected onto the sky.

This concept has recently been demonstrated in practice by Serabyn et al. 2007 at Palomar. They have installed relay optics that turn the Hale 200-inch telescope into a powerful off-axis imager. Fig. 6-1 displays a simplified version of the optical path. A fold mirror inserted before the Cassegrain focus picks off the telescope beam and sends it to a custom circular stop that selects one quadrant of the aperture, conveniently avoiding the central obstruction and secondary support spiders. The relay optics manipulate the beam such that the new pupil fits tightly onto the existing Xinetics 241-actuator Palomar AO system (PALAO) DM (Troy et al. 2000). The net effect is finer sampling at the expense of angular resolution ($D_{tel} = 5.1$m $\rightarrow D_{tel} = 1.5$m) and the brightness of stars for which the AO system can maintain a stable lock (V$<12 \rightarrow$ V$<9$). These tradeoffs are justified since coronagraphs with intrinsically small IWA's can still probe sub-arcsecond separations in the near-IR, where numerous dim companions lay hidden (Veras, Crepp & Ford 2008).

Benefits of the technique can be summarized as follows:

- It is possible to generate extreme-AO-quality wavefronts immediately with only moderate changes to hardware. As a result, one can gain experience with coronagraphy in the high-Strehl regime before the next generation of DM's become available.

- The location and orientation of the subaperture can be chosen so as to avoid vignetting elements, such as the secondary substructure, thus producing an optimal diffraction pattern for the coronagraph.

- PSF stability provides the unique opportunity to develop methods for explicit removal of quasi-static instrument scattered light based on phase diversity (§3).

- Relay optics can be combined with laser-guide-star and upgrades to the DM.

Under good seeing conditions, the relay optics and PALAO have already demonstrated on-sky Strehl ratios of $S \approx 94\%$ in the K-band (Serabyn et al. 2007). We know from Chapter 4 that use of an apodized mask is appropriate only when the Strehl ratio exceeds: $S \gtrsim 0.88\ S_{qs}$, where $S_{qs}$ is the intrinsic Strehl ratio delivered by the instrument ('qs' stands for quasi-static). The near-IR camera PHARO at Palomar consistently provides image qualities exceeding $S_{qs} \gtrsim 0.95$ for sources near the optical axis. Thus, Equ. 4–8 is indeed satisfied. These considerations serve as the technical justification for building the first band-limited coronagraphic image mask for on-sky tests. The remainder of the chapter outlines the design of such a device (§6.2), its performance with the PALAO stimulus (§6.3), and preliminary on-sky tests (§6.4).

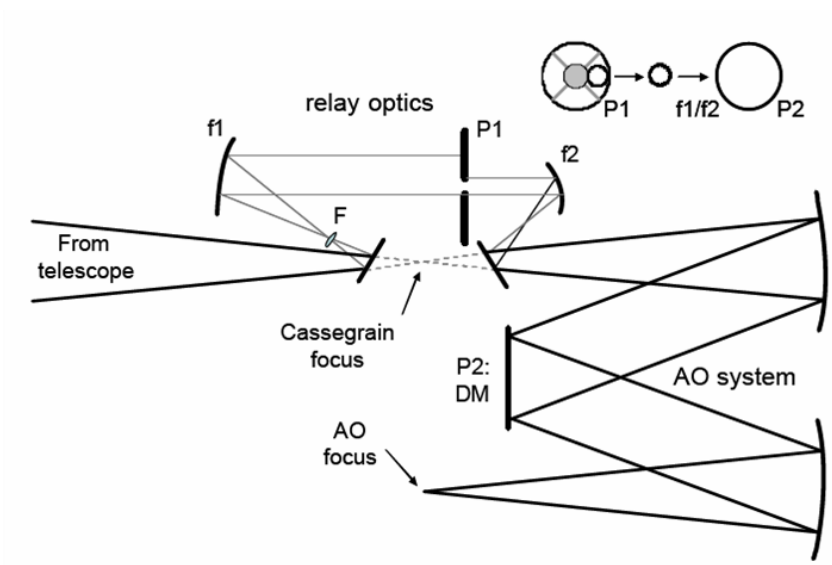


Figure 6-1. Layout of the Hale 200-inch relay optics, courtesy of Eugene Serabyn.

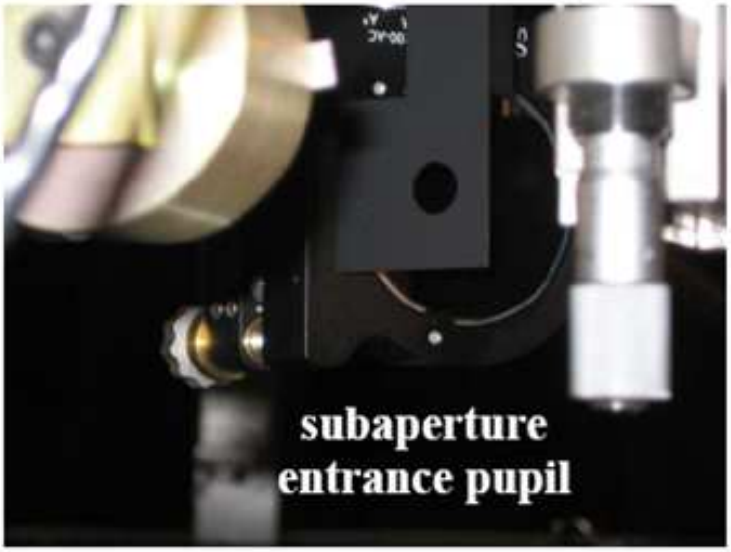


Figure 6-2. Image of the relay optics subaperture pupil at the Hale 200-inch telescope. Light from only one quadrant of the full aperture is used.

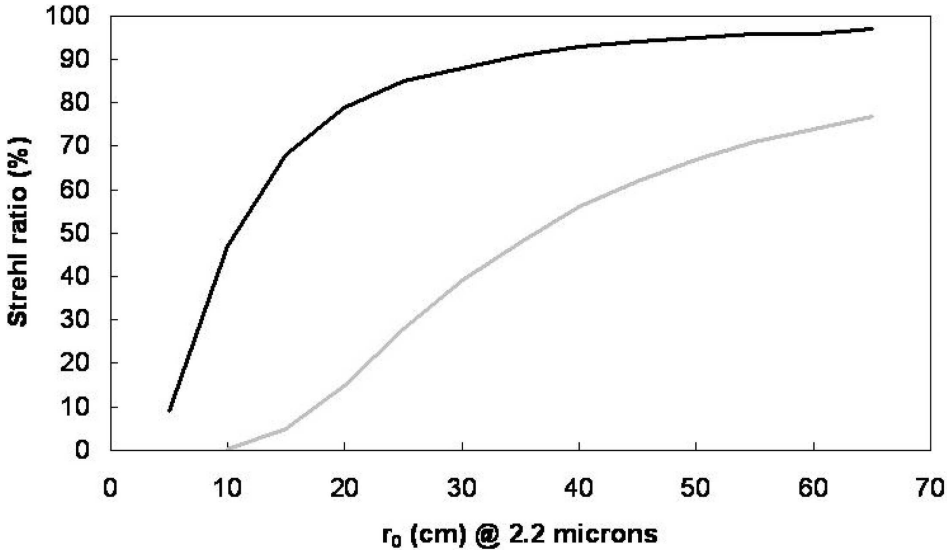


Figure 6-3. Predicted Strehl ratio as a function of the Fried parameter, $r_0$, in the K-band at the Hale 200-inch telescope with relay optics (top curve) and without (bottom curve), courtesy of Gene Serabyn.

## 6.2 Design & Fabrication

The Palomar High Angular Resolution Observer (PHARO) is a near-IR imager / spectrograph with a coronagraphic operating mode (Hayward et al. 2001). It utilizes a 1024 x 1024 HgCdTe HAWAII detector that is sensitive from $1.0 \leq \lambda \leq 2.5\mu$m, with read noise typically $< 10\ e-$ / pixel. Spectrographic and coronagraphic image masks are housed in a slit wheel in the first image plane, where there are 10 available slots. Filter, grism, and Lyot stop wheels are located further downstream near the pupil. Figure 6-4 shows a schematic of the instrument.

A 25 mas / pixel plate scale mode enables critical sampling of diffraction-limited images from the full Hale 200-inch aperture in the J-band. With relay optics in place, the plate scale changes by the ratio of the telescope diameter, 25 x 5.093 / 1.5 = 84.88 mas / pixel. We have designed a mask for the K-band, where the sampling corresponds to $\sim 3.6$ pixels per diffraction width. The K-band offers better image qualities than the J-band, but the sky background is brighter.

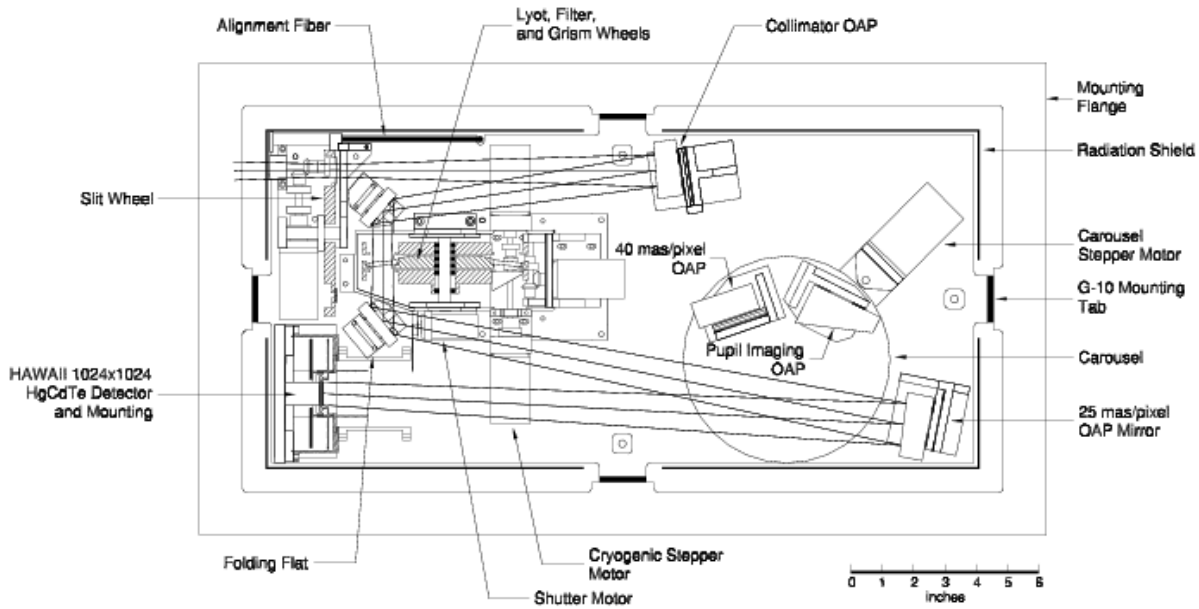


Figure 6-4. Component layout of the PHARO near-IR camera, courtesy of Tom Hayward.

### 6.2.1 Binary Image Mask

The focal ratio at the slit wheel and bandpass constrain the range of possible coronagraphic mask designs. Fast optical systems can force the size of features in the image plane to be too small whereas broad wavelength coverage affects the IWA and Lyot stop throughput. These tradeoffs are important with binary masks (§5) since they can potentially leak light at both ends of the bandpass, but graded masks, which can leak light only at long wavelengths, are made from HEBS glass and therefore more expensive. Other interesting performance differences exist between the list of potential designs – smooth binary, sampled binary, smooth graded, and sampled graded – such as polarization dependence and chromaticity (Lay et al. 2005), but they are unimportant at the sensitivities achievable from the ground. Since we have the tools and experience to build binary masks, we built a binary mask for PHARO.

PHARO receives an f/15.64 beam from the PALAO system. The desired operation range for our observations includes the $K_{short}$: $1.99 - 2.30$ $\mu$m, $Br_{\gamma}$: $2.16 - 2.18$ $\mu$m, and CO: $2.29 - 2.31$ $\mu$m filters. The $K_{short}$ filter serves as the primary science channel whereas independent experiments in all three filters can be used to measure any chromatic dependent performances, should they exist, since only monochromatic tests were previously conducted in the lab (Crepp et al. 2006). To prevent diffracted light leakage from the edges of the filter transmission profiles, the minimum and maximum wavelengths, $\lambda_{min} = 1.79$ $\mu$m and $\lambda_{max} = 2.39$ $\mu$m, were chosen conservatively.

Two different masks were designed and built: a linear fourth-order smooth binary notch filter mask and a linear hard-edge binary mask (Crepp et al. 2007). The latter of which was used as a baseline to make comparative studies. An eighth-order mask design, which has less Lyot stop throughput than a fourth-order mask, could not be justified, given the already large sacrifice in photons from the relay optics. Each mask was designed with the same aggressive IWA $= 2.678$ $\lambda_{max}/D_{tel} = 880$ mas. They were placed adjacent to one another on the same 0.7 mm thick Boro-Aluminosilicate glass substrate, Corning

model 1737 – 10/5 scratch/dig[1] , with sufficient separation to ensure that diffracted light cross-talk was negligible. The K-band glass transmission is quoted at 92%.

The masks were fabricated using $e$-beam lithography at the University of Florida nanofabrication facility in June 2006. Aluminum was used as the opaque material deposit, since it is less transmissive than Chrome (§5) in the near-IR. Lab measurements placed an upper limit on the intensity transmission directly through the 200 nm layer of Aluminum at $1 \times 10^{-7}$. The minimum feature size was set equal to the layer thickness.

The height, $\hat{M}_{\rm notch}(x)$, of a single stripe of the smooth binary linear band-limited mask (see Equ. 2–17; binary masks are technically notch filter masks) is:

$$\hat{M}_{\rm notch}(x) = f/\#\,\lambda_{min}\left[1-{\rm sinc}^2\left(\frac{\pi\epsilon x}{2\,f/\#\,\lambda_{max}}\right)\right]\ \mu{\rm m} \tag{6–3}$$

$$= 28\left[1-{\rm sinc}^2\left(\frac{0.0179857\,x}{\mu{\rm m}}\right)\right]\ \mu{\rm m}, \tag{6–4}$$

where $\epsilon = 0.428$ and $x$ has units of $\mu$m. This profile was repeated vertically 256 times. The key to the binary mask's operation is that each stripe is smaller than the resolution of the optical system, hence allowing it to diffract light like a graded mask. The hard-edge mask design is much simpler; it is literally a bar of width $2\,f/\#\,2.678\,\lambda_{max} = 200\mu$m.

Figure 6-6 shows images of the mask before it was shipped to JPL, where it was cut out of the substrate with a dicing saw to physical dimensions of 0.60 x 0.30 inches and then cleaned in an ultrasonic bath of acetone to remove the protective layer of photoresist. Simulations were run to ensure that truncation at the edge of the mask would not diffract starlight into the search area at contrast levels above $10^{-6}$. The mask was installed in PHARO in September 2006.

[1] A scratch is a defect on a polished optical surface whose length is many times its width. A dig is a defect on a polished optical surface that is equal in terms of its length and width. A scratch/dig of 10/5 indicates that the average length of a scratch is 0.10 mm and the average diameter of a dig is 0.05 mm (http://www.esourceoptics.com/).

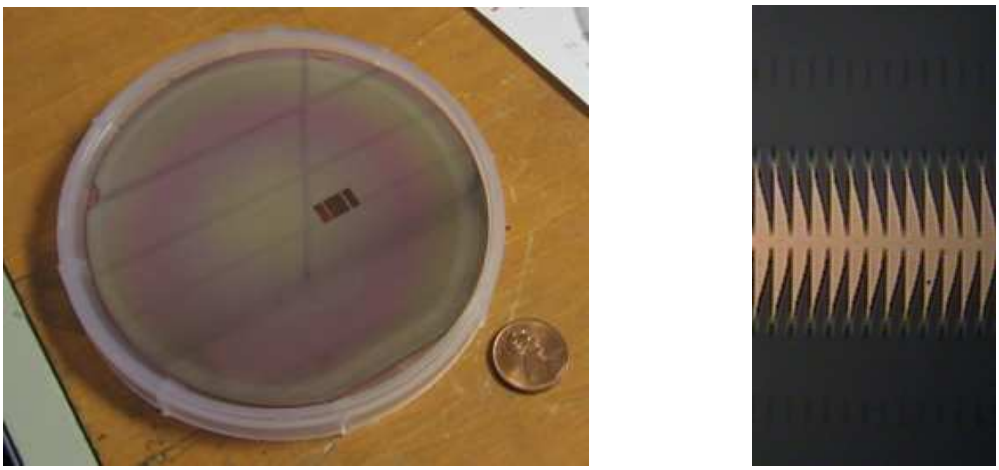

Figure 6-5. (left) The binary mask after $e$-beam lithography. A thick layer of photoresist was applied to protect the surface for shipping to JPL. (right) Microscope image of the band-limited mask. Each stripe is 28 $\mu$m wide. 'Ringing' features in the $\mathrm{sinc}^2(...)$ function (6–4), which are responsible for controlling diffracted light, can be seen above ($x > 0$) and below ($x < 0$) the main occulting region.

### 6.2.2 Aluminum Fastener & Lyot Stop

An Aluminum holder was built to fasten the coronagraphic mask to the PHARO slit wheel (Figs. 6-6, 6-7). The design incorporated a single solid piece, instead of two separate fasteners, to facilitate installation. It was necessary to allow extra space for thermal contraction since PHARO operates at 77 K. The thermal contraction of the glass substrate and differential contraction between the glass and thin layer of Aluminum deposit on the mask were negligible. The masks are oriented perpendicular to the direction of rotation of the PHARO slit wheel. This is an important detail and has implications for the science conducted in Chapter 7.

The physical size of the pupil at the Lyot plane in PHARO is 16.88 mm (Hayward et al. 2001). A band-limited mask will diffract light into a region that is smaller than this value by a factor of $1 - \epsilon$. A custom circular Lyot stop of clear diameter $(1 - 0.428) * 16.88\,\mathrm{mm} = 9.65\,\mathrm{mm}$ was built at the University of Florida using a laser cutter (Fig. 6-8). The total throughput of an off-axis source at 880 mas, including attenuation from the band-limited image mask and Lyot stop, is $\approx 16.3\%$. The throughput increases to $\approx 33\%$ for sources further from the optical axis.

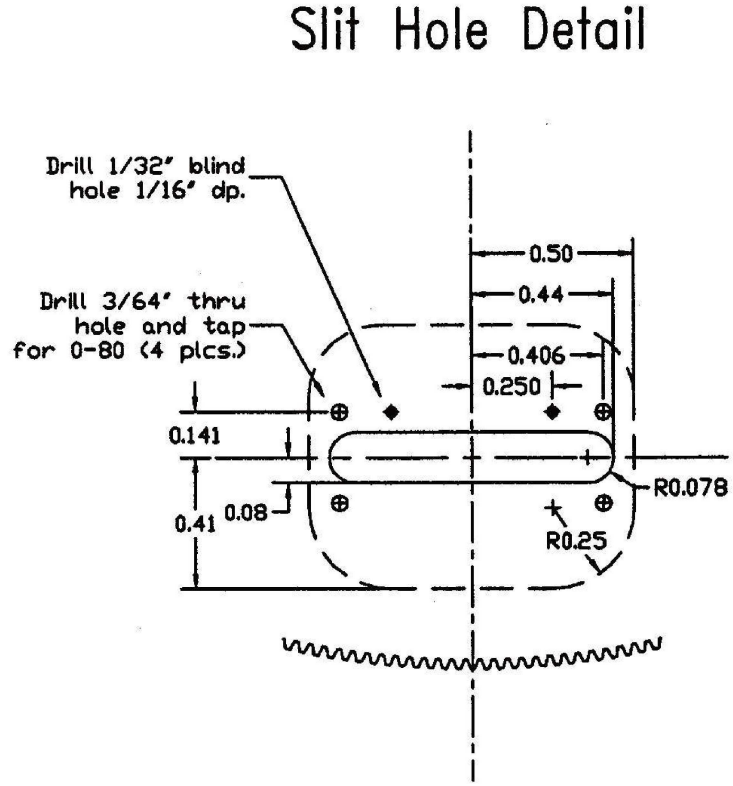


Figure 6-6. Available slot in PHARO image plane wheel. The units are inches.

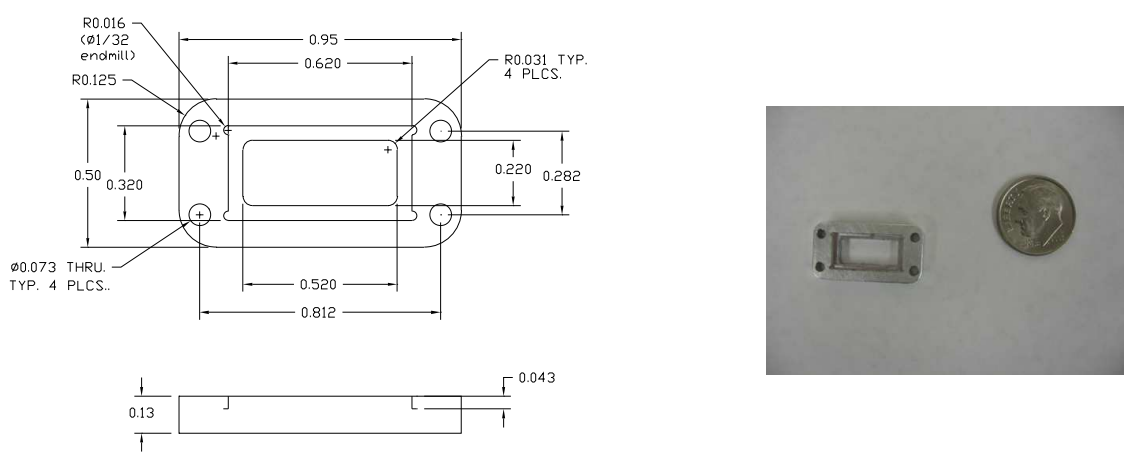


Figure 6-7. Aluminum fastener made with ±0.003 inch precision at the University of Florida machine shop.

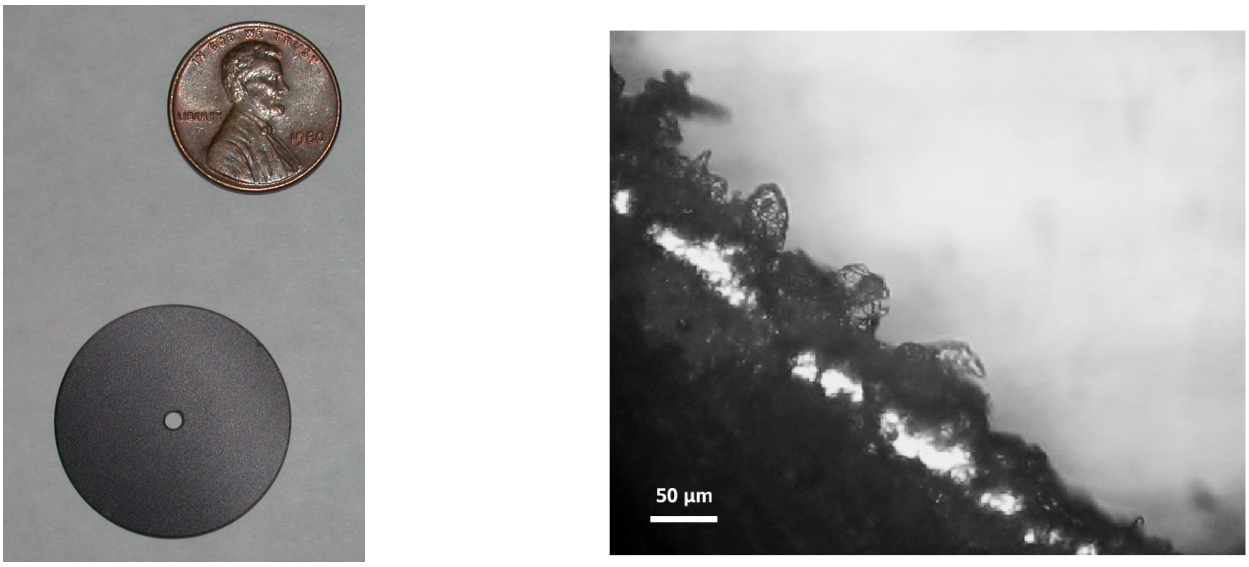


Figure 6-8. Lyot stop installed in PHARO. The University of Florida laser cutter provides cuts that are rough on the order of tens of microns. This roughness does not limit sensitivity.

## 6.3 White Light Tests

A typical observing run begins with installation of the relay optics. Alignment takes anywhere from 4-8 hours depending on the circumstances. With the remaining daylight hours it is possible to conduct lab experiments using the PALAO stimulus. This white light source well-simulates a G-dwarf star and passes through most of the optics before reaching PHARO. Experimental tests were conducted with the new binary coronagraphic mask in December 2006, April 2007, and May 2008 during the daytime and when conditions were poor after nightfall.

The goals of the tests were to:

- confirm that the coronagraphic masks suppress diffraction
- calculate contrast – presumably, on-sky observations can never do better
- identify effects that limit sensitivity
- study differences in performance between the BLM and hard-edge mask
- study the masks' chromatic behavior

Results are shown in Figs. 6-9 and 6-10 where each of the bullet points are addressed.

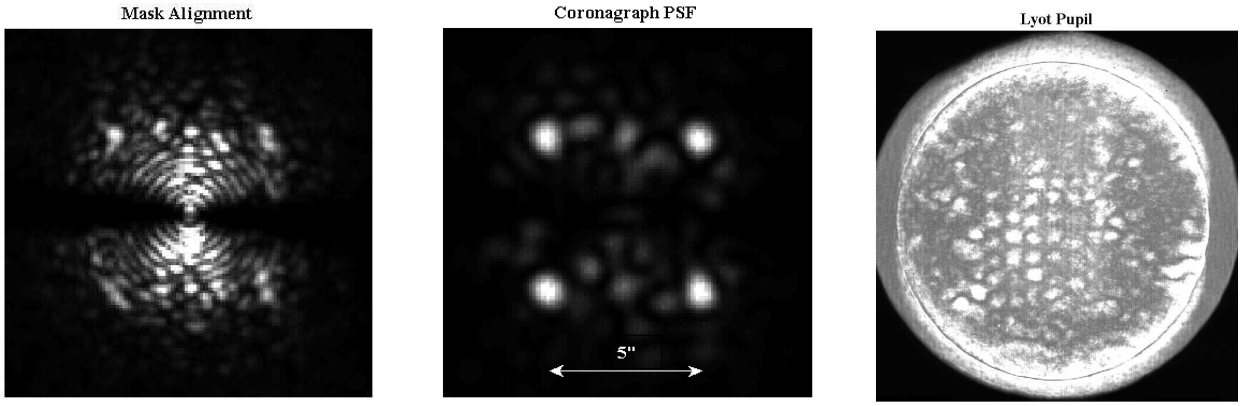


Figure 6-9. PHARO images with BLM aligned to the white light source. (left) Optimal mask position is found using the PHARO stepper motor with the Lyot stop *out* of the beam. (middle) Resulting coronagraphic PSF with Lyot stop in place. The Airy rings have been removed. The waffle-mode peaks (Makidon et al. 2005) are ≈1,000 times fainter than the stellar peak intensity and clearly visible. In fact, they saturate PHARO if the integration time is not limited. (right) Pupil image showing diffracted starlight pattern and residuals from non-common-path errors. Compare this image with Fig. 5-6.

We find that both coronagraphic masks are capable of suppressing diffraction and that the sensitivity is limited by non-common-path errors between the AO system and the detector. The DM corrects for wavefront errors introduced upstream from its position in the optical path but is blind to errors introduced downstream, such as those created by fold optics and the coronagraph itself. Fig. 6-9 shows how the peaks of residual starlight near the interior of the Lyot pupil correspond to the position of actuators on the DM. Since phase errors in the DM pupil generate intensity errors at the Lyot pupil, we know that the DM shape is not fully optimized. This is not surprising given that the wavefront is sensed before the science camera.[2] The amount of light remaining in the central portion of the Lyot plane suggests that sensitivities can improve by an order of magnitude with future experiments using the BLM.

[2] Recall that the complex field was measured at the final image plane in §3.2.3.

Fig. 6-10 displays sensitivity curves for a variety of experiments and a theoretical on-sky prediction for comparison (see §4.3). Contrast is currently limited to $\approx 3 \times 10^{-4}$ at the IWA, or one order of magnitude below the Airy pattern. The green and brown curves indicate that the BLM and hard-edge mask have a similar performance but that the hard-edge mask is better at filtering low-order content – a result that is consistent with a system with large static aberrations (§4.3.3, §5.3.3). These (non-common-path) errors create an intensity 'plateau' near the edge of the DM control region which can also be seen in Fig. 6-9. The blue BLM curve shows the relative improvement in sensitivity near the optical axis when the DM shape is iteratively tuned using the first several Zernike modes by measuring the intensity at the detector. We were unable to fully optimize the DM

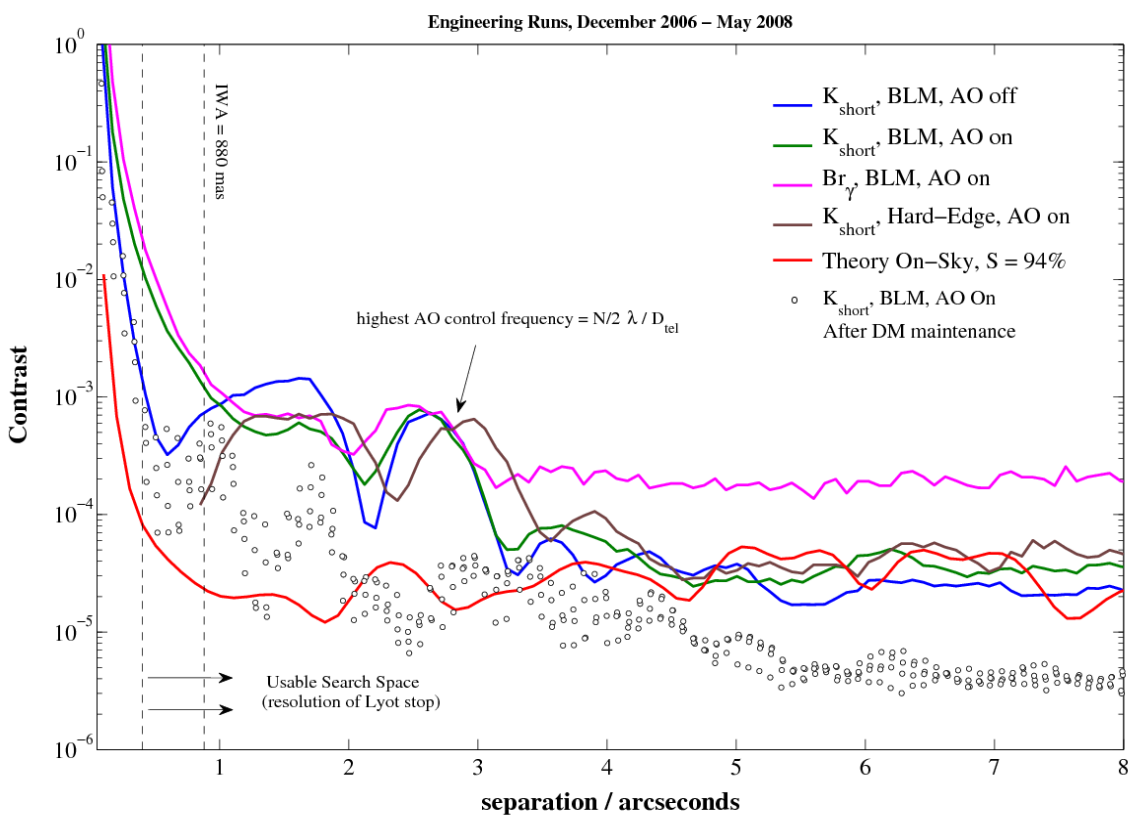


Figure 6-10. Experimental contrast results using the PALAO internal white light source. No post-processing tricks, such as PSF subtraction, have been applied. The BLM can make detections inside of the 0.88" IWA but no closer than the Lyot stop spatial resolution limit.

shape with the canonical observing staff and hours of operation. More formal engineering time will be scheduled in the near-future.

All measurements taken prior to Fall 2007 were acquired at a time when two of the DM actuators were pinned. Their lack of response to instructions scattered a significant amount of starlight. Maintenance to fix these actuators resulted in a noticeable improvement (black circles) allowing sensitivities to approach the theoretical expectation.

There appears to be no significant chromatic issues. Data taken with the $Br_\gamma$ filter in December 2006 (pink curve) closely follows the other sensitivity curves with the exception that the integration time was not sufficiently long: the $Br_\gamma$ bandpass is 15 times narrower than $K_{short}$. We also confirmed that the BLM *does* leak diffracted starlight in the J-band where the mask stripes are no longer smaller than $\lambda_{min}/D_{tel}$ (see §2.3.1).

We were unable to test the effects of mask defects on the speckle noise floor, since the white light source did not have a translation stage to shift its position within the FOV.[3] Significant changes to the speckle pattern as the white light source is moved down the long axis of the mask would indicate that it makes non-negligible contributes to the static error budget. We have no reason to expect the mask itself would scatter a large amount of light but its features are three times smaller than the masks built in §5. Nevertheless, a DM can compensate for such static errors (§3.2.3).

### 6.4 On-Sky Demonstration

In this section, we report results from the first on-sky demonstration of a band-limited coronagraphic mask. This study also represents the first tests of a TPF-C front-running candidate design operating in tandem with an extreme AO system. We are sensitive to brown dwarf companions over a wide range of ages and very young massive exoplanets. Contrast is limited by a combination of AO lag time and the non-common-path errors described above. Target selection is discussed in §7.

[3] However, one was recently installed (A. Bouchez, private communication).

### 6.4.1 Data Acquisition & Reduction

There are three critical sets of images required to calculate the companion mass-sensitivity for observations of a given star. In addition to the usual darks and flats, one must obtain: (i) non-coronagraph images, where the star is *not* occulted by the mask, in order to determine the throughput of an off-axis source, $I(0,0)$ (see §3.2.3); (ii) coronagraphic images, where the star is occulted by the mask, for the obvious reasons; and (iii) off-source images, for calibration of the bright sky background. It is also useful to obtain on-source images with the DM off to measure the seeing.

The total time spent on a bright source is often 30-45 minutes with a duty cycle efficiency of roughly 30%, when including the time necessary to slew to the target, place it within the unvignetted region (see Fig. 6-11), close the AO loop, and align the mask. Nearly 30% of the time is spent on the sky background. More overhead is required when the "flex-cam" is running. The flex-cam picks off unused blue light from the wavefront sensor beam and sends extra tip/tilt instructions to the DM to maintain precise mask alignment by correcting for differential drifts (flexures) that occur between the telescope and PHARO over the length of an exposure.

Once the images (.fits files) are in hand, they are backed up and processed with an in-house Matlab program designed specifically for PHARO high-contrast data. A simplified description of the reduction procedure is as follows:

- upload and tile the four separate read-out quadrants of the PHARO array
- cull pertinent information from .fits header
- apply flat field to correct pixel-to-pixel sensitivity variations (Fig. 6-11)
- determine peak intensity of the star, $I(0,0)$, with AO locked
- median combine coronagraph PSF images with sub-pixel precision using high-pass Fourier filter, 2D cross-correlation, Gaussian fit, and flux redistribution routines similar to the "Drizzle" method employed by Fruchter & Hook (2002)
- subtract sky background

- fix bad pixels
- scale the final coronagraph PSF image by the appropriate factors, including integration time and neutral density filters used, to obtain the relative intensity
- obtain contrast by dividing the relative intensity by the mask intensity attenuation profile incorporating the mask angle and errors in alignment
- calculate standard deviation in contrast over the search areas of interest, typically a $\lambda_{max}/D_{tel}$ wide strip above and below the mask
- convert contrast to $5\sigma$ sensitivity levels in terms of Jupiter masses using the Baraffe et al. (2003) substellar atmospheric models

### 6.4.2 HIP 72567

We observed the star HIP 72567 on 2007-04-29 (UT) using the BLM. Its X-ray activity, lithium abundance, rotation, and space motion suggest that is has an age

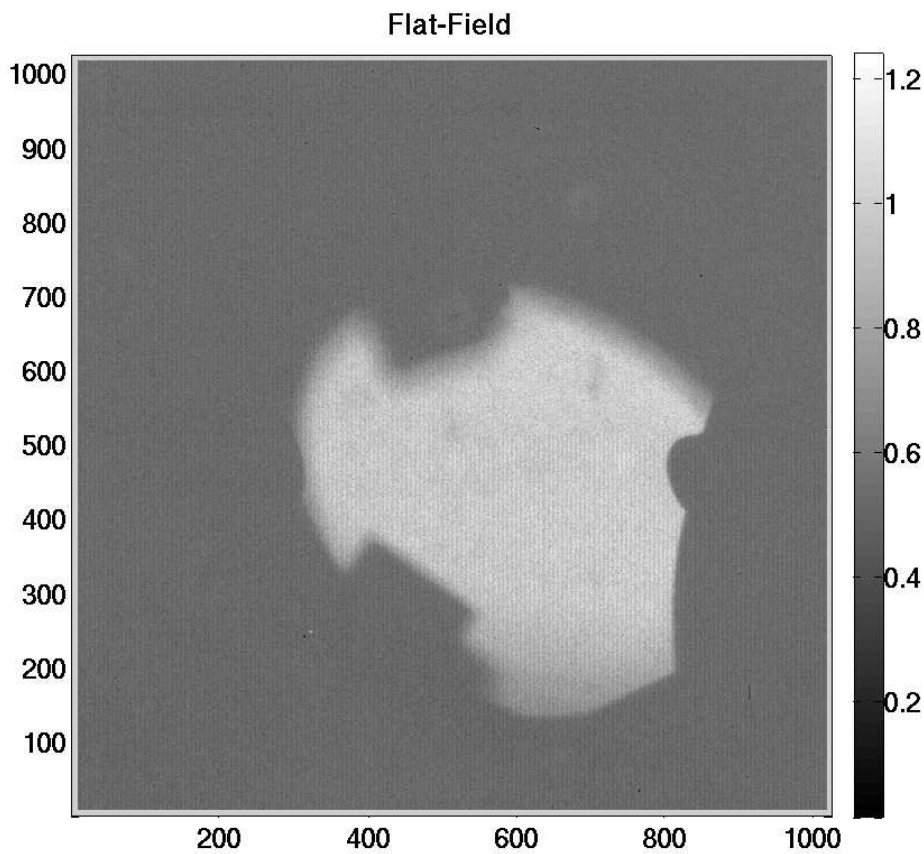


Figure 6-11. Flat-field image showing relay optics vignetting elements. Stars must be placed within the central region that resembles Africa.

of 300 − 800 Myrs (Potter et al. 2002; Gaidos et al. 2000), making it an excellent high-contrast imaging target. Table 6-1 lists the star's physical parameters and other important observational information, including the Smithsonian Astrophysical Observatory number (SAO), J2000 right-ascension (RA) and declination (DEC), distance in parsecs, spectral type, apparent visual magnitude (V), approximate age, total exposure time on source ($\Delta t_{source}$) and on sky ($\Delta t_{sky}$), median airmass, seeing, and Strehl ratio.

Table 6-1. Physical parameters and observational information for HIP 72567.

| | | | |
|---|---|---|---|
| SAO = 83553 | distance = 17.9 pcs | age = 300-800 Myrs | airmass = 1.07 |
| RA = 14 50 15.8 | sp. type = G2V | $\Delta t_{source}$ = 595 s | seeing = 1.3" |
| DEC = +23 54 42.6 | Vmag = 5.9 | $\Delta t_{sky}$ = 595 s | Strehl = $77.8 \pm 0.9$ |

Figs. 6-12 and 6-13 show the star with and without the coronagraph. A high-pass Fourier filter has been applied to amplify the signal of sources with intrinsic widths of order $\lambda_{max}/D_{tel}$ or smaller compared to low-frequency (i.e. blurry) structure. Several Airy

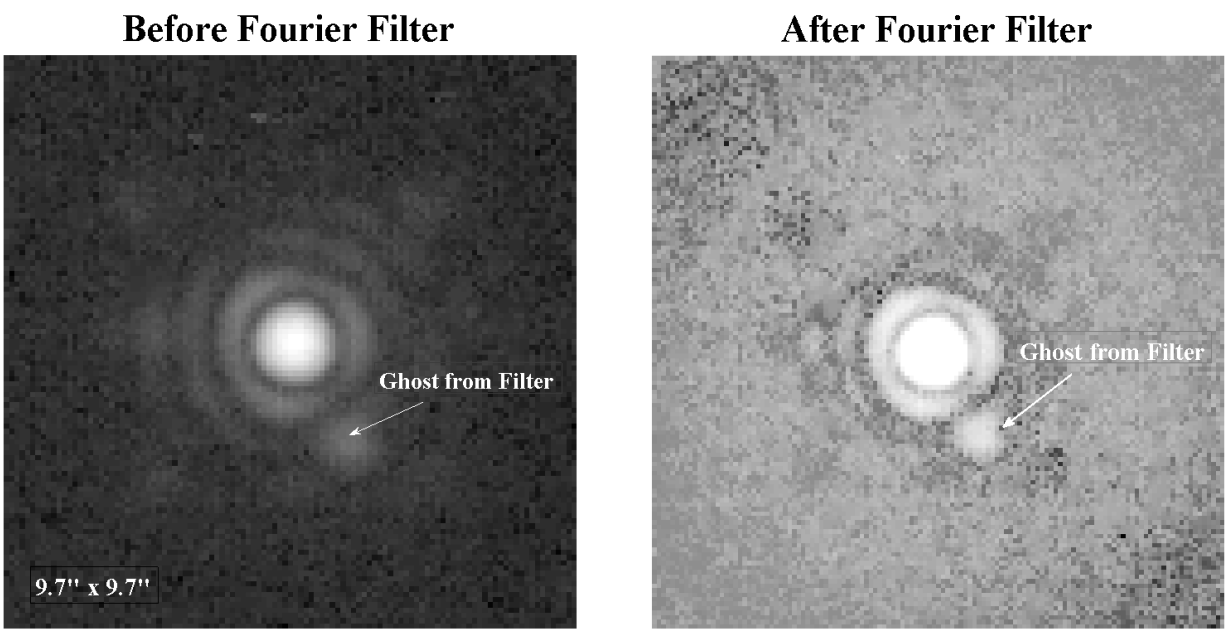


Figure 6-12. Calibration image of HIP 72567 used to calculate the Strehl ratio and off-axis throughput. Image intensities are on a logarithmic stretch and the FOV is the same in each. Fourier filtering can artificially enhance the photometric signature of a companion. This companion is not real but the result of an internal reflection from a neutral-density-filter.

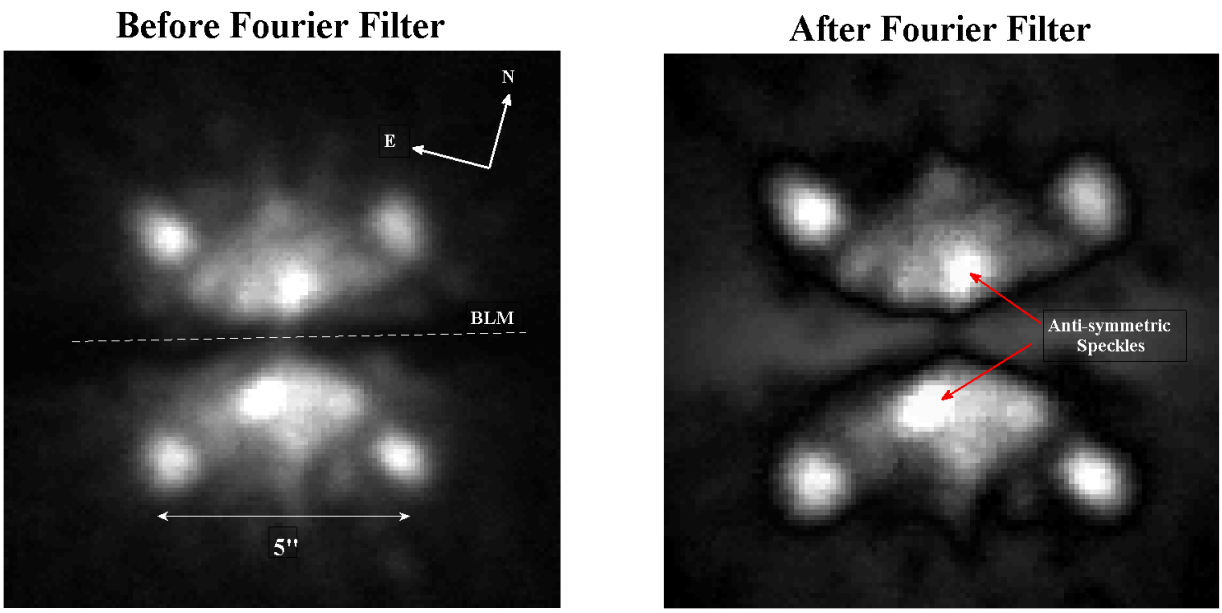


Figure 6-13. Fully processed coronagraphic images of HIP 72567 before and after Fourier filtering. Fourier filtered data are also used internally by the reduction code to facilitate precision stacking of individual images prior to median combination. The orientation of the BLM is indicated by a dotted line. The ghost from Fig. 6-12 is no longer present because the neutral-density-filter was removed to maximize flux.

rings can be seen before the BLM and Lyot stop combination suppress the star to reveal features in its immediate vicinity. The four waffle-mode peaks ($C \approx 1 \times 10^{-3}$) can barely be detected in the calibration image, but are clearly visible with the coronagraph in place. Exact contrast levels are shown in Fig. 6-14 and 6-15.

Anti-symmetric speckles due to quasi-static wavefront phase errors can be seen above and below the mask. It is possible to exploit this symmetry[4] by flipping, folding, and subtracting the image, but we find that the effective contrast does not improve significantly. This line of reasoning is precisely what has lead to the development of simultaneous differential chromatic (Close et al. 2005), polarimetric (Perrin et al. 2008), and spatial imaging (Marois et al. 2006). That is, the structure of quasi-static speckles

[4] Amplitude errors are a $<10^{-8}$ effect (§3) and thus always negligible from the ground.

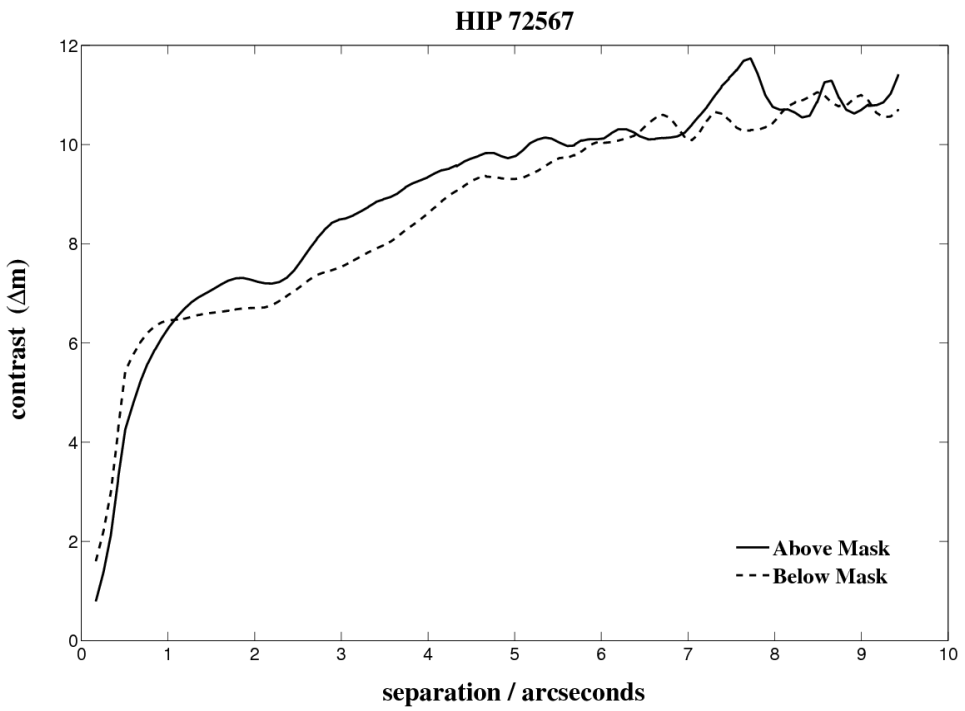


Figure 6-14. HIP 72567 coronagraph sensitivity above and below mask in magnitudes.

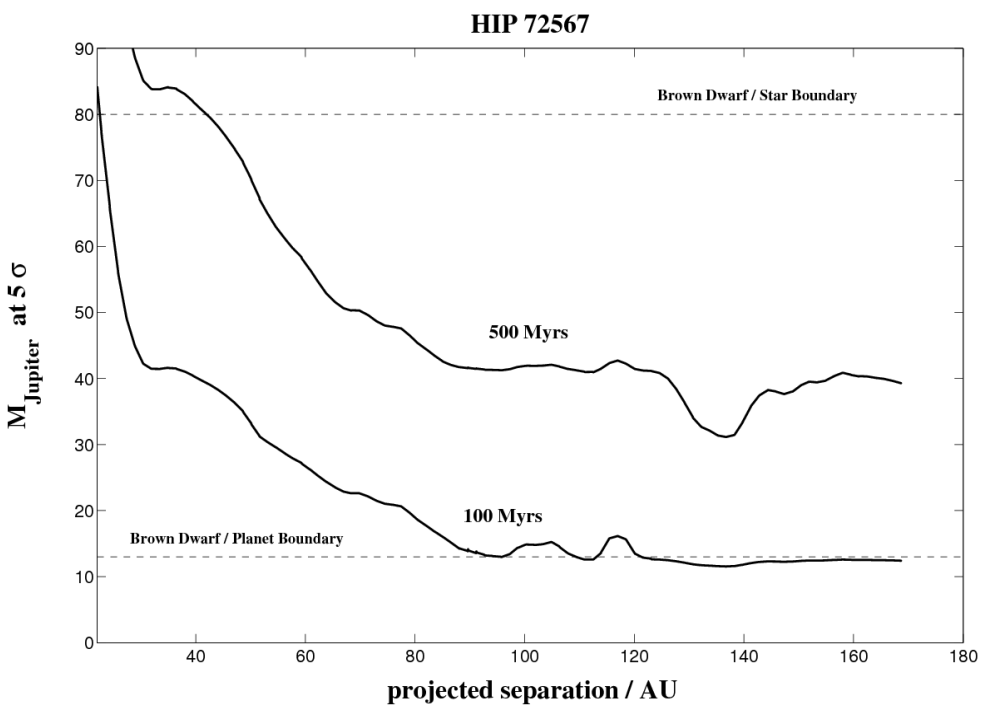


Figure 6-15. HIP 72567 coronagraph sensitivity in Jupiter masses as a function of age.

changes on a timescale shorter than typical integrations, which last several minutes. Close inspection of Fig. 6-13, for example, shows that the bright speckles do not have the same shape nor intensity. This logic likewise applies to PSF subtraction using a nearby star. In the near-future (2009), we will be the only high-contrast imaging group capable of *explicitly* removing this dominant source of noise. PSF stability provided by the relay optics affords us the opportunity. The Strehl for this particular target was low, but not characteristic of the performance.

Upon converting the contrast levels from Fig. 6-14 to companion mass at $5\sigma$ (Fig. 6-15), where $\sigma$ is the local standard deviation in the signal, we find that we are sensitive to M-dwarfs, brown dwarfs, and very young, very massive, and very distant planets, such as those shown in §1.2.1.3. HIP 72567 is the first star ever to be observed with a BLM or any legitimate TPF-C design candidate.

We note that this star is actually a triple system with a faint brown-dwarf-brown-dwarf pair orbiting at 2.6" from the primary (Potter et al. 2002). We are capable of detecting this set of companions, but they are located at an inopportune position angle and were completely occulted by the BLM. This circumstance is the result of not knowing a priori the ring angle of the imaging system with the relay optics in place. This was the first observing run, and the angle changes slightly with each installation by an amount comparable to the slit-wheel stepper motor range of motion within the FOV, which also changes location. (This is the strongest selection constraint when we target visual binary stars in §7.) It is possible to rotate the Cass-cage by $90^o$ increments, which would permit detection of HIP 72567BC, but we did not get a chance to go on-sky with the (non-default) orthogonal orientation in April 2007 or May 2008.

### 6.4.3 HIP 83389

We observed the star HIP 83389 on 2007-04-29 (UT) using the BLM. Its physical parameters along with relevant observational information are shown in Table 6-2. This star is intriguing because it hosts a Jupiter-like exoplanet (M sin i = $0.95 M_{Jupiter}$, a=4.2

Table 6-2. Physical parameters and observational information for HIP 83389.

| | | | |
|---|---|---|---|
| SAO = 46452 | distance = 18.1 pcs | age = 0.5-9 Gyrs | airmass = 1.03 |
| RA = 17 02 36.4 | sp. type = G8V | $\Delta t_{source}$ = 595 s | seeing = 1.0" |
| DEC = +47 04 54.8 | Vmag = 6.7 | $\Delta t_{sky}$ = 297 s | Strehl = $84.6 \pm 0.4$ |

AU, e=0.04; (Wright & Vogt 2008, in press)). The multiplicity of exoplanet host stars is at least 20% (Mugrauer et al. 2007) and a brown dwarf has recently been directly imaged orbiting the star HD 3651, which hosts an eccentric sub-Saturn-mass planet at 0.3 AU (Fischer et al. 2003). HIP 83389 is also on M. Turnbull's list of "habstars" for SETI and the TPF missions (Turnbull 2008).

Although this star does not exhibit signs of youth, we are sensitive to massive brown dwarfs exterior to 60 AU (Figs. 6-16, 6-17, and 6-18.). The contrast is limited by AO latency ($f_{DM}$ = 200 Hz) and systematic tip/tilt alignment errors (§4.3.3, §5.3.3) as a result of flexure between the Cass-cage and telescope (flex cam was not operational). Depending on the position of targets in the sky, the flexure may be more problematic. At times, the drifts conveniently follow the opaque portions of the linear mask, but, in this case, movements were in the orthogonal direction.

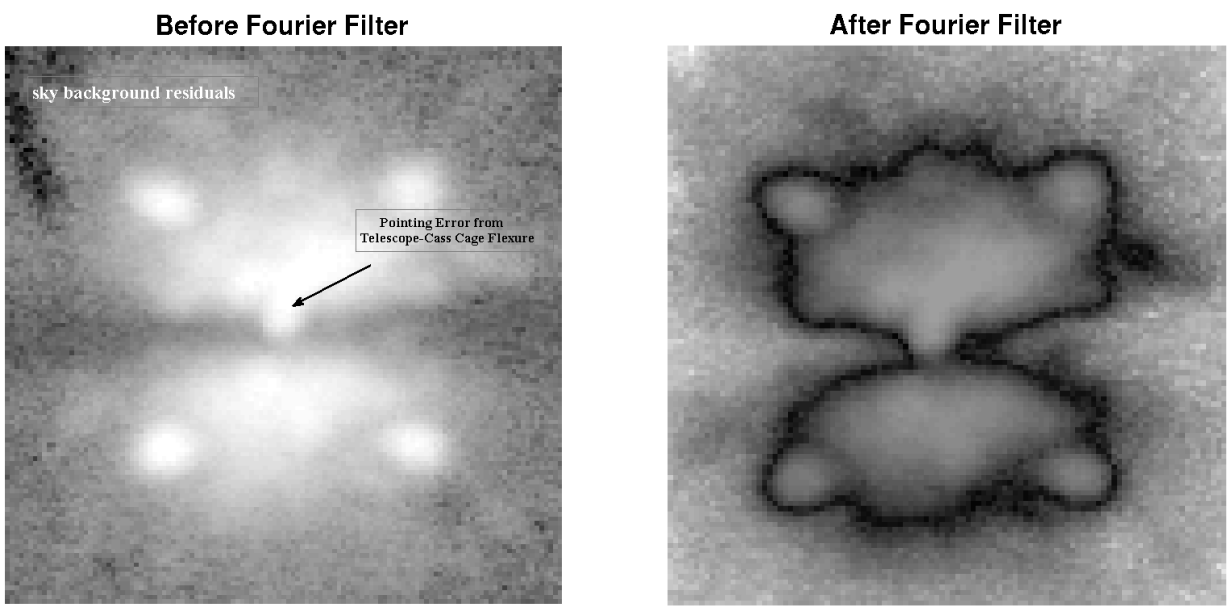


Figure 6-16. Fully processed coronagraphic images of HIP 83389.

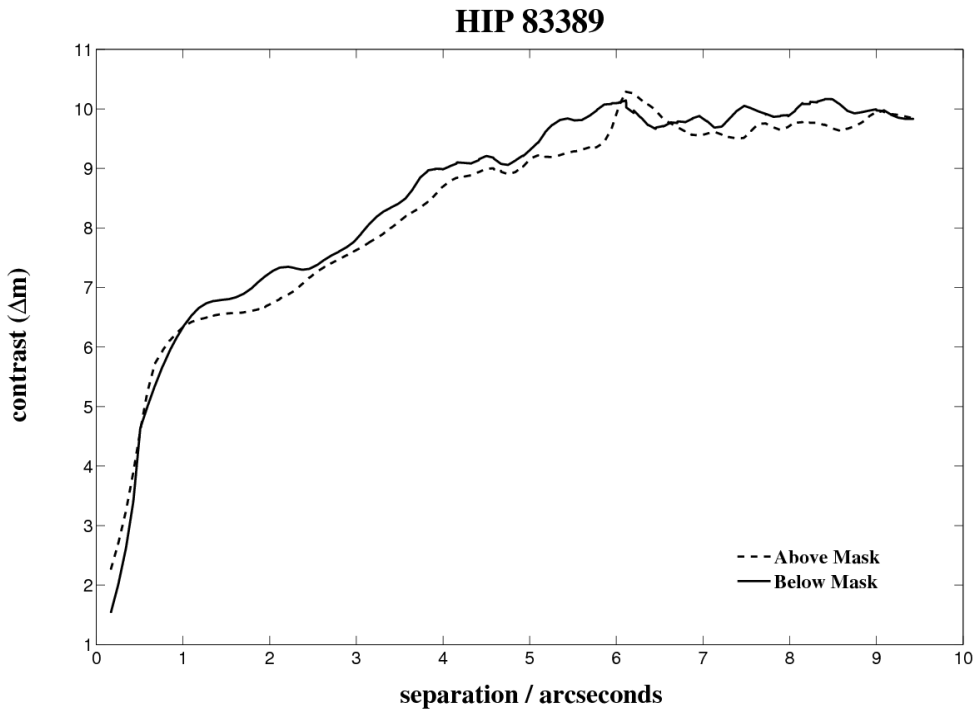


Figure 6-17. HIP 83389 coronagraph sensitivity above and below mask in magnitudes.

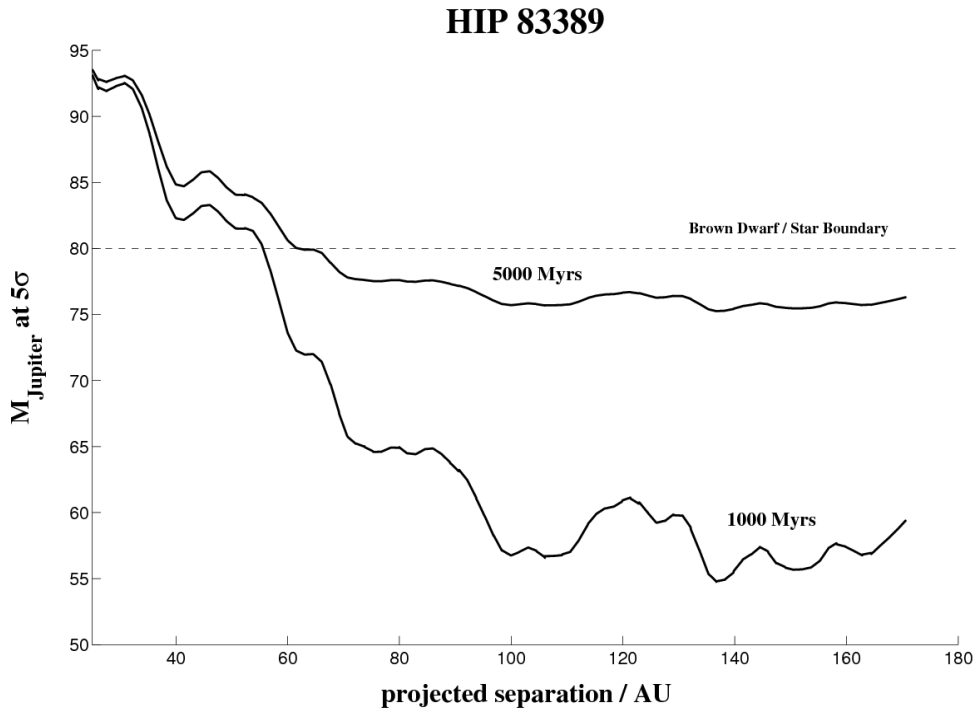


Figure 6-18. HIP 83389 coronagraph sensitivity in Jupiter masses as a function of age.

### 6.4.4 HD 102195, a.k.a. ET-1

We observed the star HD 102195 on 2007-04-30 (UT) using the BLM. HD 102195 is also known as "ET-1" and is the first planet-bearing star that the local University of Florida radial velocity team discovered (Ge et al. 2006). Throughout graduate school, I spent 40 nights at Kitt Peak National Observatory using the single object Exoplanet Tracker (ET) RV instrument and 31 nights at Apache Point Observatory using the multi-object Keck-ET RV instrument. I thought it would be interesting to target this star and place limits on the presence of substellar companions. HD 102195 also appears to be relatively young, although uncertainties still remain regarding its age. Its physical parameters and relevant observational data are shown in Table 6-3.

Sensitivity was limited by AO latency errors as is indicated by the blurring pattern seen surrounding the mask in Fig. 6-19. The DM refresh rate was again set to only 200 Hz, in order to collect sufficient flux in each wavefront sensor subaperture. The faintest target for which the relay optics will provide a substantial boost in Strehl is Vmag=9.

We were able to rule out substellar companions orbiting exterior to 50 AU down to the levels shown in Fig. 6-21. There are no brown dwarfs more massive than: 25 $M_{Jupiter}$ and younger than 100 Myrs outside of $\approx$ 125 AU; 50 $M_{Jupiter}$ and younger than 500 Myrs outside of $\approx$ 150 AU; and 70 $M_{Jupiter}$ and younger than 1 Gyrs outside of $\approx$ 150 AU (Baraffe et al. 2003) at $5\sigma$ above the noise floor.

Table 6-3. Physical parameters and observational information for ET-1.

| | | | |
|---|---|---|---|
| SAO = 119033 | distance = 29.0 pcs | age = 0.6-4.2 Gyrs | airmass = 1.19 |
| RA = 11 45 42.3 | sp. type = K0 V | $\Delta t_{source}$ = 595 s | seeing = 1.2" |
| DEC = +02 49 17.34 | Vmag = 8.1 | $\Delta t_{sky}$ = 297 s | Strehl = $75.4 \pm 0.7$ |

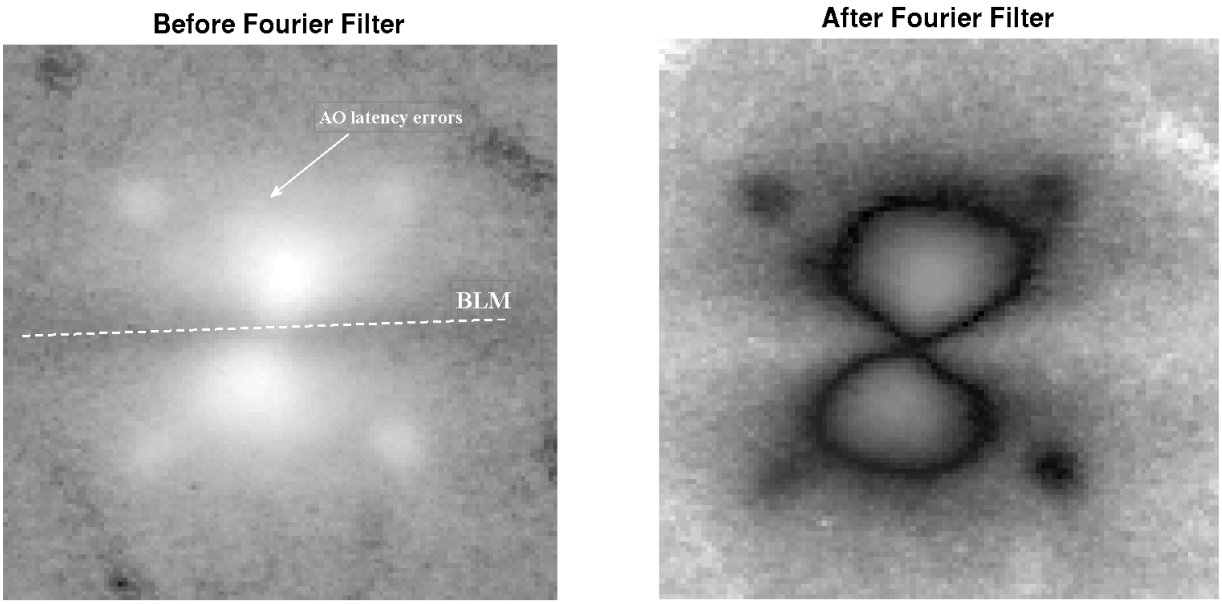


Figure 6-19. Fully processed coronagraphic images of ET-1.

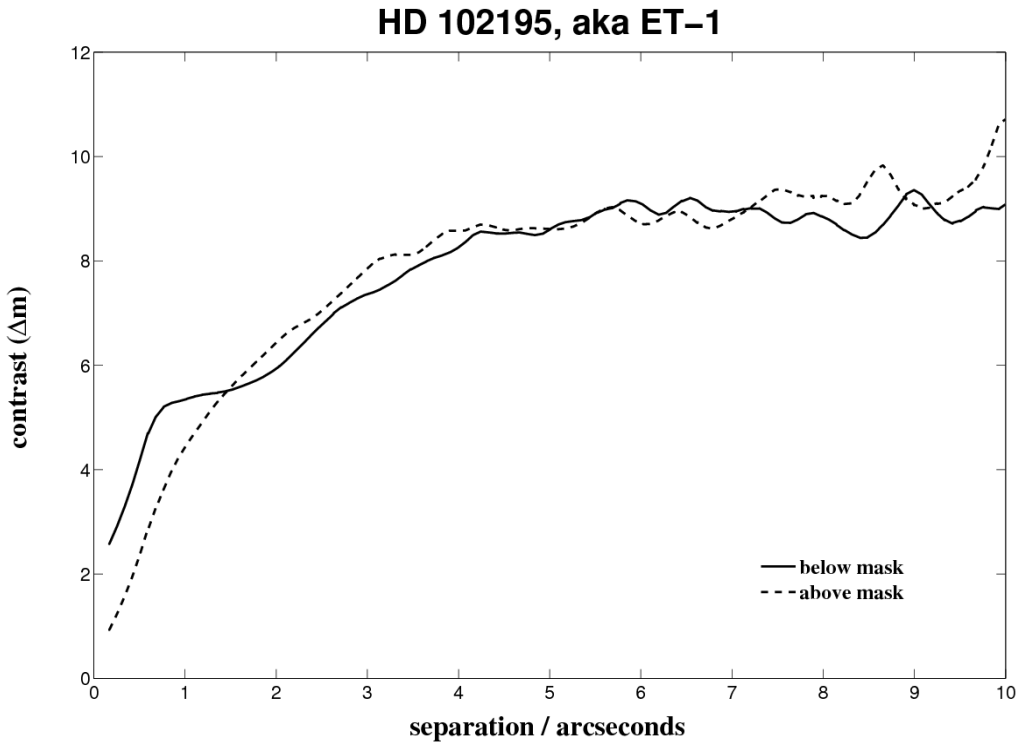


Figure 6-20. ET-1 coronagraph sensitivity above and below mask in magnitudes.

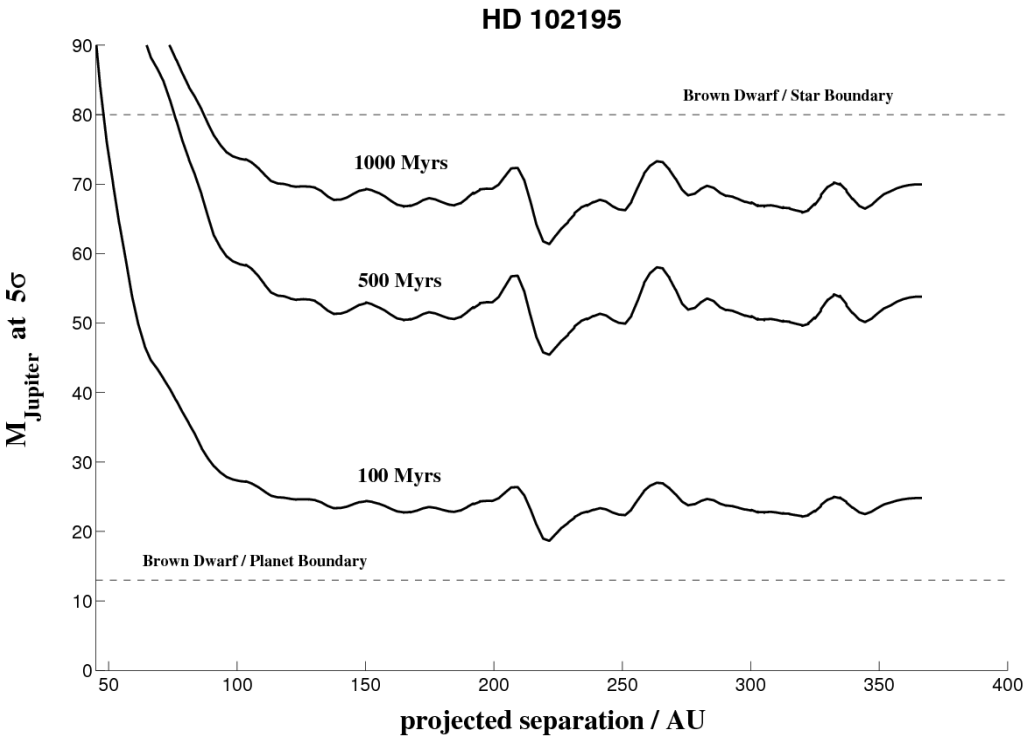


Figure 6-21. ET-1 coronagraph sensitivity in Jupiter masses as a function of age.

# CHAPTER 7
# MINI-PILOT-SURVEY FOR LOW-MASS CIRCUMBINARY COMPANIONS

## 7.1 Motivation

Binaries are a natural result of the star formation process and constitute a substantial fraction, approximately 50%, of all nearby stellar systems (Tokovinin 2004; Duquennoy & Mayor 1991). To date, however, they have been quite purposefully avoided by high-contrast imaging instruments due to an inability to suppress the light from both stars simultaneously. Depending on the separation, nearby stellar companions will either: (i) add unnecessary pointing errors, or (ii) completely overwhelm a portion of the final image. The cartoon in Fig. 7-1 depicts the situation for a ground-based telescope with perfect AO and a coronagraph. Resolving the stellar pair results in significant contrast degradation and dramatically reduces the prospects for discovering faint tertiary companions.

Such configurations occur frequently at near-IR wavelengths with large aperture telescopes. For example, there exists a distinct peak in the orbital period distribution of binary stars with G-type primaries at $\approx 10^{4.8}$ days (Duquennoy & Mayor 1991). This number corresponds to an angular spacing of 0.5" on the sky if we take 75 pcs as a characteristic distance to targets in the solar neighborhood. The spatial resolution of a diffraction-limited 5m telescope at 2.0 microns is $\approx$ 0.1". Thus, *the majority of nearby intermediate-spectral-type binary stars are separated by several diffraction widths.*

To circumvent this problem, a linear occulting mask, which has an intensity transmission that depends on only one Cartesian coordinate, may be used. Since there are no pointing penalties down the long axis of the mask, simultaneous alignment to each stellar component can provide high-contrast images of the circumbinary environment, and faint off-axis sources may be detected at the IWA. For example, the 'x' in Fig. 7-1 indicates the potential location of a companion executing a p-type orbit around a binary star system that has a large inclination relative to the plane of the sky.

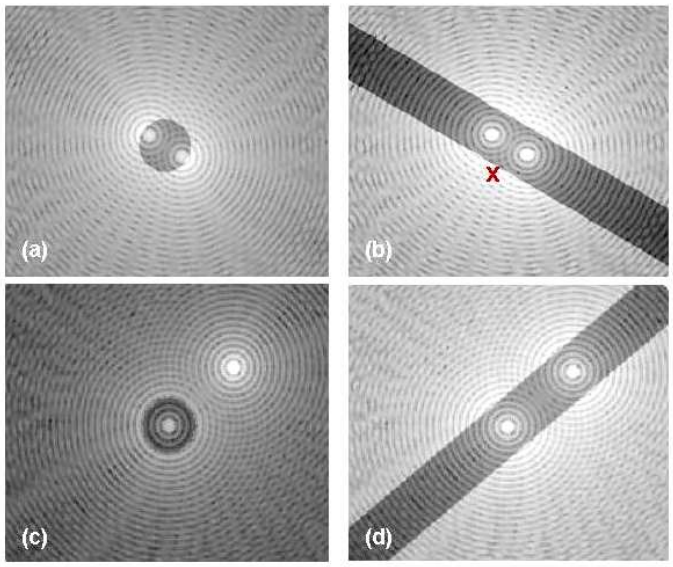


Figure 7-1. Qualitative simulation images comparing circular to linear masks. (a) Binary stars separated by several $\lambda/D$. The pointing errors are significant. (b) A linear mask aligned to both stars simultaneously. (c) Binary stars separated by many $\lambda/D$. The search-space is severely limited. (d) A linear mask can accommodate any such geometry. These images were generated using perfect wavefronts, equally luminous stars, hard-edge masks with high transmission (0.05), and no Lyot stop. Intensity is shown on a logarithmic scale.

Numerical simulations have shown that companions are stable in such configurations over a wide range of separations, mass ratios, and orbital eccentricities (Holman & Wiegert 1999). Moreover, recent Spitzer observations have detected several circumbinary debris disks (Trilling et al. 2007), lending credence to potential low-mass companion formation in these dynamically more complex environments, and ≈20% of short period planets orbit a single member of a binary system (Mugrauer et al. 2007). Given this information, it is hardly justifiable to make conclusions regarding the frequency of substellar companions without considering binary stars.

In addition to searching a new parameter space, other poignant reasons for targeting binaries are:

- RV measurements have revealed a paucity of brown-dwarfs orbiting within several AU of single stars (Marcy & Butler 2000). Subsequent imaging surveys show that this so-called "brown-dwarf desert" extends as far as ∼1000 AU (McCarthy & Zuckerman 2004; Carson et al. 2006). The existence of a similar desert with binary

stars remains open question. The current paradigm of 'environment-dependent' star formation (Duchêne et al. 2007) predicts that large-separation brown-dwarfs should be slightly more common around binaries than single stars, based solely on arguments of binding-energy. Such observations can test this prediction.

- Direct detections made in a variety of settings can help to break the brown-dwarf mass/age degeneracy for a given spectral type.
- The existence of a tertiary companion constrains a system's orbital history.

Based on these scientific justifications, we were awarded on-sky time at Palomar to conduct the first high-contrast imaging observations of visual binary stars using the coronagraphic masks from §6. The remainder of this chapter describes target selection criterion and results from our "mini-pilot-survey".

## 7.2 Target Selection

The following constraints were used for selecting viable binary targets:

- primary with V< 9 for AO locking
- secondary with V< 12 for mask alignment
- DEC $> -5^o$
- $d < 70$ pcs
- angular separation, $50 < \theta$ mas $< 1800$
- accessible position angles

A distance cut is included to maintain a close physical IWA and remove intrinsically bright stars that meet the apparent magnitude criterion. The angular separation between stars, $\theta$, should be large enough that an 8-10m telescope resolves the binary, but small enough that circumbinary orbits in the search area are reasonably stable. [Notice that we could use the small aperture to our advantage again by targeting stars that we do *not* resolve ($50 \lesssim \theta$ mas $\lesssim 300$) but those that a large telescope would – specifically, situation (a) in Fig. 7-1. In this case, a circular mask is ideal.]

The most restrictive criterion is the position angle. The slit-wheel range of motion within the PHARO FOV, with the relay optics in place, is only $\pm 7.5^o$. If we include

the degeneracies in binary star position angles ($180^o = 360^o$, ... etc.) and allow for $90^o$ rotations of the Cass-cage, we can access $60^o/360^o$=1/6 of all random orbital position angles. This implies that not all targets can be selected by youth, especially since we require the orbit in order to forecast the position angle and angular separation for the observing run dates. Selection is further complicated by the fact that we have to recalibrate the Cass-cage ring angle each time the relay optics are installed, as was mentioned in §6.4.2. In other words, we do not know with certainty whether a particular binary is observable until we go on-sky(!)

In total, 690 targets ($0 < \mathrm{RA} < 24$ hrs) were selected from the Sixth Catalog of Orbits of Visual Binary Stars (Mason et al. 2002), Scardia et al. (2008), Makarov (2003), Zuckerman & Song (2004), López-Santiago et al. (2006), and several young unpublished targets provided by Mari-Cruz Galvez-Ortiz. Of these stars, 115 were purportedly younger than 500 Myrs and satisfied the first 5 criterion listed above, but only 7/115 had well-determined orbits. Given the 1/12 probability of accessing their position angles in a given Cass-cage orientation (and poor weather), we managed to observe only 1 young binary star system. Nevertheless, we were able to generate sensitivities to brown dwarfs for 4/5 of the other systems we did observe even though they were older.

## 7.3 Tertiary Companion Sensitivity

It is reasonable to expect the sensitivity on two stars to be somewhat worse than twice that of a single star due to non-common-path errors and isoplanatism. These effects are, however, small for binaries with $\approx 1$" separations. Another interesting feature is that companions can be detected in between the stars so long as they are located outside of the mask IWA (Fig. 7-1b). The amount of scattered light in this region may be less than that very close to one of the sources.

Contrast levels will be different for each star, since, in general, they differ in brightness, but the mass-sensitivity must be the same: "If there were a brown-dwarf tertiary located right here, would I see it?". In the following, we report contrast in a

$\lambda_{max}/D_{tel}$-wide strip above and below the mask relative to the brighter of the two stars and starting from their photo-center. The mass-sensitivity curves show an average of the contrast curves above and below the mask, as was done in §6.

Many of the individual K-band apparent magnitudes are not available since 2MASS is seeing limited. It is, however, possible to use the combined flux recorded by 2MASS with our diffraction-limited calibration images to obtain the apparent K-band magnitudes:

$$K_1 = K_{2\mathrm{MASS}} + 5/2 \log(1 + F_2/F_1) \quad (7\text{–}1)$$

$$K_2 = K_{2\mathrm{MASS}} + 5/2 \log(1 + F_1/F_2) \quad (7\text{–}2)$$

where $K_{2\mathrm{MASS}}$ is the combined (unresolved) apparent K-band magnitude measured by 2MASS (Skrutskie et al. 2006) and $F_1$ and $F_2$ are the fluxes measured from our calibration images in arbitrary units. Apparent magnitudes are then converted to absolute magnitudes in order to calculate contrast in Jupiter-masses using the Girardi et al. (2002) and Baraffe et al. (2003) atmospheric models, which are consistent with one another near the brown-dwarf – stellar boundary for ages greater than 50 Myrs.

### 7.3.1 HIP 88637

We observed the binary star system HIP 88637 on 2008-5-26 (UT) using the BLM. HIP 88637 is a kinematic member of the Pleiades moving group and has an age < 150 Myrs (Makarov 2003). Table 7-1 lists its physical parameters and relevant observational information. Seeing measurements usually recorded by the Palomar MASS-DIMM system (Thomsen et al. 2007) are not available for this run due to inconsistent weather conditions. We did not measure the seeing directly on account of these time constraints.

Table 7-1. Physical parameters and observational information for HIP 88637.

| | | | |
|---|---|---|---|
| SAO = 85723 | distance = 37.7 pcs | age < 150 Myrs | airmass = 1.05 |
| RA = 18 05 49.7 | sep / PA$^a$ = 0.49" / 91.4$^o$ | $\Delta t_{source}$ = 991 s | seeing = unav. |
| DEC = +21 26 45.2 | Vmag = 7.6 / 8.4 | $\Delta t_{sky}$ = 991 s | Strehl = 89.8 ± 0.9 |

$^a$Position angles are measured in degrees East from North.

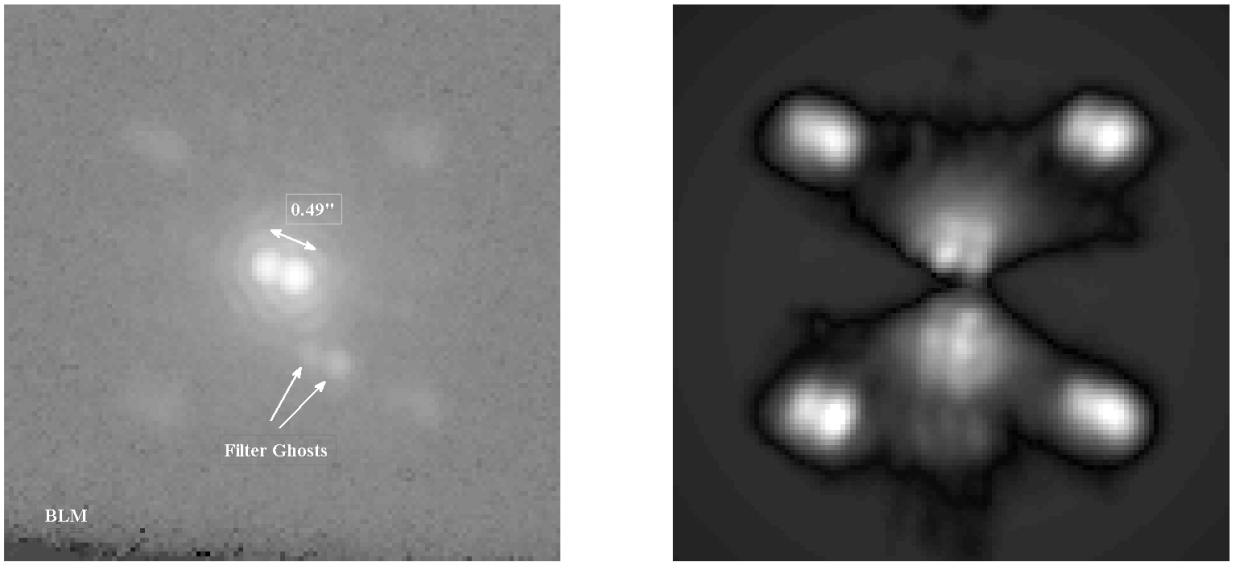


Figure 7-2. Calibration and high-pass Fourier-filtered coronagraph images of HIP 88637.

Results are shown in Figs. 7-2, 7-3, and 7-4. Reflections from a neutral-density filter are visible for each star in the calibration image, but not seen in the coronagraph image since the filter is removed once the mask is aligned. There are now eight waffle-mode peaks. The contrast is comparable to levels achieved around single stars in §6.4 (see

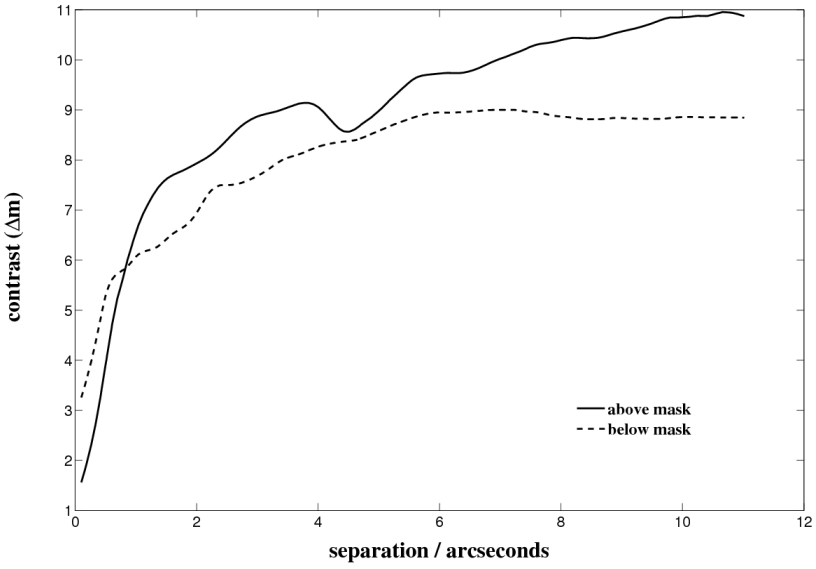


Figure 7-3. HIP 88637 coronagraph sensitivity in magnitudes. The asymmetry in flux above and below the mask is a result of mechanical flexure.

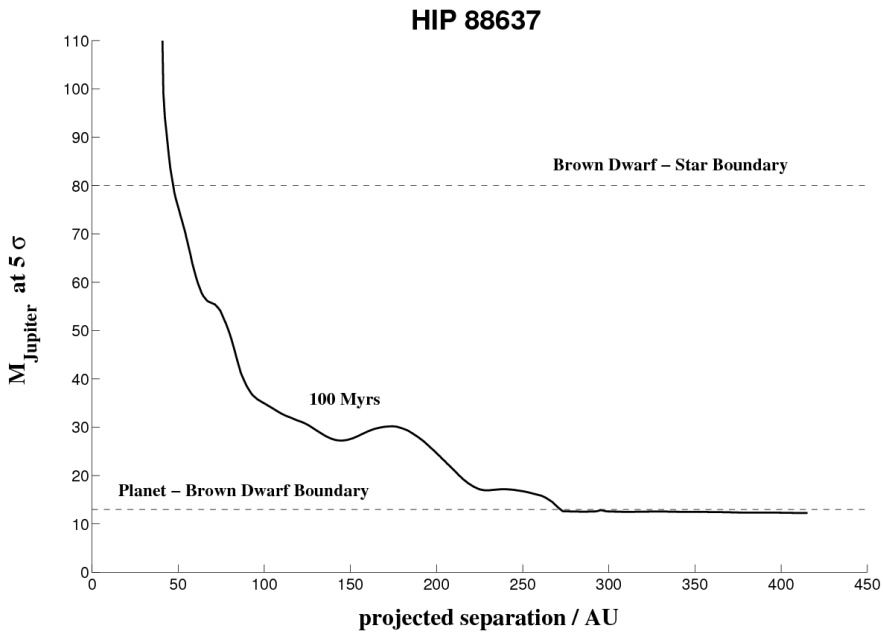


Figure 7-4. HIP 88637 coronagraph sensitivity in Jupiter masses for an age of 100 Myrs.

below). We were able to generate sensitivities to brown-dwarfs and massive extrasolar planets orbiting exterior to 50 AU and 275 AU respectively at the $5\sigma$ level. No tertiary companions were detected.

### 7.3.2 HIP 82510

The direct imaging measurements made on the previous target, HIP 88637, were very sensitive due to its young age but also an improvement to the hardware. This next data set, HIP 82510, shows how the sensitivity was enhanced by switching to a Lyot stop, the medium cross (Hayward et al. 2001), that suppresses the non-common-path errors shown in Fig. 6-9. It also has higher throughput and spatial resolution, although the design in §6.2.2, which was used for all observations in April 2007, should work best in the ideal case.

Table 7-2. Physical parameters and observational information for HIP 82510 in April 2007.

| | | | |
|---|---|---|---|
| SAO = 84655 | distance = 56.9 pcs | age = unknown | airmass = 1.02 |
| RA = 16 51 50.1 | sep / PA = 1.36" / 102.5$^o$ | $\Delta t_{source}$ = 297 s | seeing = 0.9" |
| DEC = +28 39 59.0 | Vmag = 7.0 / 8.5 | $\Delta t_{sky}$ = 149 s | Strehl = 85.9 $\pm$ 0.3% |

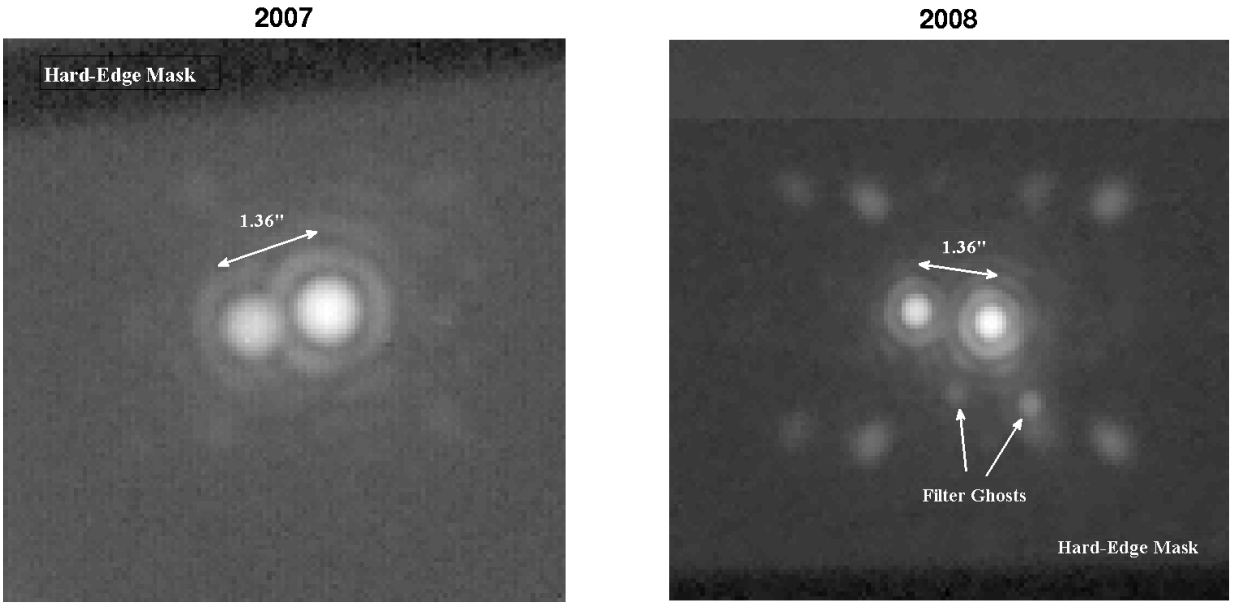


Figure 7-5. Calibration images of HIP 82510 in April 2007 and May 2008. Spatial resolution and throughput are improved on account of a wider Lyot stop.

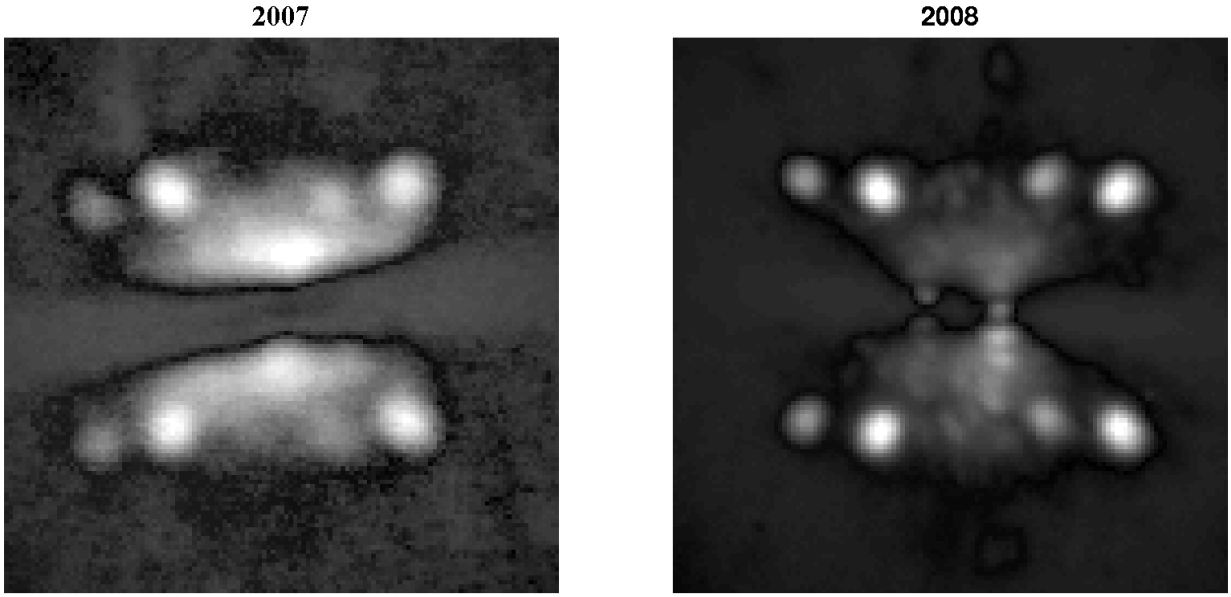


Figure 7-6. Coronagraph images of HIP 82510 in April 2007 and May 2008.

We observed the binary star system HIP 82510 on 2007-4-29 and 2008-5-26 (UT) using the hard-edge mask and BLM respectively.. Table 7-2 displays its physical

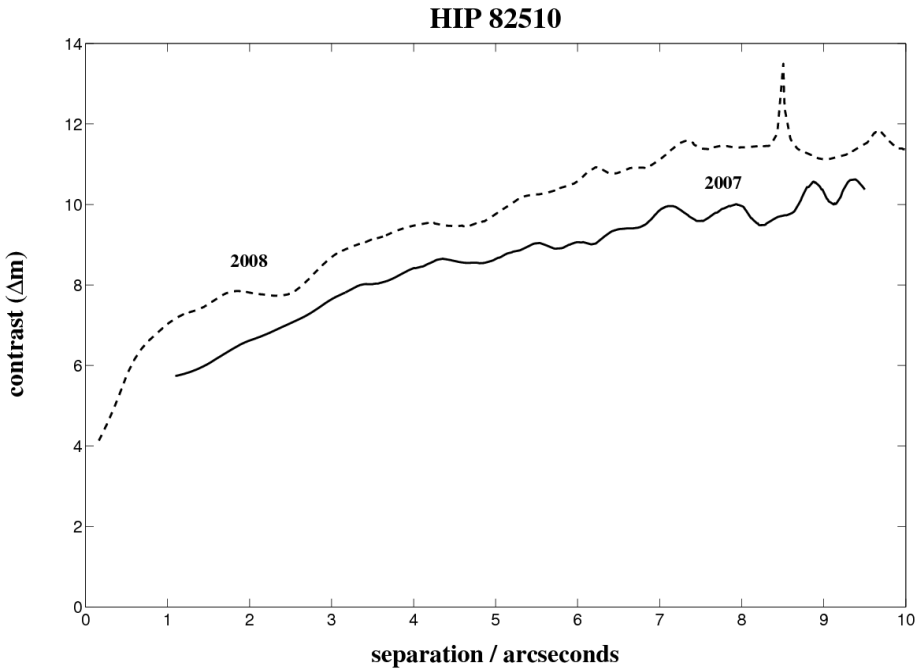


Figure 7-7. HIP 82510 coronagraph sensitivity in magnitudes in 2007 and 2008.

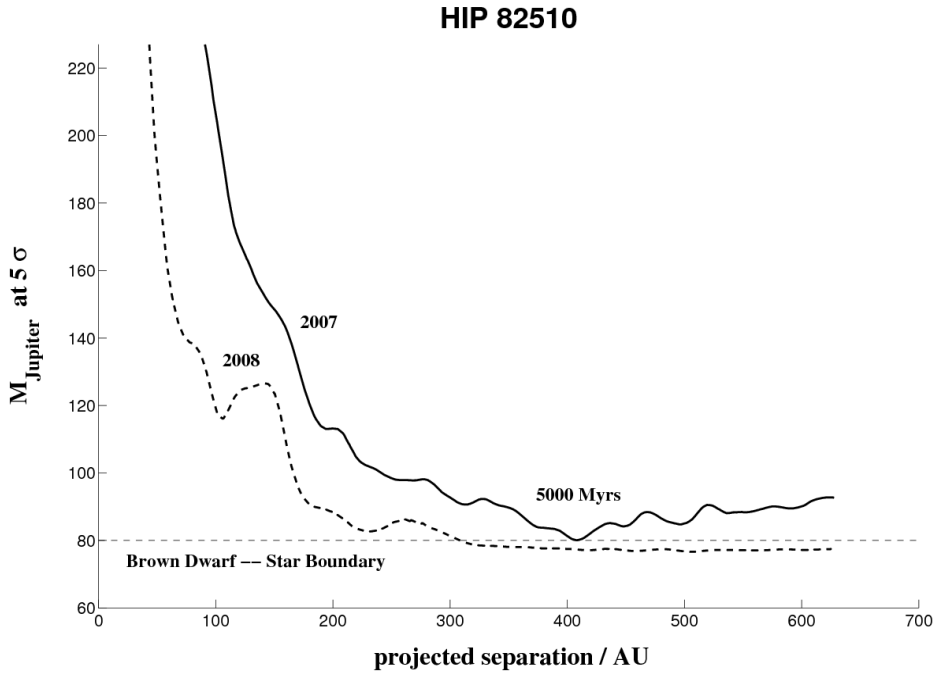


Figure 7-8. HIP 82510 coronagraph sensitivity in Jupiter masses in 2007 and 2008. Although different masks were used, the enhanced performance is the result of switching to a Lyot stop better suited to handle non-common-path errors.

parameters and relevant observational information for the first run. On the second run, the airmass and Strehl ratio were 1.01 and $84.0 \pm 1.3\%$ respectively.

The position angle relative to PHARO changed by $11.4^o$ in between runs, but only $0.5^o$ is due to orbital motion (PA=$103^o$ in May 2008), implying that the Cass-ring angle changed by $10.9^o$. This is a significant amount and affects target selection since the slit-wheel range of motion is only $15^o$ (§7.2). The effect will be accounted for in the future by compiling lists of targets that span the range of position angles surrounding the Cass-ring "sweet-spots" (i.e. where an unobscured quadrant of the telescope aperture can be selected) or by building masks that are not parallel to one another (§8).

The difference in relative position angle made it mandatory to use different masks for the two runs. Although the BLM has the potential to outperform the hard-edge mask (§4), the improved sensitivity shown in Figs. 7-7 and 7-8 is a result of blocking non-common-path errors and passing more off-axis light with the medium cross Lyot stop. The scattered light floor drops just enough to detect massive brown-dwarfs. We note that the K-band flux ratio, $F_2/F_1$, was measured to be 0.319 in 2007 and 0.318 in 2008.

### 7.3.3 HIP 88964

We observed the star HIP 88964 on 2008-5-26 (UT) using the BLM. Table 7-3 displays its physical parameters and relevant observational information. Results are shown in Figs. 7-9, 7-10, and 7-11. The DM operated at 500 HZ, which is faster than most of the observations presented here using the relay optics. Frequencies approaching 2 kHz are ideal for minimizing AO lag-time errors.

Table 7-3. Physical parameters and observational information for HIP 88964.

| | | | |
|---|---|---|---|
| SAO = 123187 | distance = 50.1 pcs | age = unknown | airmass = 1.18 |
| RA = 18 09 33.9 | sep / PA = 0.62" / $288.2^o$ | $\Delta t_{source}$ = 977 s | seeing = unav. |
| DEC = +03 59 35.8 | Vmag = 6.1 / 7.4 | $\Delta t_{sky}$ = 489 s | Strehl = $88.8 \pm 1.5\%$ |

Mass-sensitivity depends strongly on age only below the brown dwarf–star boundary ($\lesssim 80 M_{Jupiter}$). This is the result of cooling since substellar bodies are unable to sustain

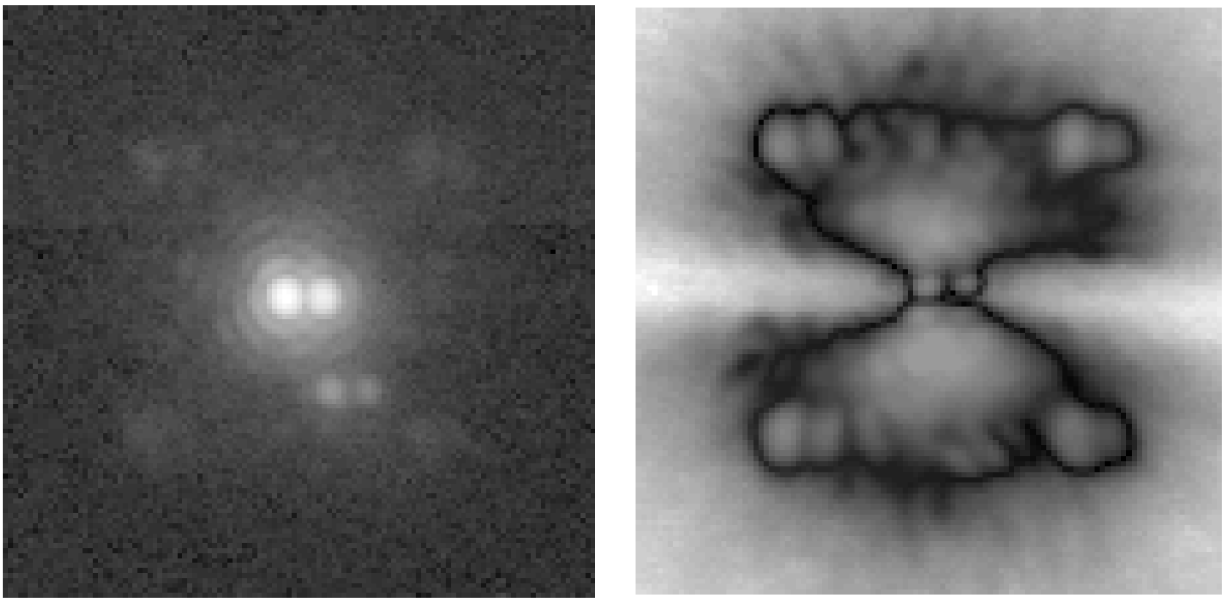

Figure 7-9. Calibration and coronagraph images of HIP 88964.

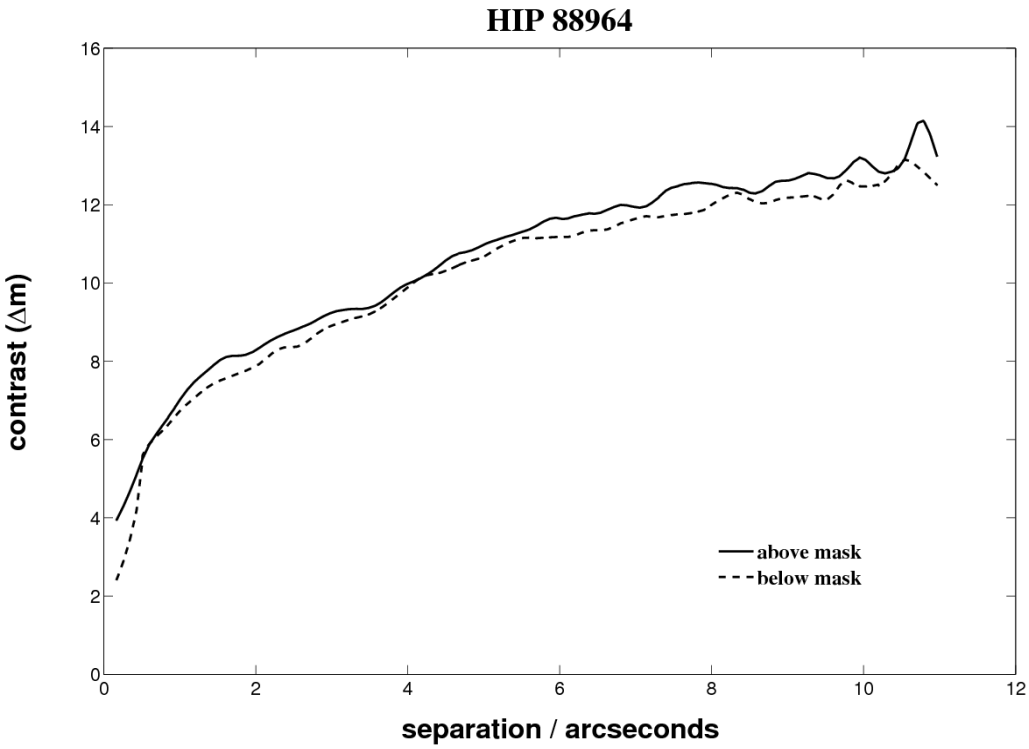


Figure 7-10. HIP 88964 coronagraph sensitivity in magnitudes.

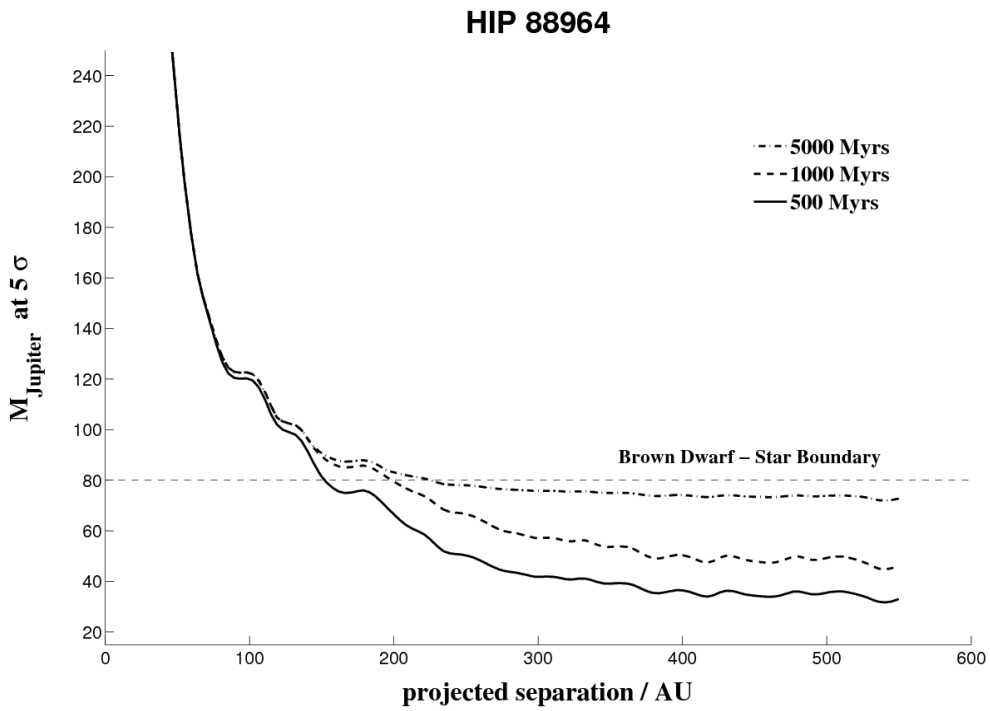


Figure 7-11. HIP 88964 coronagraph sensitivity in Jupiter masses for various ages.

hydrogen fusion reactions. The contrast reaches $\approx 40 M_{Jupiter}$ at an age of 500 Myrs. No companions were detected.

### 7.3.4 HIP 66458

We observed the binary star HIP 66458 (Table 7-4) on 2008-5-26 (UT) using the BLM. Impending clouds prevented acquisition of a calibration image. Nevertheless, we were able to calculate the K-band magnitudes via Equ. 7–2 from the waffle-mode peaks(!)

Several point-sources are visible above and below the mask (Fig. 7-12). Symmetries in the image suggest the presence of long-lived speckles (so-called "super-speckles"), which are the result of quasi-static errors, but not all of the sources have a symmetric or anti-symmetric partner, which might be the result of slightly different mask alignments for each star. Follow-up observations are required to discriminate speckles from companions. The evidence in this case is, however, likely too weak to warrant a proposal.

Table 7-4. Physical parameters and observational information for HIP 66458.

| | | | |
|---|---|---|---|
| SAO = 63648 | distance = 58.8 pcs | age = unknown | airmass = 1.05 |
| RA = 13 37 27.6 | sep / PA = 1.74" / 96.9$^o$ | $\Delta t_{source}$ = 942 s | seeing = unav. |
| DEC = +36 17 41.6 | Vmag = 5.0 / 7.1 | $\Delta t_{sky}$ = 248 s | Strehl = unav. |

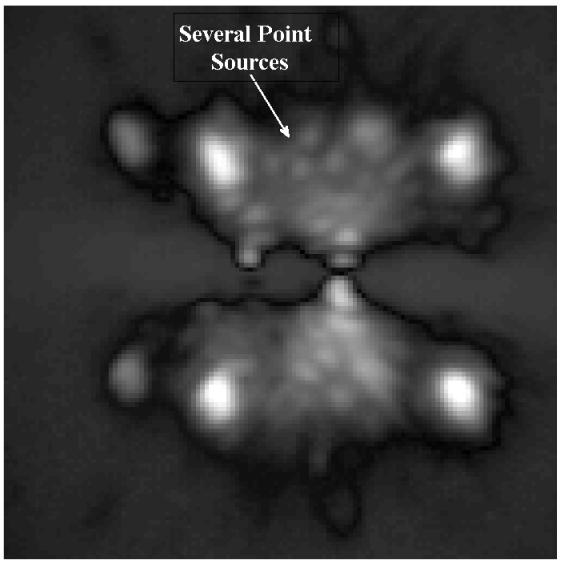


Figure 7-12. Coronagraph image of HIP 66458.

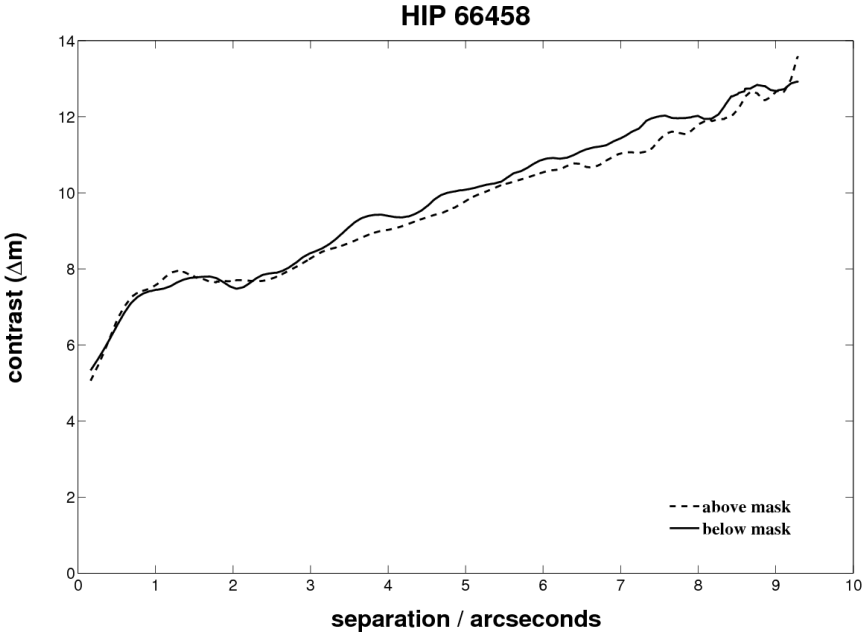


Figure 7-13. HIP 66458 coronagraph sensitivity in magnitudes.

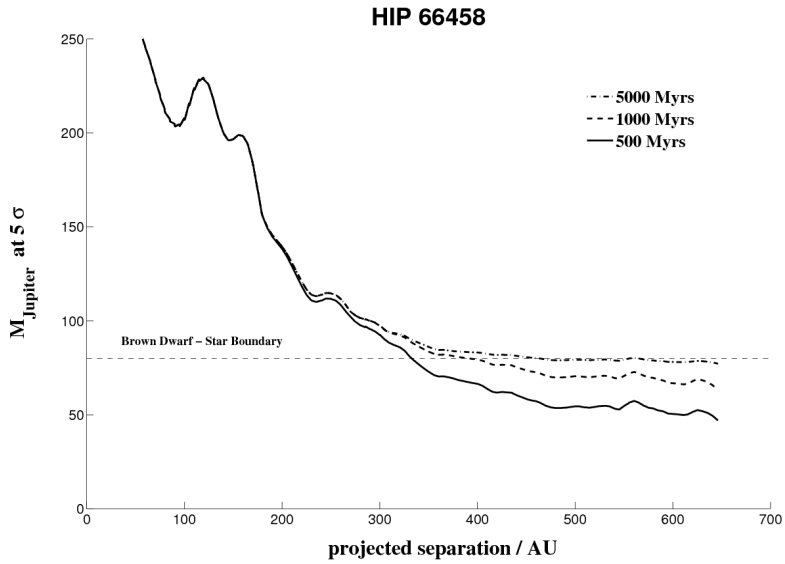


Figure 7-14. HIP 66458 coronagraph sensitivity in Jupiter masses for various ages.

### 7.3.5 HIP 76952

We observed HIP 76952 (Table 7-5) on 2008-5-26 (UT) using the hard-edge mask. The DM was operating at 500 Hz. Results are shown in Figs. 7-15, 7-16, and 7-17. Sensitivities sufficient to detect massive brown dwarfs were generated at projected separations greater than 250 AU. No nearby point sources were detected.

Table 7-5. Physical parameters and observational information for HIP 76952.

| | | | |
|---|---|---|---|
| SAO = 83958 | distance = 44.5 pcs | age = unknown | airmass = 1.01 |
| RA = 15 42 44.6 | sep / PA = 0.72" / 112.4$^o$ | $\Delta t_{source}$ = 439 s | seeing = unav. |
| DEC = +26 17 44.3 | Vmag = 4.1 / 5.6 | $\Delta t_{sky}$ = 439 s | Strehl = 92.3 $\pm$ 1.7% |

### 7.3.6 HIP 82898

We observed HIP 82898 (Table 7-6) on 2007-4-29 (UT) using the BLM. The DM was operating at 500 Hz. Results are shown in Figs. 7-18, 7-19, and 7-20. We were unable to generate sensitivities to brown dwarfs independent of age. No tertiaries were detected.

Table 7-6. Physical parameters and observational information for HIP 82898.

| | | | |
|---|---|---|---|
| SAO = 17285 | distance = 67.1 pcs | age = unknown | airmass = 1.18 |
| RA = 16 56 25.3 | sep / PA = 1.29" / 67.7$^o$ | $\Delta t_{source}$ = 142 s | seeing = 0.9" |
| DEC = +65 02 20.8 | Vmag = 7.1 / 7.4 | $\Delta t_{sky}$ = 71 s | Strehl = 89.5 $\pm$ 0.3% |

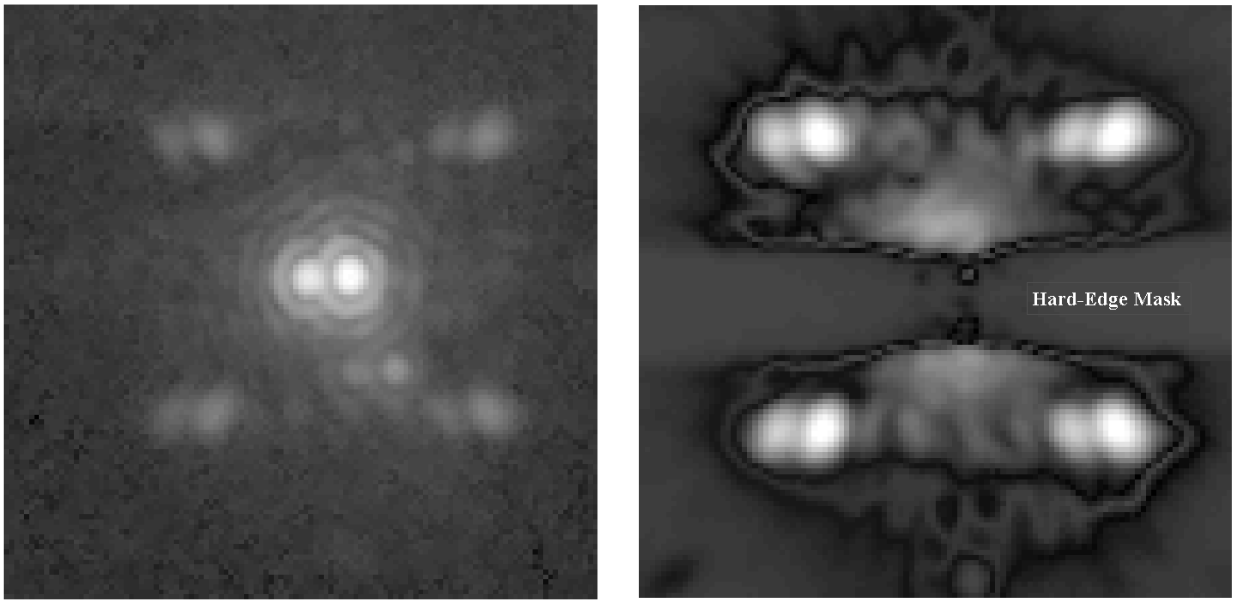


Figure 7-15. Calibration and coronagraph images of HIP 76952.

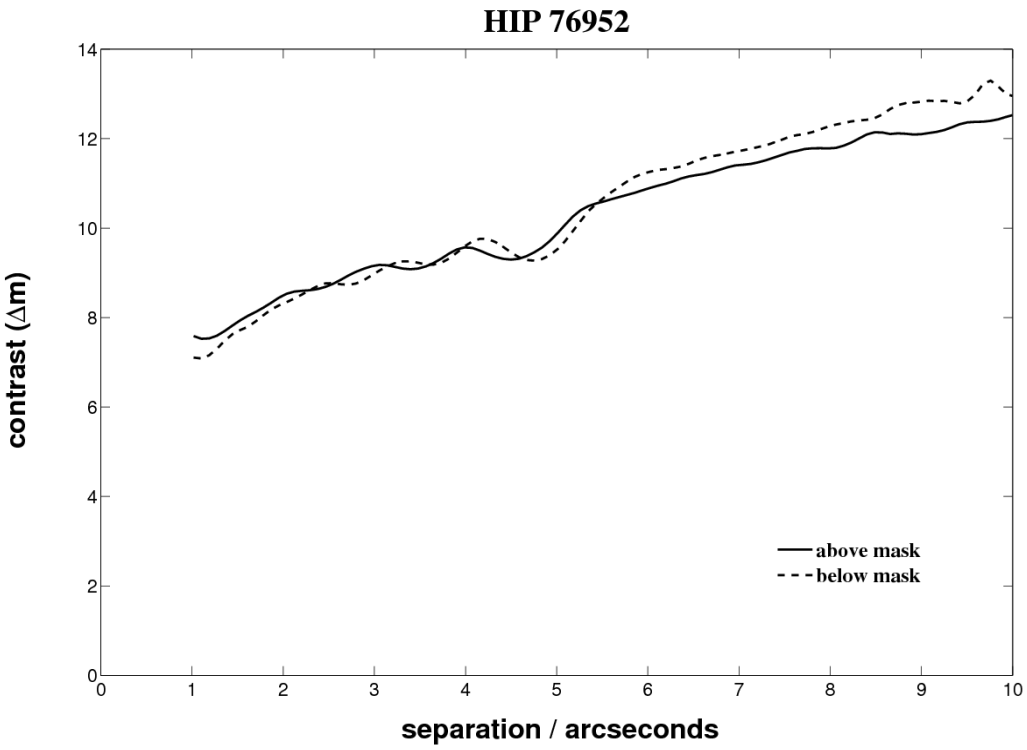


Figure 7-16. HIP 76952 coronagraph sensitivity in magnitudes.

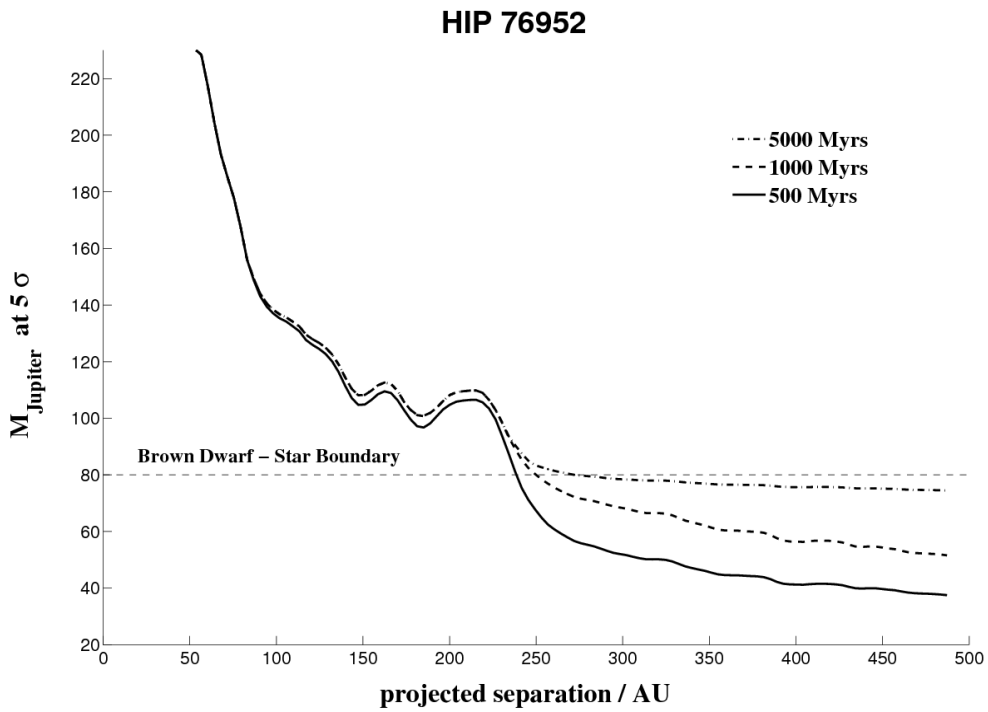


Figure 7-17. HIP 76952 coronagraph sensitivity in Jupiter masses for various ages.

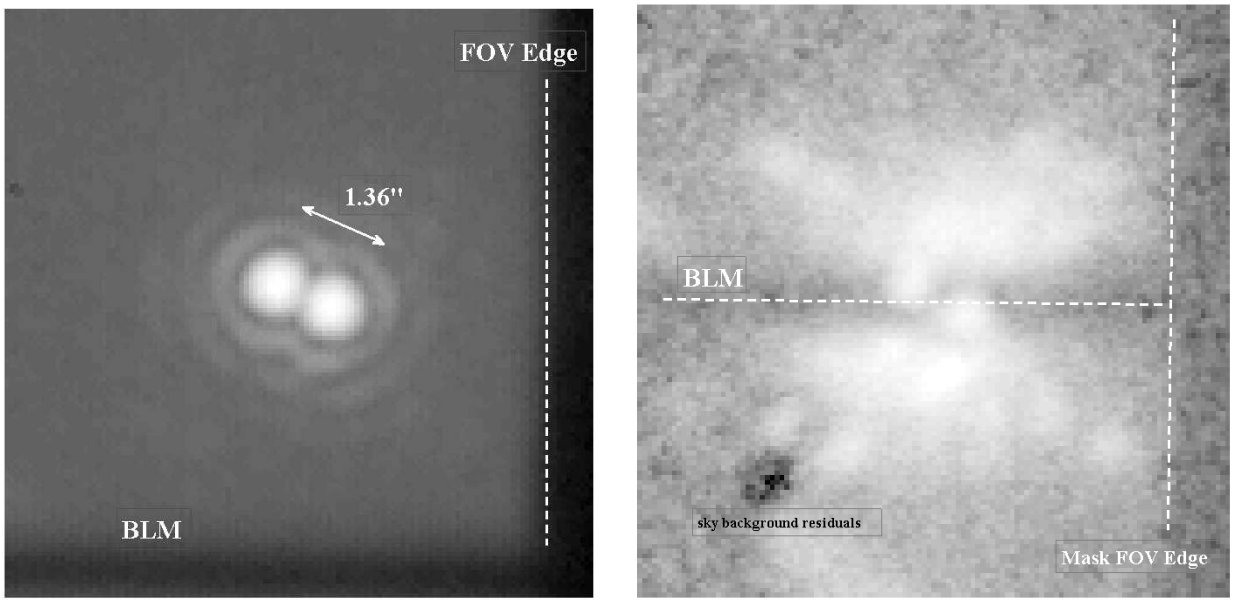


Figure 7-18. Calibration and unfiltered coronagraphic images of HIP 82898.

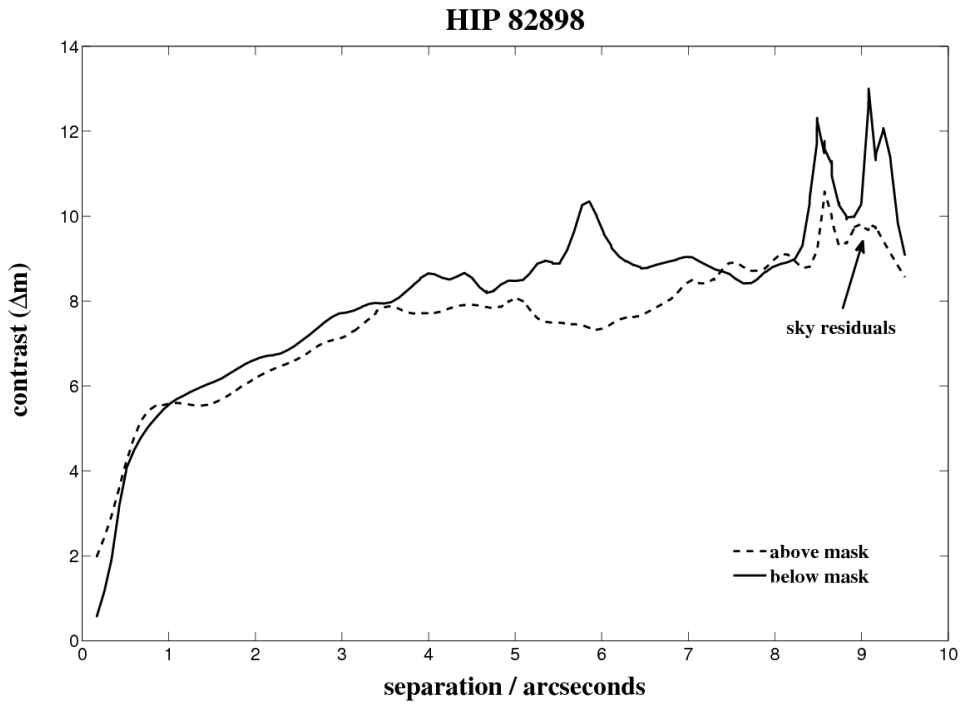


Figure 7-19. HIP 82898 coronagraph sensitivity above and below mask in magnitudes.

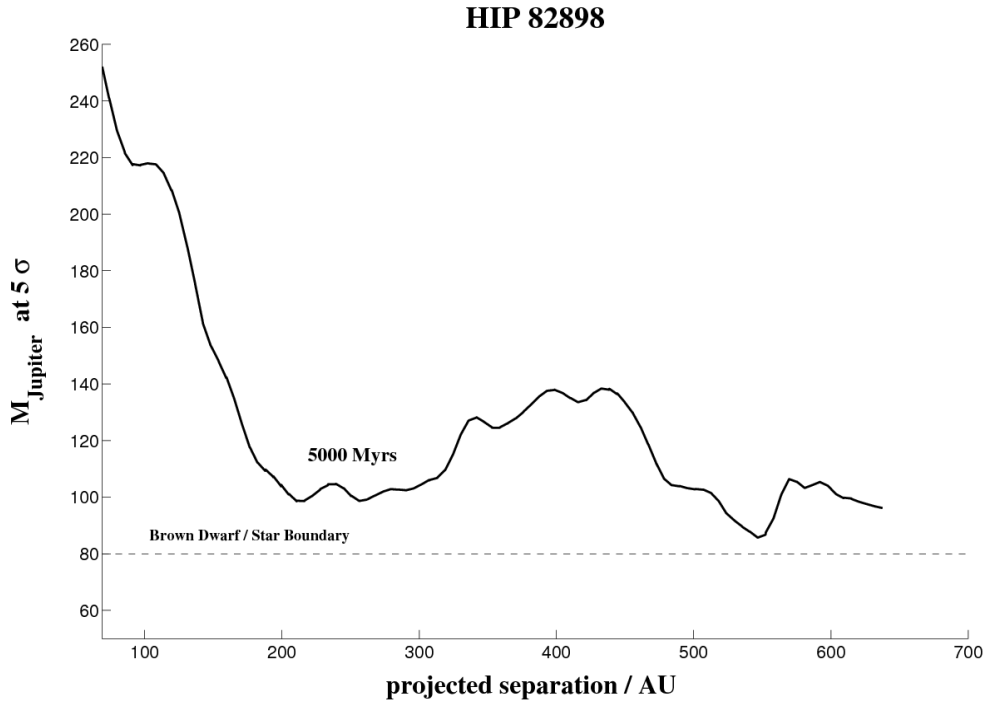


Figure 7-20. HIP 82898 coronagraph sensitivity in Jupiter masses for an age of 5 Gyrs.

## 7.4 Discussion

The observational results reported in the last two chapters (3 single stars and 6 double stars) were obtained with only 7 hrs of on-sky time. We were awarded 6.5 nights but most was lost to southern California fires, which burned down power-lines leading to the observatory in October 2007, and high humidity, including snow-fall, in May 2008. It should be possible to target $\approx$ 40 more binary systems and several bright young single stars with the 3 more nights we were awarded in November 2008 to recoup lost time.

In any case, we have learned a lot. The BLM clearly works and we have identified the effects that can limit sensitivity. The flex-camera will soon operate smoothly and correct for the drifts seen with HIP 83389 and HIP 88637. We now have a handle on the preferred Cass-cage ring angles and how they translate to on-sky measurements relative to our mask within PHARO. Combining this information with more on-sky time will permit observations that better favor young systems. Moreover, we expect significant gains in sensitivity (see §8) by removing the non-common-path errors shown in Fig. 6-9. Once enough sources are observed and the above hardware adjustments are made, it will be possible to make apple-to-apple comparisons of the hard-edge mask versus the BLM and to the full aperture using data obtained previously by Joe Carson.

We anticipate an experiment in the near-term where a very bright source, like Vega, is imaged onto a quadrant of the array. This will reduce the read-time and allow for better speckle tracking. We also plan to fully characterize both the hard-edge mask and BLM by moving the white light source down their long axis (§6.3). If non-common-path errors associated with visual binary stars, which land on different locations of the mask (see §3.2.3), can be neglected, or at least minimized using an optimal DM setting, it may be possible to perform high-fidelity PSF subtraction (§3.2.5), by modeling the speckle pattern.

A sensitive and statistically significant survey of visual binary stars will place new constraints on the population of substellar tertiary companions, which is important for the

reasons discussed in §7.1. It is interesting to consider how the search area of a linear mask affects the results of a Monte Carlo simulation where artificial brown dwarfs are inserted. Of course, a few detections would be most exciting.

I am also naturally curious about circumbinary planets. If they are more massive (on average) compared to planets orbiting single stars, due to a surplus of material from which they can form, or if their orbits are more eccentric (on average), due to stochastic processes, they will be easier to image!

# CHAPTER 8
# AFTERWORD: PROJECT CONCLUSIONS & LONG-TERM PROSPECTS

This section reiterates the main conclusions from Chapters 2-7 and briefly describes the project's likely path over the next few years.

In summary, we find that:

- Eighth-order BLMs are useful from the ground and space. They control diffraction while helping to attenuate residual low spatial-frequency errors and also guard against light leakage due to the finite size of stars.
- Eighth-order BLMs can be built using nanofabrication techniques and their performance aligns well with theoretical predictions.
- There are certain guidelines, or "rules of thumb", that govern the selection of image-plane occulters from the ground.
- Preliminary tests of the first BLM operating in concert with the first extreme AO system generate instantaneous contrast levels sufficient to detect substellar companions orbiting single and double stars over a relatively wide range of ages. Sensitivity is limited by wavefront control.

The basic premise of this work is straightforward: *contrast* is most important in the game of high-contrast imaging, especially with the field in its current state: one or maybe two images of extrasolar planets thus far that did not even require a coronagraph to detect(!) Simultaneous differential imaging techniques have generated the deepest sensitivities to date, but they can always be applied *after* the instrument scattered light has been explicitly removed using hardware. Since star-planet separations span several orders of magnitude (0.018 AU -275 AU, HD 41004 Bb and AB Pic respectively), there should be an abundant number of companions with $> 0.5$" separations. For example, Epsilon Eridani b will reach its greatest elongation of 1.6" in the year 2010 (Benedict et al. 2006). It is thus quite reasonable to sacrifice spatial resolution to help overcome fundamentally challenging problems, such as the exquisite positioning of numerous, closely-spaced actuators to correct for the atmosphere while removing instrument scattered light. Relay optics can address these issues several years before the next generation of AO systems

come on-line. I plan to use them well into my first post-doc appointment which permits the continuation of work along these lines.

This project has a lot of potential and there are several obvious next steps to take:

- Remove the waffle-mode peaks. They occupy valuable search area. This can be accomplished with software by modifying the wavefront reconstructor.
- Compensate for non-common-path errors using the techniques in §3 and/or by poking individual actuators and looking at the result in the Lyot pupil plane.
- Build a BLM for the J-band where young planets are brighter, the IWA improves by 42%, and the sky background is significantly fainter.
- Couple the relay optics with the PALM-3k AO system. The PALM-3k by itself will "only" generate Strehl ratios of $\approx$ 80% over the full aperture of the Hale 200-inch (Dekany et al. 2007).

Figure 8-1 shows predictions for bright single stars using relay optics with and without compensation for non-common-path errors and then with the upgrade to PALM-3k. Instantaneous contrast levels of order $10^{-6}$ are possible. An integral-field-unit should be capable of discriminating between speckles and companions using color information to improve the effective sensitivity by another order of magnitude.

There may be insufficient flux for all 64x64 wavefront sensor subapertures using the relay optics, but, as we have shown in §3.2.3, it is not necessary to correct near the outer-most edges of the dark-hole. This sacrifice in search area permits use of less subapertures while improving the dark-hole depth. Laser-guide star AO may be another alternative in this situation since the 'cone-effect' associated with illuminating a nearby layer of the atmosphere (i.e., the fact that the laser does not create a perfect point source) is relatively small for a 1.5m telescope.

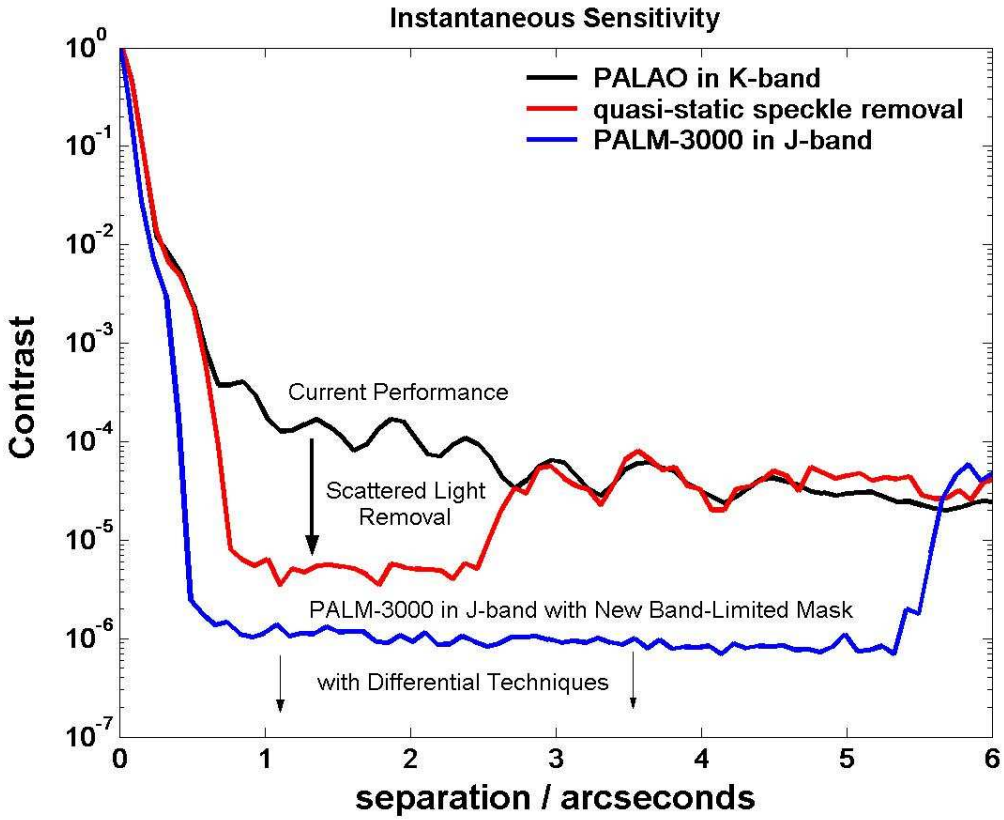


Figure 8-1. Contrast as a function of angular separation for the Hale telescope using relay optics. It is possible to remove (quasi-static) scattered light (created by non-common-path errors) down to the noise floor set by the atmosphere at $\approx 7 \times 10^{-6}$ in the K-band (red curve). These methods may then be applied to teh PALM-3k system in the J-band and with a new BLM (blue curve). The IWA will improve from 880 mas to 510 mas and the contrast will drop to $2 \times 10^{-6}$ and extend to 5400 mas. Sacrifices of the outer search area may drop the instantaneous noise floor even further. The full aperture can probe smaller separations but cannot match the sensitivity. With post-processing techniques, the effective contrast may reach $10^{-7}$. Young massive exoplanets are detectable with this technology.

REFERENCES


Abe, L., Murakami, N., Nishikawa, J., & Tamura, M. 2006, A&A, 451, 363

Absil, O., den Hartog, R., Gondoin, P., Fabry, P., Wilhelm, R., Gitton, P., & Puech, F. 2006, A&A, 448, 787

Aime, C. 2005, A&A, 434, 785

Allende Prieto, C., & Lambert, D. L. 1999, A&A, 352, 555

Balasubramanian, K., Hoppe, D. J., Halverson, P. G., Wilson, D. W., Echternach, P. M., Shi, F., Lowman, A. E., Niessner, A. F., Trauger, J. T., & Shaklan, S. B. 2006, in IAU Colloq. 200: Direct Imaging of Exoplanets: Science & Techniques, ed. C. Aime & F. Vakili, 405

Baraffe, I., Chabrier, G., Barman, T. S., Allard, F., & Hauschildt, P. H. 2003, A&A, 402, 701

Bean, J. L., McArthur, B. E., Benedict, G. F., Harrison, T. E., Bizyaev, D., Nelan, E., & Smith, V. V. 2007, AJ, 134, 749

Béjar, V. J. S., Zapatero Osorio, M. R., Pérez-Garrido, A., Álvarez, C., Martín, E. L., Rebolo, R., Villó-Pérez, I., & Díaz-Sánchez, A. 2008, ApJ, 673, L185

Benedict, G. F., McArthur, B. E., Gatewood, G., Nelan, E., Cochran, W. D., Hatzes, A., Endl, M., Wittenmyer, R., Baliunas, S. L., Walker, G. A. H., Yang, S., Kürster, M., Els, S., & Paulson, D. B. 2006, AJ, 132, 2206

Beuzit, J.-L., Feldt, M., Dohlen, K., Mouillet, D., Puget, P., Antichi, J., Baruffolo, A., Baudoz, P., Berton, A., Boccaletti, A., Carbillet, M., Charton, J., Claudi, R., Downing, M., Feautrier, P., Fedrigo, E., Fusco, T., Gratton, R., Hubin, N., Kasper, M., Langlois, M., Moutou, C., Mugnier, L., Pragt, J., Rabou, P., Saisse, M., Schmid, H. M., Stadler, E., Turrato, M., Udry, S., Waters, R., & Wildi, F. 2006, The Messenger, 125, 29

Biller, B. A., Kasper, M., Close, L. M., Brandner, W., & Kellner, S. 2006, ApJ, 641, L141

Bonfils, X., Mayor, M., Delfosse, X., Forveille, T., Gillon, M., Perrier, C., Udry, S., Bouchy, F., Lovis, C., Pepe, F., Queloz, D., Santos, N. C., & Bertaux, J.-L. 2007, A&A, 474, 293

Bordé, P. J., & Traub, W. A. 2006, ApJ, 638, 488

Born, M., & Wolf, E. 1999, Principles of Optics - 7th expanded ed.

Brunetto, E. T., Dierickx, P., Gilmozzi, R., Le Louarn, M., Koch, F., Noethe, L., Verinaud, C., & Yaitskova, N. 2004, in Presented at the Society of Photo-Optical Instrumentation Engineers (SPIE) Conference, 5382, Second Backaskog Workshop on Extremely Large Telescopes. Edited by Ardeberg, Arne L.; Andersen, Torben. Proceedings of the SPIE, Volume 5382, pp. 159-168 (2004)., ed. A. L. Ardeberg & T. Andersen, 159

Burrows, A., Sudarsky, D., & Hubeny, I. 2004, ApJ, 609, 407

Carson, J. C., Eikenberry, S. S., Brandl, B. R., Wilson, J. C., & Hayward, T. L. 2005, AJ, 130, 1212

Carson, J. C., Eikenberry, S. S., Smith, J. J., & Cordes, J. M. 2006, AJ, 132, 1146

Carson, J. C., Wilson, D. W., & Trauger, J. T. 2005, in Presented at the Society of Photo-Optical Instrumentation Engineers (SPIE) Conference, 5905, Techniques and Instrumentation for Detection of Exoplanets II. Edited by Coulter, Daniel R. Proceedings of the SPIE, Volume 5905, pp. 427-438 (2005)., ed. D. R. Coulter, 427

Cash, W. 2006, Nature, 442, 51

Charbonneau, D., Brown, T. M., Latham, D. W., & Mayor, M. 2000, ApJ, 529, L45

Chauvin, G., Lagrange, A.-M., Dumas, C., Zuckerman, B., Mouillet, D., Song, I., Beuzit, J.-L., & Lowrance, P. 2005a, A&A, 438, L25

Chauvin, G., Lagrange, A.-M., Zuckerman, B., Dumas, C., Mouillet, D., Song, I., Beuzit, J.-L., Lowrance, P., & Bessell, M. S. 2005b, A&A, 438, L29

Clampin, M. 2007, in In the Spirit of Bernard Lyot: The Direct Detection of Planets and Circumstellar Disks in the 21st Century, ed. P. Kalas, 49

Close, L. M., Lenzen, R., Guirado, J. C., Nielsen, E. L., Mamajek, E. E., Brandner, W., Hartung, M., Lidman, C., & Biller, B. 2005, Nature, 433, 286

Crepp, J. R., Carson, J., Serabyn, E., Wallace, K., Ge, J., & Kravchenko, I. 2007, in AAS/Division for Planetary Sciences Meeting Abstracts, 39, AAS/Division for Planetary Sciences Meeting Abstracts, #22.04

Crepp, J. R., Ge, J., Vanden Heuvel, A. D., Miller, S. P., & Kuchner, M. J. 2006, ApJ, 646, 1252

Crepp, J. R., Vanden Heuvel, A. D., & Ge, J. 2007, ApJ, 661, 1323

Debes, J. H., Ge, J., & Chakraborty, A. 2002, ApJ, 572, L165

Debes, J. H., Ge, J., Kuchner, M. J., & Rogosky, M. 2004, ApJ, 608, 1095

Dekany, R., Bouchez, A., Roberts, J., Troy, M., Kibblewhite, E., Oppenheimer, B., Moore, A., Shelton, C., Smith, R., Trinh, T., & Velur, V. 2007, in Advanced Maui Optical and Space Surveillance Technologies Conference

Des Marais, D. J., Harwit, M. O., Jucks, K. W., Kasting, J. F., Lin, D. N. C., Lunine, J. I., Schneider, J., Seager, S., Traub, W. A., & Woolf, N. J. 2002, Astrobiology, 2, 153

Dohlen, K., Beuzit, J.-L., Feldt, M., Mouillet, D., Puget, P., Antichi, J., Baruffolo, A., Baudoz, P., Berton, A., Boccaletti, A., Carbillet, M., Charton, J., Claudi, R., Downing, M., Fabron, C., Feautrier, P., Fedrigo, E., Fusco, T., Gach, J.-L., Gratton, R., Hubin, N., Kasper, M., Langlois, M., Longmore, A., Moutou, C., Petit, C., Pragt, J., Rabou, P., Rousset, G., Saisse, M., Schmid, H.-M., Stadler, E., Stamm, D., Turatto, M., Waters, R., & Wildi, F. 2006, in Presented at the Society of Photo-Optical Instrumentation Engineers (SPIE) Conference, 6269, Ground-based and Airborne Instrumentation for Astronomy. Edited by McLean, Ian S.; Iye, Masanori. Proceedings of the SPIE, Volume 6269, pp. 62690Q (2006).

Duchêne, G., Delgado-Donate, E., Haisch, K. E., Jr., Loinard, L., & Rodríguez, L. F. 2007, in Protostars and Planets V, ed. B. Reipurth, D. Jewitt, & K. Keil, 379

Duquennoy, A., & Mayor, M. 1991, A&A, 248, 485

Durisen, R. H., Hartquist, T. W., & Pickett, M. K. 2007, ArXiv e-prints, 709

Ellerbroek, B., Britton, M., Dekany, R., Gavel, D., Herriot, G., Macintosh, B., & Stoesz, J. 2005, in Presented at the Society of Photo-Optical Instrumentation Engineers (SPIE) Conference, 5903, Astronomical Adaptive Optics Systems and Applications II. Edited by Tyson, Robert K.; Lloyd-Hart, Michael. Proceedings of the SPIE, Volume 5903, pp. 20-31 (2005)., ed. R. K. Tyson & M. Lloyd-Hart, 20

Fazio, G. G., et al. 2004, ApJS, 154, 10

Fischer, D. A., Butler, R. P., Marcy, G. W., Vogt, S. S., & Henry, G. W. 2003, ApJ, 590, 1081

Ford, V., Levine-West, M., Kissil, A., Kwack, E., Ho, T., Dumont, P., Lisman, D., Feher, P., & Cafferty, T. 2006, in IAU Colloq. 200: Direct Imaging of Exoplanets: Science & Techniques, ed. C. Aime & F. Vakili, 335

Fridlund, C. V. M. 2004, Advances in Space Research, 34, 613

Fruchter, A. S., & Hook, R. N. 2002, PASP, 114, 144

Gabrielse, G., Hanneke, D., Kinoshita, T., Nio, M., & Odom, B. 2006, Physical Review Letters, 97, 030802

Gaidos, E. J., Henry, G. W., & Henry, S. M. 2000, AJ, 120, 1006

Gaudi, B. S., et al. 2008, Science, 319, 927

Ge, J., van Eyken, J., Mahadevan, S., DeWitt, C., Kane, S. R., Cohen, R., Vanden Heuvel, A., Fleming, S. W., Guo, P., Henry, G. W., Schneider, D. P., Ramsey, L. W., Wittenmyer, R. A., Endl, M., Cochran, W. D., Ford, E. B., Martín, E. L., Israelian, G., Valenti, J., & Montes, D. 2006, ApJ, 648, 683

Girardi, L., Bertelli, G., Bressan, A., Chiosi, C., Groenewegen, M. A. T., Marigo, P., Salasnich, B., & Weiss, A. 2002, A&A, 391, 195

Give'On, A., Belikov, R., Shaklan, S., & Kasdin, J. 2007, Optics Express, 15, 12338

Give'on, A., Kern, B., Shaklan, S., Moody, D. C., & Pueyo, L. 2007, in American Astronomical Society Meeting Abstracts, 211, American Astronomical Society Meeting Abstracts, 135.20

Green, J. J., Beichman, C., Basinger, S. A., Horner, S., Meyer, M., Redding, D. C., Rieke, M., & Trauger, J. T. 2005, in Presented at the Society of Photo-Optical Instrumentation Engineers (SPIE) Conference, 5905, Techniques and Instrumentation for Detection of Exoplanets II. Edited by Coulter, Daniel R. Proceedings of the SPIE, Volume 5905, pp. 185-195 (2005)., ed. D. R. Coulter, 185

Green, J. J., & Shaklan, S. B. 2003, in Presented at the Society of Photo-Optical Instrumentation Engineers (SPIE) Conference, 5170, Techniques and Instrumentation for Detection of Exoplanets. Edited by Coulter, Daniel R. Proceedings of the SPIE, Volume 5170, pp. 25-37 (2003)., ed. D. R. Coulter, 25

Guyon, O. 2003, A&A, 404, 379

Guyon, O. 2005, ApJ, 629, 592

Guyon, O., Pluzhnik, E. A., Kuchner, M. J., Collins, B., & Ridgway, S. T. 2006, ApJS, 167, 81

Haghighipour, N., & Raymond, S. N. 2007, ApJ, 666, 436

Hatzes, A. P., Cochran, W. D., Endl, M., Guenther, E. W., Saar, S. H., Walker, G. A. H., Yang, S., Hartmann, M., Esposito, M., Paulson, D. B., & Döllinger, M. P. 2006, A&A, 457, 335

Hayward, T. L., Brandl, B., Pirger, B., Blacken, C., Gull, G. E., Schoenwald, J., & Houck, J. R. 2001, PASP, 113, 105

Hecht, E., & Zajac, A. 1974, Optics (Addison-Wesley Series in Physics, Reading, Mass.: Addison-Wesley, 1974)

Henry, T. J. 2004, in Astronomical Society of the Pacific Conference Series, 318, Spectroscopically and Spatially Resolving the Components of the Close Binary Stars, ed. R. W. Hilditch, H. Hensberge, & K. Pavlovski, 159

Holman, M. J., & Wiegert, P. A. 1999, AJ, 117, 621

Iben, I. J. 1967, ARA&A, 5, 571

Iben, I. J., & Laughlin, G. 1989, ApJ, 341, 312

Ida, S., & Lin, D. N. C. 2004, ApJ, 616, 567

Itoh, Y., Oasa, Y., & Fukagawa, M. 2006, ApJ, 652, 1729

Johnson, J. A. 2007, Ph.D. thesis, University of California, Berkeley

Johnson, J. A., Marcy, G. W., Fischer, D. A., Wright, J. T., Reffert, S., Kregenow, J. M., Williams, P. K. G., & Peek, K. M. G. 2008, ApJ, 675, 784

Kaltenegger, L., Traub, W. A., & Jucks, K. W. 2007, ApJ, 658, 598

Kasdin, N. J., Vanderbei, R. J., Spergel, D. N., & Littman, M. G. 2003, ApJ, 582, 1147

Kasper, M., Apai, D., Janson, M., & Brandner, W. 2007, A&A, 472, 321

Kasting, J. F., Whitmire, D. P., & Reynolds, R. T. 1993, Icarus, 101, 108

Krist, J. 2007, in In the Spirit of Bernard Lyot: The Direct Detection of Planets and Circumstellar Disks in the 21st Century, ed. P. Kalas

Kuchner, M. J., & Spergel, D. N. 2003, ApJ, 594, 617

Kuchner, M. J., & Traub, W. A. 2002, ApJ, 570, 900

Kuchner, Crepp,, & Ge. 2005, ApJ, 628, 466

Labadie, L., Le Coarer, E., Maurand, R., Labeye, P., Kern, P., Arezki, B., & Broquin, J.-E. 2007, A&A, 471, 355

Lafrenière, D., Doyon, R., Marois, C., Nadeau, D., Oppenheimer, B. R., Roche, P. F., Rigaut, F., Graham, J. R., Jayawardhana, R., Johnstone, D., Kalas, P. G., Macintosh, B., & Racine, R. 2007, ApJ, 670, 1367

Lay, O. P., Green, J. J., Hoppe, D. J., & Shaklan, S. B. 2005, in Presented at the Society of Photo-Optical Instrumentation Engineers (SPIE) Conference, 5905, Techniques and Instrumentation for Detection of Exoplanets II. Edited by Coulter, Daniel R. Proceedings of the SPIE, Volume 5905, pp. 148-161 (2005)., ed. D. R. Coulter, 148

Lazcano, A., & Miller, S. 1996, Cell, 85, 793

Lin, D. N. C., Bodenheimer, P., & Richardson, D. C. 1996, Nature, 380, 606

Lissauer, J. J., & Stevenson, D. J. 2007, in Protostars and Planets V, ed. B. Reipurth, D. Jewitt, & K. Keil, 591

Liu, M. C., Fischer, D. A., Graham, J. R., Lloyd, J. P., Marcy, G. W., & Butler, R. P. 2002, ApJ, 571, 519

Lloyd, J. P., Graham, J. R., Kalas, P., Oppenheimer, B. R., Sivaramakrishnan, A., Makidon, R. B., Macintosh, B. A., Max, C. E., Baudoz, P., Kuhn, J. R., & Potter, D. 2001, in Presented at the Society of Photo-Optical Instrumentation Engineers (SPIE) Conference, 4490, Proc. SPIE Vol. 4490, p. 290-297, Multifrequency Electronic/Photonic Devices and Systems for Dual-Use Applications, Andrew R. Pirich; Paul L. Repak; Paul S. Idell; Stanley R. Czyzak; Eds., ed. A. R. Pirich, P. L. Repak, P. S. Idell, & S. R. Czyzak, 290

Lloyd, J. P., & Sivaramakrishnan, A. 2005, ApJ, 621, 1153

Lopez, B., Schneider, J., & Danchi, W. C. 2005, ApJ, 627, 974

López-Santiago, J., Montes, D., Crespo-Chacón, I., & Fernández-Figueroa, M. J. 2006, ApJ, 643, 1160

Luck, R. E., & Heiter, U. 2006, AJ, 131, 3069

Luck, R. E., & Heiter, U. 2007, AJ, 133, 2464

Lyon, R. G., Heap, S., Lo, A., Cash, W., Starkman, G. D., Vanderbei, R. J., Kasdin, N. J., & Copi, C. J. 2007, ArXiv e-prints, 712

Lyot, B. 1939, MNRAS, 99, 538

Macintosh, B., Graham, J., Palmer, D., Doyon, R., Gavel, D., Larkin, J., Oppenheimer, B., Saddlemyer, L., Wallace, J. K., Bauman, B., Evans, J., Erikson, D., Morzinski, K., Phillion, D., Poyneer, L., Sivaramakrishnan, A., Soummer, R., Thibault, S., & Veran, J.-P. 2006a, in Presented at the Society of Photo-Optical Instrumentation Engineers (SPIE) Conference, 6272, Advances in Adaptive Optics II. Edited by Ellerbroek, Brent L.; Bonaccini Calia, Domenico. Proceedings of the SPIE, Volume 6272, pp. 62720L (2006).

Macintosh, B., Troy, M., Doyon, R., Graham, J., Baker, K., Bauman, B., Marois, C., Palmer, D., Phillion, D., Poyneer, L., Crossfield, I., Dumont, P., Levine, B. M., Shao, M., Serabyn, G., Shelton, C., Vasisht, G., Wallace, J. K., Lavigne, J.-F., Valee, P., Rowlands, N., Tam, K., & Hackett, D. 2006b, in Presented at the Society of Photo-Optical Instrumentation Engineers (SPIE) Conference, 6272, Advances in Adaptive Optics II. Edited by Ellerbroek, Brent L.; Bonaccini Calia, Domenico. Proceedings of the SPIE, Volume 6272, pp. 62720N (2006).

Macintosh, B. A., Graham, J., Poyneer, L., Sommargren, G., Wilhelmsen, J., Gavel, D., Jones, S., Kalas, P., Lloyd, J. P., Makidon, R., Olivier, S., Palmer, D., Patience, J., Perrin, M., Severson, S., Sheinis, A., Sivaramakrishnan, A., Troy, M., & Wallace, J. K. 2003, in Presented at the Society of Photo-Optical Instrumentation Engineers (SPIE) Conference, 5170, Techniques and Instrumentation for Detection of Exoplanets. Edited by Coulter, Daniel R. Proceedings of the SPIE, Volume 5170, pp. 272-282 (2003)., ed. D. R. Coulter, 272

Makarov, V. V. 2003, AJ, 126, 1996

Makidon, R. B., Sivaramakrishnan, A., Perrin, M. D., Roberts, L. C., Jr., Oppenheimer, B. R., Soummer, R., & Graham, J. R. 2005, PASP, 117, 831

Marcy, G. W., & Butler, R. P. 2000, PASP, 112, 137

Marley, M. S., Fortney, J. J., Hubickyj, O., Bodenheimer, P., & Lissauer, J. J. 2007, ApJ, 655, 541

Marois, C., Lafrenière, D., Doyon, R., Macintosh, B., & Nadeau, D. 2006, ApJ, 641, 556

Mason, B. D., Hartkopf, W. I., Urban, S. E., Wycoff, G. L., Pascu, D., Hall, D. M., Hennessy, G. S., Platais, I., Rafferty, T. J., & Holdenried, E. R. 2002, AJ, 124, 2254

Mawet, D., Riaud, P., Absil, O., & Surdej, J. 2005, ApJ, 633, 1191

Mawet, D., Riaud, P., Hanot, C., Vandormael, D., Loicq, J., Baudrand, J., Surdej, J., & Habraken, S. 2007, in Presented at the Society of Photo-Optical Instrumentation Engineers (SPIE) Conference, 6693, SPIE , Proc. SPIE 6693, id. #66931M (2007), 52

Mayama, S., Tamura, M., Hayashi, M., Itoh, Y., Fukagawa, M., Suto, H., Ishii, M., Murakawa, K., Oasa, Y., Hayashi, S. S., Yamashita, T., Morino, J., Oya, S., Naoi, T., Pyo, T.-S., Nishikawa, T., Kudo, T., Usuda, T., Ando, H., Miyama, S. M., & Kaifu, N. 2006, PASJ, 58, 375

Mayer, K. A., & Stevenson, D. J. 1988, Nature, 331, 612

McCarthy, C., & Zuckerman, B. 2004, AJ, 127, 2871

McElwain, M. W., Metchev, S. A., Larkin, J. E., Barczys, M., Iserlohe, C., Krabbe, A., Quirrenbach, A., Weiss, J., & Wright, S. A. 2007, ApJ, 656, 505

Metchev, S. A., & Hillenbrand, L. A. 2004, ApJ, 617, 1330

Mugrauer, M., Seifahrt, A., & Neuhäuser, R. 2007, MNRAS, 378, 1328

Mullally, F., Winget, D. E., Degennaro, S., Jeffery, E., Thompson, S. E., Chandler, D., & Kepler, S. O. 2008, ApJ, 676, 573

Murakami, N., & Baba, N. 2005, PASP, 117, 295

Nakajima, T. 2006, ApJ, 652, 1782

Neuhäuser, R., Guenther, E. W., Wuchterl, G., Mugrauer, M., Bedalov, A., & Hauschildt, P. H. 2005, A&A, 435, L13

Nielsen, E. L., Close, L. M., Biller, B. A., Masciadri, E., & Lenzen, R. 2008, ApJ, 674, 466

Nordgren, T. E., Sudol, J. J., & Mozurkewich, D. 2001, AJ, 122, 2707

Ochsenbein, F., & Halbwachs, J. L. 1982, A&AS, 47, 523

Oppenheimer, B. R., Digby, A. P., Newburgh, L., Brenner, D., Shara, M., Mey, J., Mandeville, C., Makidon, R. B., Sivaramakrishnan, A., Soummer, R., Graham, J. R., Kalas, P., Perrin, M. D., Roberts, L. C., Jr., Kuhn, J. R., Whitman, K., & Lloyd, J. P. 2004, in Presented at the Society of Photo-Optical Instrumentation Engineers (SPIE) Conference, 5490, Advancements in Adaptive Optics. Edited by Domenico B. Calia, Brent L. Ellerbroek, and Roberto Ragazzoni. Proceedings of the SPIE, Volume 5490, pp. 433-442 (2004)., ed. D. Bonaccini Calia, B. L. Ellerbroek, & R. Ragazzoni, 433

Perrin, M. D., Graham, J. R., & Lloyd, J. P. 2008, PASP, 120, 555

Phillips, A., Burton, M. G., Ashley, M. C. B., Storey, J. W. V., Lloyd, J. P., Harper, D. A., & Bally, J. 1999, ApJ, 527, 1009

Pollack, J. B., Hubickyj, O., Bodenheimer, P., Lissauer, J. J., Podolak, M., & Greenzweig, Y. 1996, Icarus, 124, 62

Potter, D., Martín, E. L., Cushing, M. C., Baudoz, P., Brandner, W., Guyon, O., & Neuhäuser, R. 2002, ApJ, 567, L133

Quintana, E. V., Adams, F. C., Lissauer, J. J., & Chambers, J. E. 2007, ApJ, 660, 807

Roberts, L. C., Jr., Perrin, M. D., Marchis, F., Sivaramakrishnan, A., Makidon, R. B., Christou, J. C., Macintosh, B. A., Poyneer, L. A., van Dam, M. A., & Troy, M. 2004, in Presented at the Society of Photo-Optical Instrumentation Engineers (SPIE) Conference, 5490, Advancements in Adaptive Optics. Edited by Domenico B. Calia, Brent L. Ellerbroek, and Roberto Ragazzoni. Proceedings of the SPIE, Volume 5490, pp. 504-515 (2004)., ed. D. Bonaccini Calia, B. L. Ellerbroek, & R. Ragazzoni, 504

Roddier, F., & Roddier, C. 1997, PASP, 109, 815

Rouan, D., Riaud, P., Boccaletti, A., Clénet, Y., & Labeyrie, A. 2000, PASP, 112, 1479

Sandler, D. G., Stahl, S., Angel, J. R. P., Lloyd-Hart, M., & McCarthy, D. 1994, Journal of the Optical Society of America A, 11, 925

Scardia, M., Prieur, J.-L., Pansecchi, L., Argyle, R. W., Sala, M., Basso, S., Ghigo, M., Koechlin, L., & Aristidi, E. 2008, Astronomische Nachrichten, 329, 54

Seager, S., Kuchner, M., Hier-Majumder, C. A., & Militzer, B. 2007, ApJ, 669, 1279

Semaltianos, N. 2001, Applied Surface Science, 183, 223

Serabyn, E., Appleby, E., Bell, J., Booth, A., Chin, J., Colavita, M. M., Crawford, S., Creech-Eakman, M., Dahl, W., Fanson, J., Garcia, J., Gathright, J., Hovland, E., Hrynevych, M., Koresko, C., Ligon, R., Mennesson, B., Moore, J., Palmer, D., Panteleeva, T., Paine, C., Ragland, S., Reder, L., Saloga, T., Smythe, R., Tyau, C., Tsubota, K., Vasisht, G., Wetherell, E., Wizinowich, P., & Woillez, J. 2005, in Presented at the Society of Photo-Optical Instrumentation Engineers (SPIE) Conference, 5905, Techniques and Instrumentation for Detection of Exoplanets II. Edited by Coulter, Daniel R. Proceedings of the SPIE, Volume 5905, pp. 272-283 (2005)., ed. D. R. Coulter, 272

Serabyn, E., Wallace, K., Troy, M., Mennesson, B., Haguenauer, P., Gappinger, R., & Burruss, R. 2007, ApJ, 658, 1386

Shaklan, S., & Levine, M. 2007, in In the Spirit of Bernard Lyot: The Direct Detection of Planets and Circumstellar Disks in the 21st Century, ed. P. Kalas

Shaklan, S. B., & Green, J. J. 2005, ApJ, 628, 474

Shaklan, S. B., & Green, J. J. 2006, Appl. Opt., 45, 5143

Sivaramakrishnan, A., Koresko, C. D., Makidon, R. B., Berkefeld, T., & Kuchner, M. J. 2001, ApJ, 552, 397

Sivaramakrishnan, A., & Lloyd, J. P. 2005, ApJ, 633, 528

Sivaramakrishnan, A., Soummer, R., Sivaramakrishnan, A. V., Lloyd, J. P., Oppenheimer, B. R., & Makidon, R. B. 2005, ApJ, 634, 1416

Sivaramakrishnan, A., & Yaitskova, N. 2005, ApJ, 626, L65

Skrutskie, M. F., Cutri, R. M., Stiening, R., Weinberg, M. D., Schneider, S., Carpenter, J. M., Beichman, C., Capps, R., Chester, T., Elias, J., Huchra, J., Liebert, J., Lonsdale, C., Monet, D. G., Price, S., Seitzer, P., Jarrett, T., Kirkpatrick, J. D., Gizis, J. E., Howard, E., Evans, T., Fowler, J., Fullmer, L., Hurt, R., Light, R., Kopan, E. L., Marsh, K. A., McCallon, H. L., Tam, R., Van Dyk, S., & Wheelock, S. 2006, AJ, 131, 1163

Soummer, R. 2005, ApJ, 618, L161

Tarter, J. C., Backus, P. R., Mancinelli, R. L., Aurnou, J. M., Backman, D. E., Basri, G. S., Boss, A. P., Clarke, A., Deming, D., Doyle, L. R., Feigelson, E. D., Freund, F., Grinspoon, D. H., Haberle, R. M., Hauck, S. A., II, Heath, M. J., Henry, T. J., Hollingsworth, J. L., Joshi, M. M., Kilston, S., Liu, M. C., Meikle, E., Reid, I. N., Rothschild, L. J., Scalo, J., Segura, A., Tang, C. M., Tiedje, J. M., Turnbull, M. C., Walkowicz, L. M., Weber, A. L., & Young, R. E. 2007, Astrobiology, 7, 30

Telesco, C. M. 2007, in Revista Mexicana de Astronomia y Astrofisica Conference Series, 29, Revista Mexicana de Astronomia y Astrofisica Conference Series, 1

Telesco, C. M., Pina, R. K., Hanna, K. T., Julian, J. A., Hon, D. B., & Kisko, T. M. 1998, in Presented at the Society of Photo-Optical Instrumentation Engineers (SPIE) Conference, 3354, Proc. SPIE Vol. 3354, p. 534-544, Infrared Astronomical Instrumentation, Albert M. Fowler; Ed., ed. A. M. Fowler, 534

Thomsen, M., Britton, M., & Pickles, A. 2007, in American Astronomical Society Meeting Abstracts, 210, American Astronomical Society Meeting Abstracts, 117.01

Tokovinin, A. 2004, in Revista Mexicana de Astronomia y Astrofisica Conference Series, 21, Revista Mexicana de Astronomia y Astrofisica Conference Series, ed. C. Allen & C. Scarfe, 7

Traub, W. A., Levine, M., Shaklan, S., Kasting, J., Angel, J. R., Brown, M. E., Brown, R. A., Burrows, C., Clampin, M., Dressler, A., Ferguson, H. C., Hammel, H. B., Heap, S. R., Horner, S. D., Illingworth, G. D., Kasdin, N. J., Kuchner, M. J., Lin, D., Marley, M. S., Meadows, V., Noecker, C., Oppenheimer, B. R., Seager, S., Shao, M., Stapelfeldt, K. R., & Trauger, J. T. 2006, in Presented at the Society of Photo-Optical Instrumentation Engineers (SPIE) Conference, 6268, Advances in Stellar Interferometry. Edited by Monnier, John D.; Schöller, Markus; Danchi, William C.. Proceedings of the SPIE, Volume 6268, pp. 62680T (2006).

Trauger, J. T., Burrows, C., Gordon, B., Green, J. J., Lowman, A. E., Moody, D., Niessner, A. F., Shi, F., & Wilson, D. 2004, in Presented at the Society of Photo-Optical Instrumentation Engineers (SPIE) Conference, 5487, Optical, Infrared, and Millimeter Space Telescopes. Edited by Mather, John C. Proceedings of the SPIE, Volume 5487, pp. 1330-1336 (2004)., ed. J. C. Mather, 1330

Trauger, J. T., & Traub, W. A. 2007, Nature, 446, 771

Trilling, D. E., Stansberry, J. A., Stapelfeldt, K. R., Rieke, G. H., Su, K. Y. L., Gray, R. O., Corbally, C. J., Bryden, G., Chen, C. H., Boden, A., & Beichman, C. A. 2007, ApJ, 658, 1289

Troy, M., Crossfield, I., Chanan, G., Dumont, P., Green, J. J., & Macintosh, B. 2006, in Presented at the Society of Photo-Optical Instrumentation Engineers (SPIE) Conference, 6272, Advances in Adaptive Optics II. Edited by Ellerbroek, Brent L.; Bonaccini Calia, Domenico. Proceedings of the SPIE, Volume 6272, pp. 62722C (2006).

Troy, M., Dekany, R. G., Brack, G., Oppenheimer, B. R., Bloemhof, E. E., Trinh, T., Dekens, F. G., Shi, F., Hayward, T. L., & Brandl, B. 2000, in Presented at the Society of Photo-Optical Instrumentation Engineers (SPIE) Conference, 4007, Proc. SPIE Vol. 4007, p. 31-40, Adaptive Optical Systems Technology, Peter L. Wizinowich; Ed., ed. P. L. Wizinowich, 31

Turnbull, M. C. 2008, Space Science Reviews, 63

Veras, Crepp, & Ford. 2008, ApJ, in prep.

Wallace, K., Hardy, G., & Serabyn, E. 2000, Nature, 406, 700

Wolszczan, A., & Frail, D. A. 1992, Nature, 355, 145

Wright, B., Marcy, & Vogt. 2008, ApJ, in prep.

Zuckerman, B., & Song, I. 2004, ARA&A, 42, 685

## BIOGRAPHICAL SKETCH

Justin Robert Crepp was born in Ellwood City, Pennsylvania, USA in 1979 to parents Robert and Jennie Crepp. He has a younger brother, Adam, and a large family with many aunts, uncles, and cousins. Justin graduated from Penn State Erie - The Behrend College, with a bachelors degree in physics and minor in mathematics in December 2002. On October 16th, 2006, he married Amy Lynn Slozat on Holmes Beach near the Tampa Bay. Their first child, Aaron Justin, was born just days before the final version of this work was submitted to the University of Florida Department of Astronomy.